NAVAL POSTGRADUATE SCHOOL

MONTEREY, CALIFORNIA

THESIS

DESIGN AND IMPLEMENTATION OF A HIGH-FLUX PHOTONEUTRON CONVERTER FOR ANALYSIS OF FAST NEUTRON RADIATION DAMAGE ON GALLIUM NITRIDE TRANSISTORS

by

Connor Westrick

June 2017

Thesis Co-Advisors:	Todd Weatherford
	Frank Harmon
Second Reader:	Matthew Porter

Approved for public release. Distribution is unlimited.

THIS PAGE INTENTIONALLY LEFT BLANK

REPORT DOCUMENTATION PAGE

Form Approved OMB No. 0704–0188

1. AGENCY USE ONLY *(Leave Blank)*	2. REPORT DATE June 2017	3. REPORT TYPE AND DATES COVERED Master's Thesis 06-27-2016 to 06-01-2017

4. TITLE AND SUBTITLE

DESIGN AND IMPLEMENTATION OF A HIGH-FLUX PHOTONEUTRON CONVERTER FOR ANALYSIS OF FAST NEUTRON RADIATION DAMAGE ON GALLIUM NITRIDE TRANSISTORS

5. FUNDING NUMBERS

6. AUTHOR(S)

Connor Westrick

7. PERFORMING ORGANIZATION NAME(S) AND ADDRESS(ES)

Naval Postgraduate School
Monterey, CA 93943

8. PERFORMING ORGANIZATION REPORT NUMBER

9. SPONSORING / MONITORING AGENCY NAME(S) AND ADDRESS(ES)

Defense Threat Reduction Agency, Ft. Belvoir, VA 22060

10. SPONSORING / MONITORING AGENCY REPORT NUMBER

11. SUPPLEMENTARY NOTES

The views expressed in this document are those of the author and do not reflect the official policy or position of the Department of Defense or the U.S. Government. IRB Protocol Number: N/A.

12a. DISTRIBUTION / AVAILABILITY STATEMENT

Approved for public release. Distribution is unlimited.

12b. DISTRIBUTION CODE

13. ABSTRACT *(maximum 200 words)*

Gallium Nitride(GaN) is known for its wide-energy bandgap of 3.4 eV and its high-efficiency as a semiconductor, which makes it a prime material for high-power, high-frequency, and low-noise systems. Specifically, GaN high electron-mobility transistors (HEMTs) have seen an increase in popularity due to its two-dimensional electron gas (2DEG) that allows for increased mobility of un-doped GaN. In this work, GaN HEMTs were irradiated with a fluence of $2x10^{16}\text{n/cm}^2$ while maintaining a 99 percent fast-to-thermal neutron ratio. There were three phases to this work, the first was the design and fabrication of a photoneutron converter. The second was the design and implementation of a device testing suite in order to characterize the GaN HEMTs before, during, and after the experiment. The last was the analysis of the data showing the relationship of the electrical and physical characteristics of the devices with respect to the fast neutron fluence. The damage was also analyzed using a total displacement calculation for each layer of the device. The GaN HEMTs linearly degraded due to the high energy neutron displacements within the heterojunction layers.

14. SUBJECT TERMS

Fast neutrons, non-ionizing radiation, gallium nitride, high electron mobility transistors, flux, fluence, radiation, linear accelerator

15. NUMBER OF PAGES   171

16. PRICE CODE

17. SECURITY CLASSIFICATION OF REPORT	18. SECURITY CLASSIFICATION OF THIS PAGE	19. SECURITY CLASSIFICATION OF ABSTRACT	20. LIMITATION OF ABSTRACT
Unclassified	Unclassified	Unclassified	UU

Standard Form 298 (Rev. 2–89)
Prescribed by ANSI Std. 239–18

i

THIS PAGE INTENTIONALLY LEFT BLANK

DESIGN AND IMPLEMENTATION OF A HIGH-FLUX PHOTONEUTRON CONVERTER FOR ANALYSIS OF FAST NEUTRON RADIATION DAMAGE ON GALLIUM NITRIDE TRANSISTORS

Connor Westrick
Ensign, United States Navy
B.S., United States Naval Academy, 2016

Submitted in partial fulfillment of the
requirements for the degree of

MASTER OF SCIENCE IN ELECTRICAL ENGINEERING

from the

**NAVAL POSTGRADUATE SCHOOL
June 2017**

Approved by: Todd Weatherford
                    Thesis Co-Advisor

                    Frank Harmon, Idaho State University
                    Thesis Co-Advisor

                    Matthew Porter
                    Second Reader

                    R. Clark Robertson
                    Chair, Department of Electrical and Computer Engineering

iii

THIS PAGE INTENTIONALLY LEFT BLANK

ABSTRACT

Gallium Nitride(GaN) is known for its wide-energy bandgap of 3.4 eV and its high-efficiency as a semiconductor, which makes it a prime material for high-power, high-frequency, and low-noise systems. Specifically, GaN high electron-mobility transistors (HEMTs) have seen an increase in popularity due to its two-dimensional electron gas (2DEG) that allows for increased mobility of un-doped GaN. In this work, GaN HEMTs were irradiated with a fluence of $2x10^{16}\text{n/cm}^2$ while maintaining a 99 percent fast-to-thermal neutron ratio. There were three phases to this work, the first was the design and fabrication of a photoneutron converter. The second was the design and implementation of a device testing suite in order to characterize the GaN HEMTs before, during, and after the experiment. The last was the analysis of the data showing the relationship of the electrical and physical characteristics of the devices with respect to the fast neutron fluence. The damage was also analyzed using a total displacement calculation for each layer of the device. The GaN HEMTs linearly degraded due to the high energy neutron displacements within the heterojunction layers.

THIS PAGE INTENTIONALLY LEFT BLANK

Table of Contents

List of Figures

List of Tables

THIS PAGE INTENTIONALLY LEFT BLANK

List of Acronyms and Abbreviations

2DEG two-dimensional electron gas

Al aluminum

AlGaN aluminum gallium nitride

AlN aluminum nitride

Au gold

DLTS deep-level transient spectroscopy

DLOS deep-level optical spectroscopy

DMEA Defense Microelectronics Activity

DoD Department of Defense

DUT device-under-test

EAGLE Easily Applicable Graphical Layout Editor

ENDF Evaluated Nuclear Data File

Ga gallium

GaN gallium nitride

GDR giant dipole resonance

HEMT high electron-mobility transistor

IAC Idaho Accelerator Center

InN Indium Nitride

ITER International Thermonuclear Experimental Reactor

LINAC linear accelerator

MBE molecular beam epitaxy

MCNP Monte Carlo N-Particle program

MOCVD metal organic channel vapor deposition

Ni nickel

NRL Naval Research Laboratory

NPS Naval Postgraduate School

PKA primary knock-on atom

Si silicon

SiC silicon carbide

SMU source measurement unit

TRIGA Training, Research, Isotopes, General Atomics

Acknowledgments

I would like to thank Professor Weatherford for accepting me onto his thesis team and for providing his support and knowledge toward my thesis as my advisor. The radiation and reliability course you offer was crucial to helping me understand the radiation effects and reliability issues in semiconductor devices.

I would also like to thank Matthew Porter for providing the essential semiconductor physics knowledge and the technical expertise required for designing and implementing a radiation experiment on electrical devices. The long hours and patience you provided me was invaluable toward the completion of this experiment. I would not have been able to complete this experiment without your aid.

I would also like to extend my thanks to Professor Harmon, Jon Stoner, Kevin, Brian, Chad, and the rest of the group at the Idaho Accelerator Center in Pocatello, Idaho. Their knowledge of linear accelerator operation, radiation physics, and dosimetry was critical in the design and fabrication of the photoneutron converter and the successful completion of the radiation portion of this experiment.

THIS PAGE INTENTIONALLY LEFT BLANK

CHAPTER 1:
Introduction

Whether using satellites in space, weapons at high altitudes, or control systems within nuclear-power plants, radiation-resistant electronics must be used to ensure reliable system operation. Radiation of concern to electronics operation can come from cosmic rays, medical instruments, fission events, and fusion events, but in all cases, high-energy particles or electromagnetic waves cause damage in the atomic structures. Electronics are sensitive to the effects of radiation because any alteration in the material's atomic structure can cause large changes in electrical device characteristics [1]. If the radiation dose is large enough, electronic devices may fail. While there are ways such as shielding that can protect electronics, such techniques add costly weight and volume to systems that require high reliability. Finding materials that are more radiation resistant than the materials used commonly today in electronic devices is imperative. One of these materials that is being studied is gallium nitride (GaN), which has shown promising results toward radiation hardness and use in high-power applications due to its high direct-band gap [2].

1.1 Motivation

High-power, high-frequency, and high-reliability electronics are an integral part of the energy infrastructure in today's society. Due to the projected depletion of fossil fuel sources in the 21$^{\text{st}}$ century, nuclear power is a potential source of energy that could help solve this crisis. Next-generation nuclear power will demand greater control and monitoring of radiation which will require electronics to be radiation hard in high-radiation environments. Fusion reactors take a plasma of deuterium and tritium molecules that is magnetically confined and fuses them by injecting large amounts of energy into the plasma containment chamber [3]. Fusion reactors do not thermalize their neutrons because they do not rely on neutrons to fuel the fusion reaction. The non-reliance upon thermal neutrons causes a large field of fast neutrons that have small cross-sections of interaction [4]. The core of fusion reactors transfers roughly 80 percent of its energy into 14-MeV neutrons, while the rest of the energy goes into alpha particles [5]. An image of the core of the International Thermonuclear Experimental Reactor (ITER) Tokamak, which is isolated through magnetic confinement

using large coils of electromagnets, is shown in Figure 1.1. The ITER Tokamak was built as an experimental fusion reactor that hopes to be the breakthrough in fusion energy. Due to the high-energy spectrum of neutrons, understanding the damage effects of fast neutrons upon the electronics involved in the system is crucial [3].
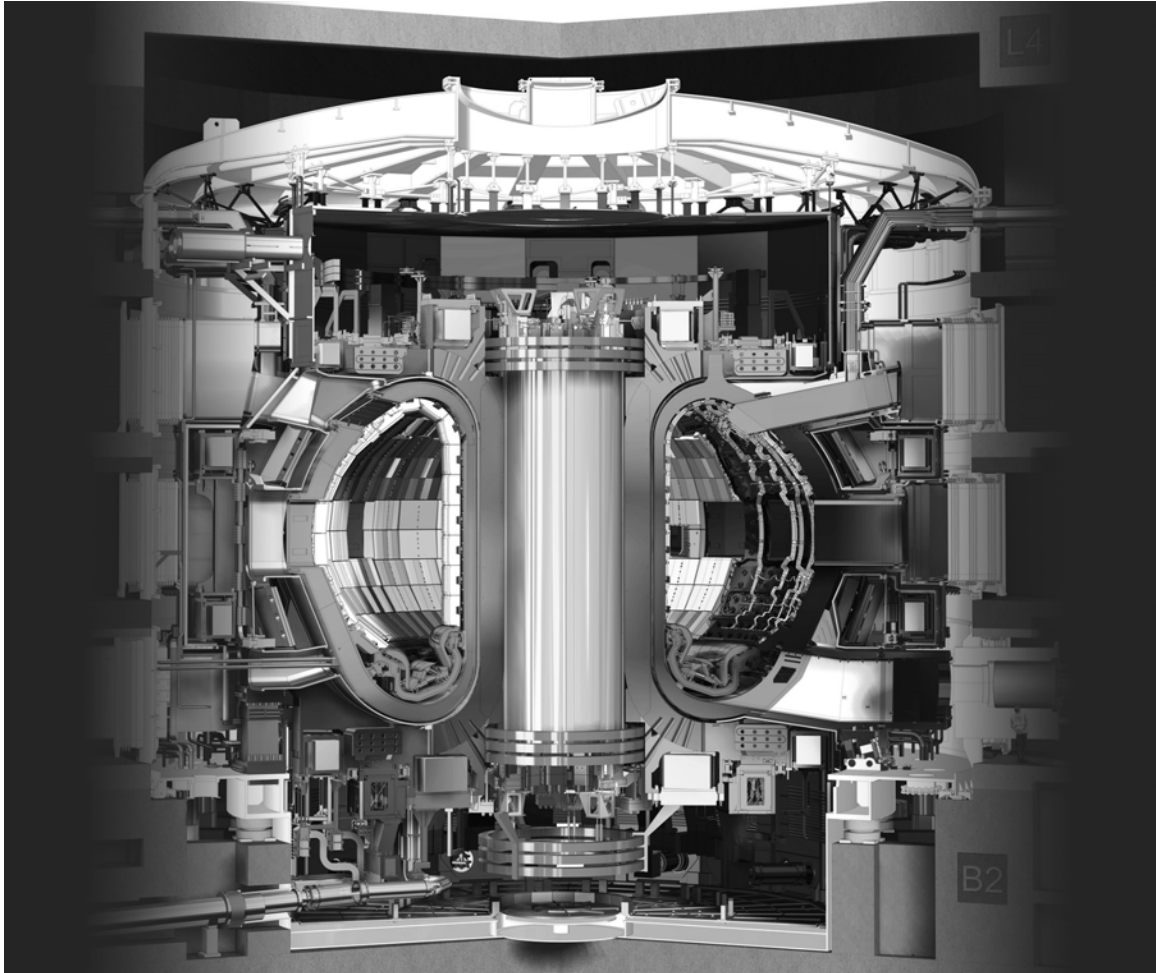
Figure 1.1. The Core of the ITER Tokamak Reactor Located in Saint-Paul-lès-Durance, France. Source: [3].

The research provided in this work strives to study the effects of fast-neutron damage and a possible radiation-hard semiconductor, GaN, for use in high radiation-field environments. While hoping to provide electronics capable of reliable use in nuclear power, there are also other applications that would benefit from a semiconductor capable of such radiation doses. With transistors becoming smaller and cheaper as technology improves, the reliability of such transistors decreases [1]. Providing a semiconductor with the reliability discussed

would prove useful for space and military applications. All space and military electronics need to have longer life times and higher hardness towards radiation than that required for consumer electronics. In this research, we hope to get one step closer to finding an electronic device resistant to high-penetration radiation.

1.2 Research Objective

The goal for this research was to irradiate GaN-on-silicon (Si) high electron-mobility transistors (HEMTs) with a high fluence of fast neutrons and to determine the physical damage, electrical alterations within the devices, and ultimately the radiation hardness of the devices toward fast neutrons. GaN is being studied because its wide-band gap characteristic is well suited for use in high-power applications and its insensitivity to ionizing radiation. Specifically, GaN-on-Si technology is being explored because it is the most economical way to grow GaN with low crystal structure deformities. Since HEMTs are designed to utilize the spontaneous and piezoelectric polarization inherent in the III-Nitride semiconductor group to create a two-dimensional electron gas (2DEG) within the transistor [6], it was imperative to understand the effect of the radiation damage in the crystalline structure. GaN-on-Si HEMTs have been shown by Wade and Iobst to be radiation hard toward 2 MeV protons and gamma irradiation, but the effects of non-ionizing radiation still need to be further investigated [7] [2].

The goal for this research was to employ a linear accelerator (LINAC) to generate fast neutrons to a flux greater than $6 \cdot 10^{10}$ n/cm^{2}s over a period of 50 hours in order to provide the non-ionizing damage required to test the radiation hardness of GaN. An efficient photoneutron converter needed to be designed in order to achieve a high flux of fast neutrons. Using a LINAC allowed us to optimize the neutron flux for irradiating the GaN-on-Si HEMTs. While maximizing fast-neutron flux was essential for analyzing displacement damage within the devices, other requirements were also present. One requirement was to minimize the activation of the devices under test. A second requirement was to be able to take the irradiated parts back to the Naval Postgraduate School (NPS) to run post-experiment tests and compare with the pre-experiment test results. To minimize activation, the energy range of the neutron spectrum produced by the photoneutron converter needed to have at least 99-percent fast neutrons with only one-percent thermal neutrons. While minimizing thermal neutrons, the experiment also needed to minimize the dose received

by gamma irradiation. Gamma irradiation was naturally a factor that needed to be taken into account since the experiment utilized the photonuclear effect via gamma rays, known as bremsstrahlung, in order to create secondary neutrons at a high flux. Minimizing the gamma radiation that escapes the converter ensures accurate results and analysis of the permanent damage within the devices because this experiment was focused around non-ionizing damage within the devices. To develop a fast-neutron source that supports device testing, heating of the photoneutron converter needed to be taken into account in order to minimize the annealing and possible damage of the tested devices due to overheating; therefore, an active convection-cooling system needed to be designed around the photoneutron converter to minimize heating.

Another objective of the experiment was to provide accurate measurements at a far distance from the GaN devices at constant intervals during the experiment to obtain various electrical characteristics of the devices with respect to neutron fluence by measuring the current-voltage relationships across the device. A few examples of such characteristics include voltage threshold, gate leakage, access resistance, and dynamic on-state resistance. These parameters are derived from the I-V characteristics of the device which are measured using static-DC and pulsed-DC tests. Investigating the device property changes due to fast-neutron radiation provides further knowledge about the radiation hardness of GaN and specifically GaN-on-Si HEMTs toward neutron-displacement damage.

1.3 Prior Work

In a previous thesis done at the NPS in 2015 by Iobst, GaN-on-Si HEMTs were irradiated by gamma radiation and neutron radiation. The neutron radiation was generated from a Training, Research, Isotopes, General Atomics (TRIGA) reactor at UC Davis, California and achieved a fast-neutron flux of $5 \cdot 10^9 \pm 2.5 \cdot 10^9$ n/(cm^2 · s) and a total fluence of $1.2 \cdot 10^{15} \pm 5 \cdot 10^{14}$ n/cm^2 [2]. The gamma-radiation experiment took place at the Defense Microelectronics Activity (DMEA) up to a total dose of 2 Mrads(SiO_2). In relation to the neutron experiment, nuclear reactors are designed around producing as many thermal neutrons as possible in order to promote energy production within the core, but this in turn caused the devices to be activated. Iobst measured the electrical characteristics of the GaN devices before and during the experiment at varying radiation levels. The results demonstrated that the GaN HEMTs are resistant to both gamma radiation and low levels

of neutron radiation. The only characteristics that had a significant change during the experiments were the gate leakage and the conductance of the devices [2].

Also in 2015, another thesis was completed at NPS by Wade. Wade conducted an experiment where he examined irradiation of the GaN HEMTs with 2.0 MeV protons up to a fluence of $6 \cdot 10^{14}$ H/cm^2. The results showed that the proton irradiation produced voiding within the nickel (Ni)-gate layer of the HEMT which resulted in a decrease in the effective-gate area [7]. This decrease in effective-gate area decreased the capacitance of the devices after irradiation. Since protons have a higher probability of interaction at an atomic level than neutrons do due to their charge, the damage from the protons was far more significant than the damage from the neutrons as found by Iobst [7]; thus, a higher fluence of fast-neutron irradiation needed to be achieved in order to attempt to see similar amount of damage within the GaN HEMTs due to neutrons as was found by protons.

1.4 Thesis Outline

The current thesis is organized as follows. The semiconductor background behind this thesis study including the physics of GaN HEMTs, the effect of stress and polarization within these devices, and the influences of non-ionizing radiation in GaN is presented in Chapter 2. The simulation, design, and testing of a high-flux photoneutron converter are discussed in Chapter 3 along with the physics behind the photoneutron converter. The design of the in-situ testing of the GaN-on-Si HEMTs are discussed in Chapter 4. Results and analysis of the in-situ testing and the pre-irradiation and post-irradiation electrical-parameter comparisons of the GaN HEMTs are presented in Chapter 5. In this chapter, we also include the calculations for total displacement within each layer of the device due to the neutron radiation. Finally, conclusions and recommendations for future work are presented in Chapter 6.

THIS PAGE INTENTIONALLY LEFT BLANK

CHAPTER 2:
Radiation Effects on Gallium Nitride Transistors

Introduction into the type of semiconductor devices irradiated in the experiment is provided in this chapter. First, GaN, selected as the primary semiconductor material investigated in this research, is discussed. Second, we present an introduction into the physics of heterojunction growth, as well as the polarization and 2DEG control between aluminum gallium nitride (AlGaN) and GaN layers. Third, the physical and electrical properties of GaN HEMTs are discussed. Lastly, the effects of radiation within GaN devices are described followed by a timeline of the previous work done with neutron irradiation on GaN devices.

2.1 Gallium Nitride

Gallium Nitride (GaN) is a group (III-N) compound semiconductor with a Wurtzite crystal structure. With a direct band-energy gap of 3.4 eV, GaN falls in the wide band gap category of semiconductor materials while semiconductors like Si and Indium Nitride (InN) fall within the lower-energy band gap spectrum [8]. GaN is the focus of this investigation due to its many operational advantages, including its high electron mobility and high-breakdown field. Since GaN is a member of the III-V semiconductor group the material has inherent polarization within its crystal structure due to the asymmetric bonding between the Ga and nitrogen [9]. Due to this polarization, heterojunctions can be grown epitaxially in the direction of polarization to form a high-density 2DEG with high mobility. HEMTs use this 2DEG as their charge-carrier channel and can be used in high-power and high-frequency applications due to the high-breakdown voltage of GaN and high mobilities within the 2DEG [10]. GaN also has a high atomic-displacement threshold due to its wide band gap which makes it an attractive semiconductor for applications requiring radiation hardness.

2.2 GaN/AlGaN Heterojunctions

Heterojunctions are the composite of different epitaxially grown semiconductors which are overlaid in order to produce the desired device characteristics or material quality. The properties of heterojunctions can be engineered by choosing the appropriate materials,

especially through the use of alloys. Group (III-N) heterojunctions provide the ability to form a 2DEG through the use of polarization between two layers [10].

2.2.1   Heterojunction Growth

Epitaxial semiconductor layers of a III-N heterojunction can be grown by either molecular beam epitaxy (MBE) or by metal organic channel vapor deposition (MOCVD), and utilize various buffer layers to filter out strain within the device [10]. This strain comes from the mismatch in the lattice constants between different semiconductor materials [11]. Growing GaN is exceptionally difficult because a high density of defects will be present in the grown material if it is done without using a native GaN substrate. A way that manufacturers grow GaN is by epitaxially growing the GaN on top of a substrate that acts as a suitable template for growth. A lattice-constant difference between the two materials occurs when two different materials are grown on top of each other. This difference induces tensile strain on one material while the other undergoes compression strain. As an example, the stress between semiconductors can be explained by looking at the lattice constants of GaN and Si in which [12]

$$S_{xx} = S_{yy} = \frac{a_{Si} - a_{GaN}}{a_{GaN}}, \tag{2.1}$$

where S_{xx} and S_{yy} represent the biaxial strain in the plane perpendicular to the growth direction. In the above equation, a_{Si} is the lattice constant for Si which is 5.431 Å, and a_{GaN} is the lattice constant for GaN which is 3.187 Å [13]. For this example, the biaxial strain is found to be 0.704. In the case of GaN grown on Si, the GaN layer would undergo tensile strain over the Si layer which would be in a compression state. When the magnitude of the strain in the layer becomes too large, the epitaxial material relaxes through the formation of defects, such as dislocations and grain boundaries [14]. The method used by semiconductor manufacturers to be able to grow GaN-on-Si without a large number of crystalline defects from crystal strain is to grow epitaxial buffer layers between the GaN and Si layers. Using buffer layers allows the strain to be relieved before the electrically useful GaN is grown. The buffer layers serve as a lattice transition from a larger lattice constant to a smaller lattice constant that matches GaN better. The buffer layers act as a filter for dislocations, fractures, and other defects in the crystalline structure that occur due

to the lattice mismatch [9]. A TEM cross-sectional image showing the dislocations of the epitaxial growth of GaN-on-Sapphire is shown in Figure 2.1.
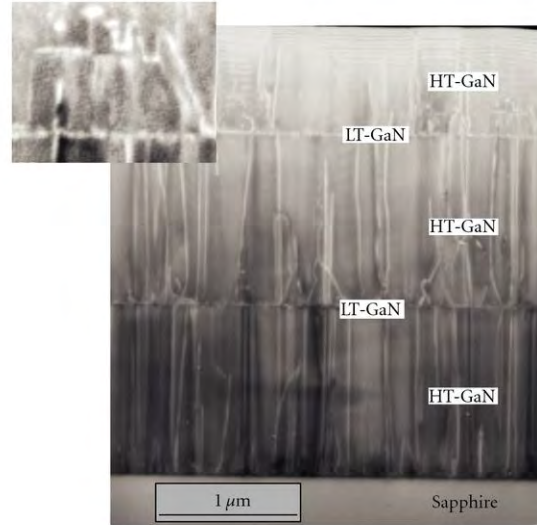
Figure 2.1. TEM Cross-Section Image of GaN-on-Sapphire Device. Source: [15].

The dislocations within the layers of the device show the effects of lattice mismatch and the issues with growing GaN on a mismatched substrate such as sapphire. It is important to minimize these defects within the GaN crystal structure in order to minimize the scattering of the charge carriers and maximize the charge density and mobility within the device [16]. When growing III-N heterojunctions, it is essential to use multiple buffer layers to filter out the majority of the defects caused by epitaxial growth [11]. Once a base of buffer layers with few defects and a similar lattice constant to GaN is achieved, high-quality GaN can be grown suitable for device use.

2.2.2   Polarization in GaN

Heterostructures fabricated from III-N semiconductors are unique because there exists an inherent polarization within these materials. Polarization within a semiconductor crystalline structure is induced by charge imbalance within the unit cell due to the lack of symmetry in the Wurtzite crystal structure [9]. In III-N heterojunctions, there are two types of polarization that play a key role in spontaneous and piezoelectric polarization [17]. Spontaneous polarization is the inherent polarization within group III-Ns that is caused by the lack of

9

crystalline symmetry of the crystal structure [10]. Piezoelectric polarization is caused by mechanical strain, typically induced by epitaxial growth of layers of different lattice constants [10]. The piezoelectric polarization is developed in a GaN/AlGaN heterojunction, for example, by growing a thin layer of $Al_xGa_{1-x}N$ on top of a much thicker GaN layer. The x refers to the molar concentration of aluminum nitride within the AlGaN compound, and the $1 - x$ is the GaN concentration within the compound. If the GaN layer is much larger than the thickness of the $Al_xGa_{1-x}N$ layer, it can be assumed that all of the strain will be placed on the thinner $Al_xGa_{1-x}N$ layer [14]. The GaN layer is therefore only influenced by the spontaneous polarization since all the strain is being placed in the thin $Al_xGa_{1-x}N$ layer. Since all the strain is placed in the $Al_xGa_{1-x}N$ on top of the GaN, both spontaneous and piezoelectric polarization must be considered for the AlGaN layer. Thus, total polarization P is described as the sum of spontaneous P_{SP} and piezoelectric polarization P_{PZ}, which is expressed as [12]

$$P = P_{SP}(T) + P_{PZ}(T, S), \tag{2.2}$$

where S is the strain in the crystalline structure and T is the temperature. Spontaneous polarization is only a factor of temperature, whereas piezoelectric polarization is a function of both temperature and strain on the crystalline structure. For an AlGaN/GaN heterostructure, the total spontaneous polarization of the AlGaN alloy $P_{SP,AlGaN}$, of mole fraction x, is a composition of the polarization of the aluminum nitride (AlN) P_{AlN}, the polarization of GaN P_{GaN}, and a bowing parameter BP. The relationship between the polarization and bowing parameter is given as [12]

$$P_{SP,AlGaN} = xP_{SP,AlN} + (1 - x)P_{SP,GaN} - BPx(1 - x), \tag{2.3}$$

while the piezoelectric polarization of the AlGaN layer is determined by

$$P_{PZ,AlGaN} = 2 \cdot \frac{a_{GaN} - a_{AlGaN}}{a_{AlGaN}} \left(e_{31} - e_{33} \frac{C_{31}}{C_{33}} \right). \tag{2.4}$$

In equation (2.4), e_{31} and e_{33} are the piezoelectric coefficients of AlGaN, while C_{31} and C_{33}

are the elastic constants of AlGaN. The total polarization of the AlGaN layer is essential in determining the charge-sheet concentration of the 2DEG that forms in the heterojunction.

2.2.3   2DEG Formation and Control

When a heterojunction is formed between two different III-Ns of different lattice constants, there is a piezoelectric polarization that develops a virtual charge around the strain interface [9]. A polarization vector forms in the c-direction of growth due to the spontaneous polarization from the group (III-N) semiconductor. This polarization results in the appearance of a net-positive charge along the interface which creates a dipole that strips electrons from the top side of the AlGaN and sweeps them to the GaN side. These electrons are the source of the charge carriers within the 2DEG of the device [9]. These carriers build up in a quantum well which forms at the interface of the AlGaN and GaN layers of the heterojunction. This sheet-charge formation is called a 2DEG and is quantum confined in the c-direction, which is defined as the lateral direction of crystalline growth. The equilibrium band diagram of the GaN/AlGaN heterojunction along with the 2DEG that forms from the contact is represented in Figure 2.2.
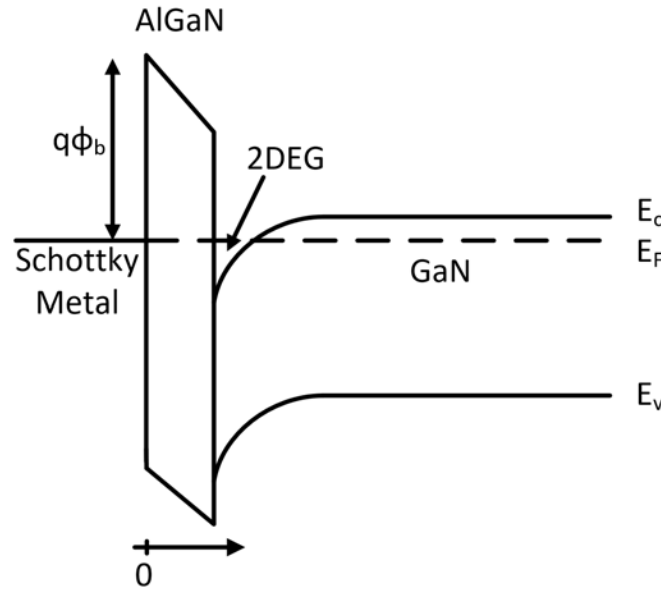
Figure 2.2. Equilibrium Band Diagram of GaN/AlGaN Heterojunction

The band diagram shows the metal-Schottky contact on the left and then the AlGaN and GaN layers in sequence with the formation of a 2DEG in between. From the equilibrium

11

band diagram of the AlGaN/GaN heterojunction, it can be seen exactly where the 2DEG forms in relation to the conduction-energy band E_c, the valence-energy band E_v, and the Fermi-energy level E_F. The barrier height ϕ_b is the potential difference between the Schottky metal and the AlGaN layer which is in units of V when multiplied by the electron charge q. An electric field forms across the AlGaN layer that sweeps electrons toward the AlGaN/GaN interface, dipping the conduction band at the interface below the Fermi-energy level in a "valley" formation [13]. This "valley" confines electrons in discrete energy ranges and constrains them to a quantum-planar motion within the device. This conglomeration of electrons allows a high-electron density with high mobility to form within the 2DEG [13]. The density of the electrons within the 2DEG can be controlled by applying a gate voltage to the Schottky contact. The quasi-Fermi level of the metal will increase on the diagram if a negative gate voltage is applied. It is important to note that electric field is the inverse of the voltage potential gradient; therefore, a negative voltage coincides with a higher gate-Fermi level [14]. The quasi-Fermi energy level of the GaN will not change since the energy levels of the GaN far from the interface do not change relative to each other. The barrier height of the Schottky metal does not change when a negative bias is applied; therefore, by putting a larger negative voltage on the gate, it will eventually pull the conduction band out from beneath the Fermi-energy level. The negative gate bias diminishes the quantum well, depleting the 2DEG of electrons due to the increase in the conduction-band edge. The equilibrium electron concentration of the 2DEG n^o_{2DEG} is sensitive to the difference in polarization ΔP between the two materials in question, the difference of the conduction-band energy ΔE_c, and the barrier height of the material ϕ_b [11]. The equilibrium-charge density Q^o_{2DEG} is given as [12]

$$Q^o_{2DEG} = C_{eff}\left(\phi_b - \frac{\Delta P}{C_{AlGaN}} - \frac{\Delta E_c}{q}\right), \qquad (2.5)$$

where effective capacitance C_{eff} is defined as

$$C_{eff} = \frac{C_{AlGaN}C_q}{C_{AlGaN} + C_q}. \qquad (2.6)$$

The capacitance of the AlGaN layer C_{AlGaN} is defined as the permittivity of AlGaN over

the thickness of the AlGaN layer. C_q is known as the quantum capacitance of the device and is calculated as

$$C_q = q^2 D_{2DEG}, \tag{2.7}$$

where D_{2DEG} is the density of states in the 2DEG. The charge density leads to the calculation of the 2DEG concentration by

$$n^o_{2DEG} = \frac{Q^o_{2DEG}}{-q}, \tag{2.8}$$

and the voltage threshold by

$$V_{TH} = \frac{Q^o_{2DEG}}{C_{AlGaN}}. \tag{2.9}$$

The next step is to look at how the gate controls the concentration of the 2DEG now that the equilibrium-2DEG concentration has been defined. The concentration of the heterojunction 2DEG versus a gate voltage is expressed as [12]

$$n_{2DEG} = -\frac{1}{q}C_{eff}(V_g - V_{th}), \tag{2.10}$$

where V_g is the applied gate voltage to the heterojunction and V_{TH} is the threshold voltage. The primary benefit that III-N heterojunctions provide is the lack of doping used to generate the 2DEG. Instead, the charge carriers come from the donor surface states at the top of the AlGaN layer due to polarization between the two semiconductor layers. This process provides carriers without hindering the mobility of the 2DEG through the introduction of impurities as dopants. The electron mobility μ_n is an imperative characteristic of a semiconductor device and can be described as [18]

$$\mu_n = \frac{q\tau_n}{m^*_n}, \tag{2.11}$$

where q is the charge of an electron, τ_n is the scattering lifetime, and m^*_n is the effective

mass of an electron within the material. Increasing dopants in a semiconductor decreases the scattering lifetime, consequently decreasing mobility, because of carrier scattering from ionized dopants. The mobility in GaN/AlGaN heterostructures is elevated above the mobility of bulk GaN due to the minimization of scattering within the 2DEG [19].

2.3   GaN HEMTs

HEMTs have been traditionally used in high-frequency and high-power applications due to high mobility and high electron densities within the 2DEG channel. HEMTs are fabricated by depositing Schottky metal for the transistor gate onto an epitaxially-grown semiconductor heterojunction, in which a 2DEG has formed, and depositing metal for ohmic contacts on either side of the gate, forming the drain and source. The 2DEG acts as the channel for the electrons to travel from source to drain [10]. Figure 2.3 is an illustration of a GaN/AlGaN HEMT with the transistor leads and resistances overlaid.
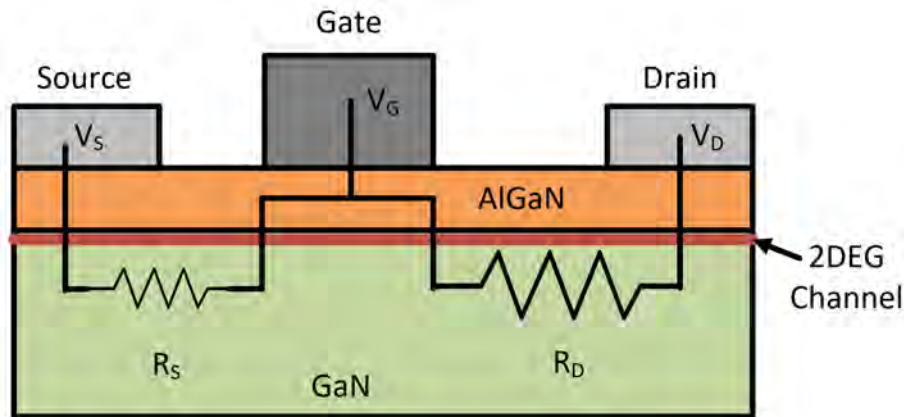
Figure 2.3. Illustration of the Cross Section of a GaN/AlGaN HEMT

2.3.1   DC Characteristics

When discussing the electrical characteristics of GaN HEMTs it is important to fully understand links between the 2DEG concentration and the voltage level applied to the drain and gate. The presence of the 2DEG will be independent of the presence of contact metallization, Schottky or otherwise, since the 2DEG forms due to the polarization between the GaN and AlGaN [13]. A gate voltage must be applied across a Schottky contact to deplete the 2DEG in order to control the magnitude of the 2DEG, as explained in the

previous section. To achieve current flow through the channel, a voltage V_D must be applied to the drain. If the gate length L is longer than a few microns, the voltage drop across the channel $V(x)$ significantly reduces the electron density within the channel [12]. The relationship between 2DEG concentration and gate voltage from equation (2.10) is adjusted to account for the creation of a channel between the source and drain contacts. The adjusted equation is expressed as [12]

$$n_{2DEG}(x) = -\frac{1}{q}C_{eff}(V_g - V_{th} - V(x)). \tag{2.12}$$

Thus, the electron concentration of the 2DEG decreases across the channel from source to drain. We assume that the current through the channel only consists of electron drift current in order to derive an equation for the drain current. We can show that due to the drift current to electron concentration relationship, the current at any point x in the channel is given by [11]

$$I_n = \mu_n C_{eff}(V_g - V_{th} - V(x))\frac{dV(x)}{dx}, \tag{2.13}$$

where μ_n is the electron mobility and $\frac{dV(x)}{dx}$ is the rate of change of the potential over distance along the channel in the structure. This equation can be integrated over the length of the gated channel and multiplied by the channel width Z to get an equation for the drain current I_D with respect to the gate and drain voltage

$$I_D = \frac{Z}{L}\mu_n C_{eff}\left((V_g - V_{th})V_D - \frac{V_D^2}{2}\right). \tag{2.14}$$

An example of the drain current versus drain voltage V_D relationship for increasing gate voltages is given in Figure 2.4.

15
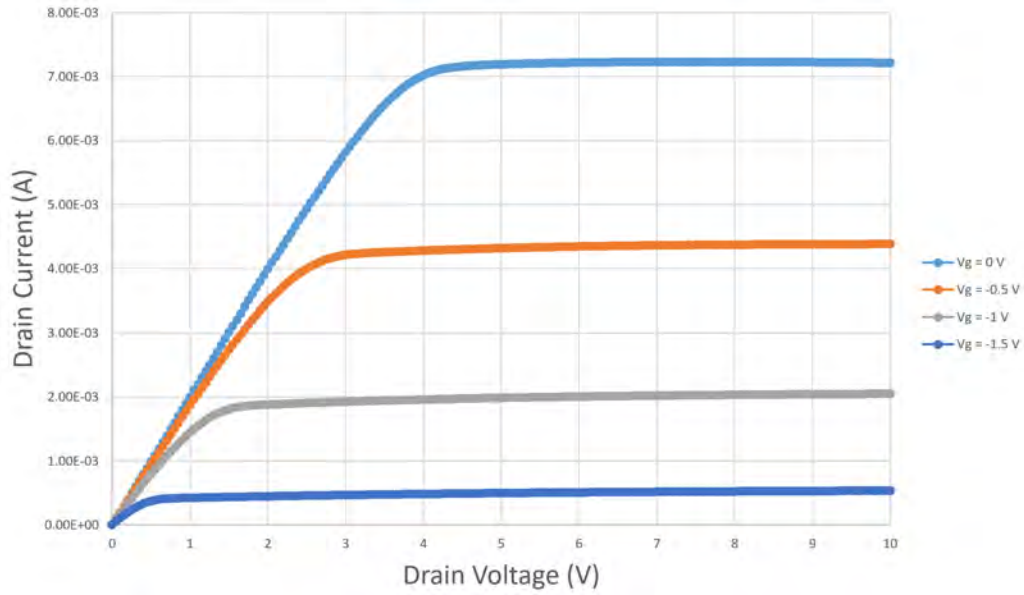
Figure 2.4. Id-Vd Relationship of a GaN/AlGaN HEMT

Note that the magnitude of the drain current increases as gate voltage increases, and that there is a saturation of the drain current at higher drain voltages. Several regions of operation can be determined from Figure 2.4 and equation (2.14). At low drain voltages, the drain-current relationship is linear in both V_d and V_g, which denotes the triode region of the device [14]. In this region, the device effectively operates as a gate-controlled resistor. The relationship between drain current and gate voltage can also be plotted. The Id-Vg plot demonstrates the sharp dependence upon gate voltage, with drain current rapidly decreasing below the threshold voltage, and the linearly increasing above the threshold. An example is displayed in Figure 2.5. These plots can be used to extract the threshold voltage and the effective electron mobility, which will be explored in Chapter 5. In addition, it can be seen on the plot that the drain current remains low at low gate voltages and increases linearly from about -2 V to about -1 V where it then cuts off and saturates due to the effects of the access resistance.
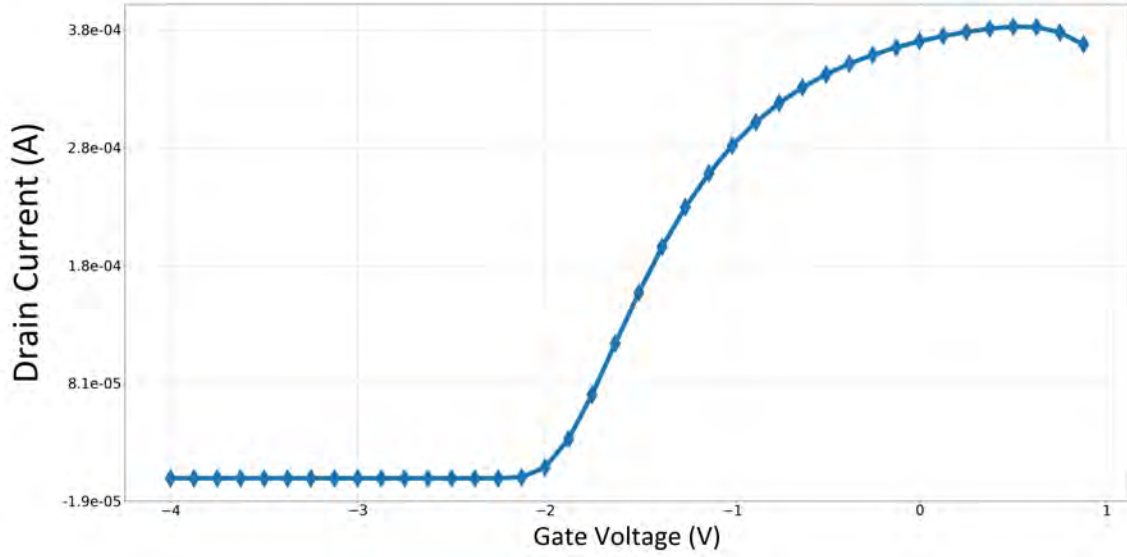
Figure 2.5. Id-Vg Relationship of GaN/AlGaN HEMT at a Drain Voltage of 100 mV

2.3.2   Access Resistances

There is an access resistance for both the drain and the source side which modify the relationship of the drain current with the applied source and drain voltage. The access resistances of HEMTs are the sum of the interface resistance of the ohmic contact, the resistance of the 2DEG region, and the resistance from the drain/source contacts to the gate-contact edge [12]. The distance of the drain/source from the gate is a key parameter in the magnitude of the access resistance, as the ohmic-contact interface resistance is usually small. These resistances cause voltage drops across them that lowers the actual voltage that the gated part of the HEMT sees. The drain access resistance R_D can be calculated as [12]

$$R_D = \frac{L_{gd}}{qn^o_{2DEG}\mu_n z},\tag{2.15}$$

and similarly the source access resistance R_S is defined as

$$R_S = \frac{L_{gs}}{qn^o_{2DEG}\mu_n z}.\tag{2.16}$$

17

The access resistances are directly proportional to the length from the gate to the drain L_{gd} and the length from the gate to the source L_{gs}. It can be seen that the resistances inversely depends upon the concentration of the 2DEG and mobility. The effect of these resistances is to modify equation (2.14) to

$$I_D = \frac{Z}{L} \mu_n C'_{eff} \left((V'_g - V_{th})V'_D - \frac{V'^2_D}{2} \right),$$
(2.17)

where

$$V'_D = V_D - I_D(R_D + R_S),$$
(2.18)

and

$$V'_g = V_g - I_D R_S.$$
(2.19)

In equation (2.19), V'_g is the gate voltage referenced to the gate edge on the source side and V'_D is the voltage at the gate edge on the drain side. The effect of the access resistance is to reduce the effectiveness of the gate and drain in controlling the drain current for high drain current magnitudes [12]. Because of this effect, the resistances change due to defects or other types of damage within the device. The applied voltages that the HEMT will see will be altered and ultimately affect the drain current through the device.

2.3.3   Gate Leakage Current

If the gate is forward biased, large amounts of current can flow through the gate because the gate of a HEMT is a Schottky diode. This behavior is unlike that found in other field-effect transistors such as MOSFETs which have an oxide for an insulated gate [12]. Utilizing Kirchhoff's current law, it is understood that the drain current is the sum of the source and gate currents within the HEMT. The saturation current I_o depends exponentially upon the barrier height of the Schottky diode. The gate current I_G is related to I_o and can be calculated as [12]

$$I_G = I_o \left(e^{\frac{qV'_G}{\eta kT}} - 1 \right). \tag{2.20}$$

The gate current is dependent upon the gate voltage as well as the saturation current I_o and the ideality factor η. The ideality factor is a correction factor that represents the divergence of the actual gate current from the ideal gate current equation. The Boltzmann constant is k, while T represents the temperature. An example of the gate characteristics of a HEMT at 100 mV drain voltage is shown in Figure 2.6.
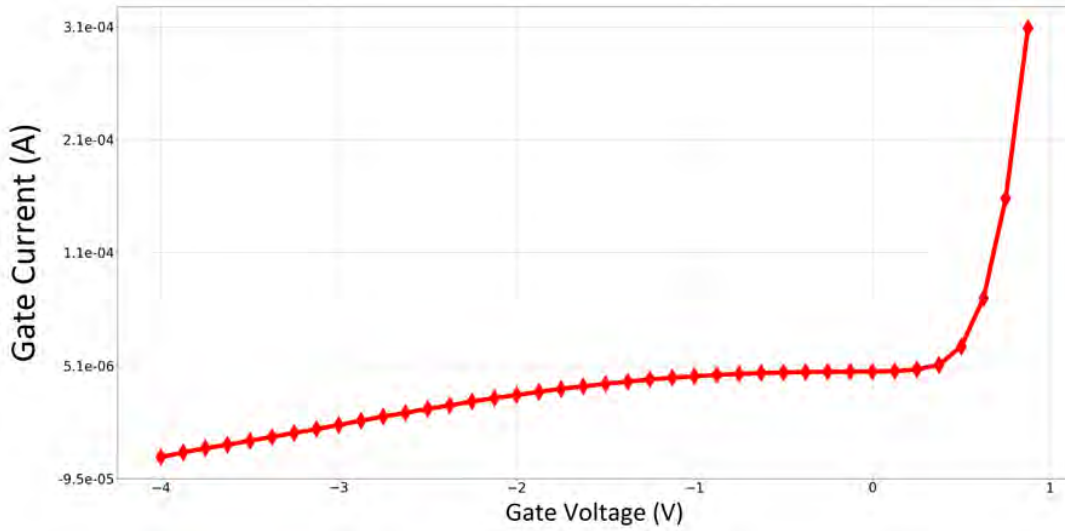
Figure 2.6. Ig-Vg Plot of a GaN/AlGaN HEMT

The gate current remains low at lower gate voltages; however, the device acts like a diode with increasing current when the gate voltage is brought above 0 V.

2.3.4 Drain Current Collapse and Dynamic R$_{\text{DS,on}}$

A key focus of this experiment is the characterization of the state of defects and traps within GaN-on-Si HEMTs and how these defects change when increasing neutron fluence. The measurement of defect-induced device responses can provide valuable insight into the effects of radiation upon the defect state of the device. One such effect is dynamic on-state resistance. Dynamic on-state resistance is defined as the transient increase in the resistance of the device channel based on the application of a reverse-bias high-voltage stress to the

19

drain-gate access region [20]. This measurement probes the traps at the edge of the gate on the drain side by stressing the device in the off-state with a high drain voltage. Stressing the gate-drain access region sweeps the electrons out of the region leaving positively charged ions that effectively extend the length of the gate by allowing a voltage drop across the depletion layer [16]. The increase of the depletion layer length with a higher stress voltage causes the increased resistance of the region due to the increase in voltage drop. When the stress is removed from the device and returned to an on-state biasing, the electrons are swept back into the depletion region and recombine. This recombination lowers the resistance of the access region due to the lowering of the voltage drop. The increase in resistance within the channel effects the IV characteristics by collapsing the drain current during the stressing period. The current recovers when the device is held in the on-state, allowing the electrons to recombine into the depletion region. The representation of the IV characteristics that evolve from the current collapse is illustrated in Figure 2.7.
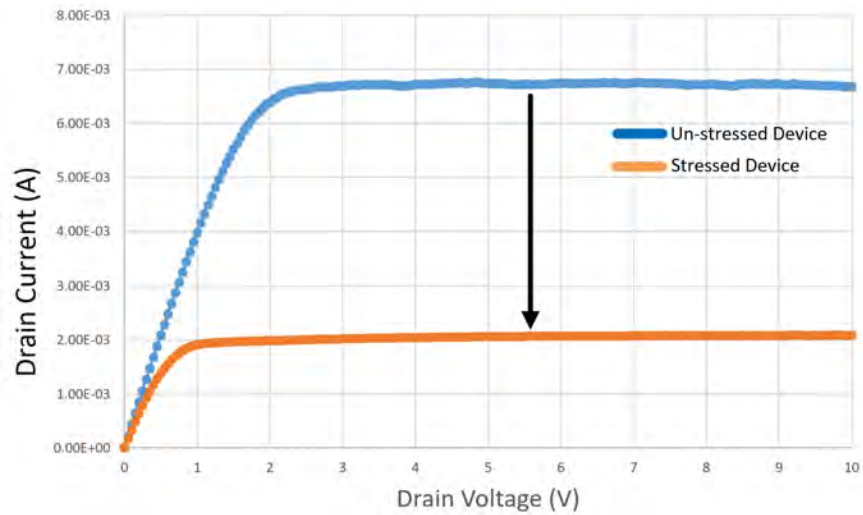
Figure 2.7. Id-Vd Plot Showing the Drain Current Collapse Immediately after a Stressing Period on the Tested GaN-on-Si HEMTs

The collapse in current can be seen by the magnitude drop between the blue and orange curves of the figure. The slope of the linear region is also lower which means the resistance has increased causing the lowering of the saturation current. This stress fills the traps with electrons from the gate edge causing a depletion layer L_{dep} between the gate and the drain on the surface of both the AlGaN and GaN layers. This depletion layer causes a virtual-gate extension due to the extra charge from the ionized atoms and when the device is turned on,

the electrons recombine with the ionized atoms [16]. This means there are two electric fields within the device, one due to the depletion layer, and one due to the potential difference between gate and drain. Assuming the entirety of the electric field is within the depletion layer, the electric field for the depletion layer is given as [16]

$$E_0 = \int_0^{L_{dep}} \frac{\sigma_T}{2\pi\epsilon} \frac{t-x}{r^2 + (t-x)^2} dt,$$ (2.21)

where σ_T is the charge due to polarization, r is the distance laterally from the GaN/AlGaN interface, x is the distance from the gate, and t is the constant of integration for the line charges. The calculation for the electric field E' can also be calculated across the drain to gate region due to the applied voltage which is given as [16]

$$E' = -\frac{V_{DG}}{L_{dep}}.$$ (2.22)

The potential from the drain to the gate V_{DG} and the sum of the two electric fields results in the total electric field seen by the HEMT due to the virtual-gate extension and the biasing. Using the sum of the electric fields and the assumption that the voltage drop between the drain and gate is only across the depletion layer, the length of the depletion layer L_{dep} can be determined by assuming that the total field drops to zero at L_{dep}. An illustration of the virtual lengthening of the gate due to the depletion of electrons is shown in Figure 2.8 along with the shrinking of the depletion layer when the device is put in the on-state, and the trap states capture electrons. The device is stressed using a high drain voltage and low gate voltage which creates a depletion region shown on the left. The electrons recombine which shrinks the depletion layer when the device is put in the on-state, as shown in the right plot of Figure 2.8.
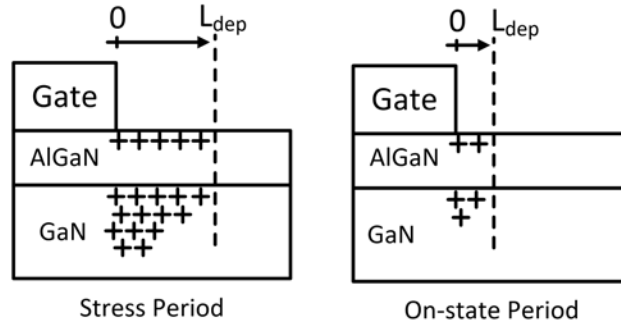
Figure 2.8. Animation of Virtual Gate Extension in HEMT

2.4   Radiation Effects in GaN Devices

It is important to distinguish between two types of radiation damage, ionizing and non-ionizing radiation damage, when studying radiation effects. Ionizing radiation damage occurs when radiation collides and transfers energy to the electrons within a material [4]. Non-ionizing radiation damage occurs when radiation displaces atoms within a material by colliding and knocking it out of place [4]. With most irradiation, high-energy massive particles are considered both ionizing and non-ionizing because they do both these effects while moving through a material. Protons are charged particles with a significant mass; therefore, they have the ability to move electrons from their original positions as well as collide with a nucleus causing it to be displaced. It is assumed that neutrons only cause non-ionizing damage themselves when discussing neutron damage within GaN, but secondary particles from nuclear reactions may still cause ionizing damage through the device.

2.4.1   Non-ionizing Radiation Damage

The cross section of interaction needs to be defined in order to understand how non-ionizing radiation damages materials. The cross section is a measurement of the probability of a particle interaction [21]. Specifically, the probability of an interaction between two atoms is imperative to understand because it defines the likelihood of a particle to cause an atom to be displaced within a material. The classical representation of the displacement damage event can be shown as two atoms colliding and undergoing elastic scattering. The initial displacement event can cause the secondary atom, known as a primary knock-on atom (PKA), to continue through the material displacing other atoms within the material [21]. Figure 2.9 is an illustration of the initial collision event and the resulting chain reaction of

22

secondary displacements created by PKAs.
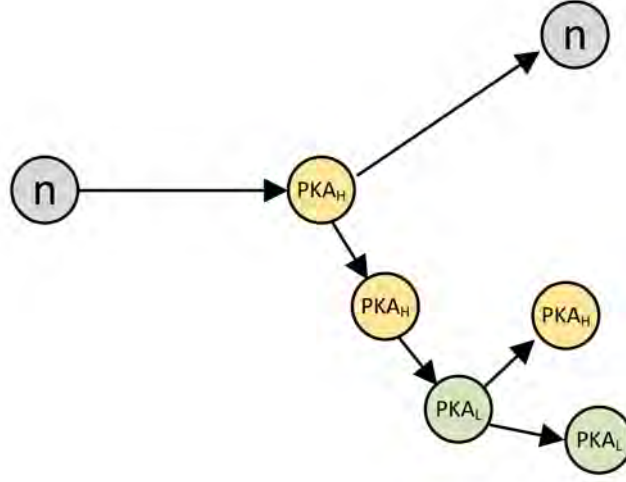
Figure 2.9. Illustration of the Collision Event and PKA Generation

In Figure 2.9, n is the high-energy neutron, while PKA_H is a high-energy PKA and PKA_L is a low-energy PKA. The arrow lengths represent the inverse relationship to the cross section for the specific particle, which means longer arrows represent lower cross sections. The mean distance between scattering events gets longer when there is a lower probability of interaction between two atoms. The shorter arrows represent a higher cross section and therefore a shorter time between interactions in the material. In Figure 2.9, while a neutron was used as the initial incoming particle, any particle with high energy could be used to show the displacement that occurs within materials. Non-ionizing radiation damage from heavy particles is generally described with elastic scattering and therefore elastic cross sections due to their large mass and low probability of causing nuclear reactions within the displaced nuclei. The equation for the maximum transferred energy T_M to a PKA through non-ionizing damage is given as [21]

$$T_M = \frac{4M_1 M_2}{(M_1 + M_2)^2} E_o,$$
(2.23)

where M_1 is the mass of the incoming particle, M_2 is the mass of the secondary particle, E_o is the energy of the incoming particle, and θ_c is the collision angle. These collisions caused by high-energy particles interacting with the nuclei create damage within semiconductors

through various means.

Dislocations, implantations, and clustering can all occur due to the displacement of atoms within the material [22]. The effect of these defects can cause major changes in the device characteristics by doping a layer with impurities, blurring interfaces, and creating voids within layers. In GaN HEMTs specifically, doping the AlGaN layer with impurities could alter the formation of the 2DEG by mitigating the effect of the inherent dipole created when GaN and AlGaN interface [13]. Blurring interfaces could result in decreased capacitance under the gate or extra pathways for current to take throughout the HEMT. Voids under the gate could severely degrade the mobility of the HEMT by increasing resistance along the channel. Neutrons behave differently since the angle of scattering is independent of the incoming-particle energy and the transferred energy; therefore, neutrons will have different atomic relationships due to their lack of charge and increased probability of nuclear reactions.

2.4.2   Neutron Displacement Damage

The first difference to note about neutron damage compared to other non-ionizing radiation is that the cross section of neutron damage is independent of the scattering angle [21]. This property allows the neutrons to displace atoms within a material in a near-isotropic fashion. Since neutrons do not have a charge, they are not affected by the presence of electrons and ions unless they are in the direct path of the incoming neutron [22]. The cross section of neutrons cannot be described by just elastic cross sections because it needs to account for not only the displacement of atoms, but the possibility for a nuclear reaction that would take energy from the initial collision. An example of this type of event would be the collision of a neutron with an atom, displacing the atom, and causing an ejection of a photon in order for the nucleus to go back to a lower-energy state. The creation of a photon in this interaction took energy out of the system and made it inelastic. Taking the elastic and inelastic collision into account is critical when calculating the damage within a material.

Understanding the displacement cross section σ_D of a material for an incoming neutron at a given energy is essential when studying neutron damage within semiconductors. There are four major events that need to be accounted for when calculating the displacements due to neutrons. There are elastic neutron-to-neutron events (n, n), neutron-to-neutron due

to inelastic scattering $(n, n)^*$, neutron-to-two neutron events $(n, 2n)$, and neutron-to-gamma events (n, γ) [4]. All four events along with their PKAs need to be taken into account in order to provide an accurate model for the neutron-displacement cross section within a material. Modifying the Kinchin and Pease model to account for all four possible events, the total displacement cross section accounting for all four neutron events is expressed as [4]

$$
\begin{aligned}
\sigma_D ={}& \frac{\sigma_S(E_i)}{\gamma E_i} \int_{E_d}^{\gamma E_i} \left[\frac{1-P}{1-2P} \left(C' \zeta(T) \frac{T}{2E_d} \right)^{(1-2P)} - \frac{P}{1-2P} \right] \\
& \times \left[1 + \alpha_1(E_i) \left(1 - \frac{2T}{\gamma E_i} \right) \right] dT \\
& + \sum_j \frac{\sigma_{sj}(E_i, Q_j)}{\gamma E_i} \left[1 + \frac{Q_j}{E_i} \left(\frac{1+A}{A} \right) \right]^{-1/2} \\
& \times \int_{\check{T}_j}^{\hat{T}_j} \left[\frac{1-P}{1-2P} \left(C' \zeta(T) \frac{T}{2E_d} \right)^{(1-2P)} - \frac{P}{1-2P} \right] dT \\
& + \int_0^{E_i - E'_m} \sigma_{(n,2n)}(E_i, T) \left[\frac{1-P}{1-2P} \left(C' \zeta(T) \frac{T}{2E_d} \right)^{(1-2P)} - \frac{P}{1-2P} \right] dT \\
& + \sigma_\gamma \left[\frac{1-P}{1-2P} \left(C' \zeta(T) \frac{E_\gamma^2}{8E_d(A+1)c^2} \right)^{(1-2P)} - \frac{P}{1-2P} \right], \quad (2.24)
\end{aligned}
$$

where σ_S is the elastic cross section, E_i is the incoming-particle energy, E_d is the displacement energy for the specific atom, $\gamma = 4A/(1 + A)^2$, A is the atomic mass of the displaced atom, and P is the crystal effect. T is the transferred energy, E_γ is the gamma energy, A is the atomic mass, and C' is a correction constant.

The displacement cross section for any energy of that material can be calculated if the flux-energy spectrum of the incoming particles is known. From here the displacement rate for a given energy per unit volume can be achieved by multiplying the displacement cross section by the incoming-particle flux at a specific energy. The total displacement rate R is then expressed as [4]

$$R = N \int_{E_{min}}^{E_{max}} \sigma_D(E_i)\Phi_n(E_i)dE, \qquad (2.25)$$

where Φ_n is the neutron flux at a given particle energy. The displacement rate allows us to calculate the number of displacements within a given material per second and therefore the total number can be easily found using the total time interval of irradiation. This rate can then be correlated with changes in material and device characteristics.

As an example, the neutron cross section for interaction within Ni is shown in Figure 2.10 to decrease as the energy of the neutron increases with a resonance region between 100 eV and 100 keV incoming-neutron energy.
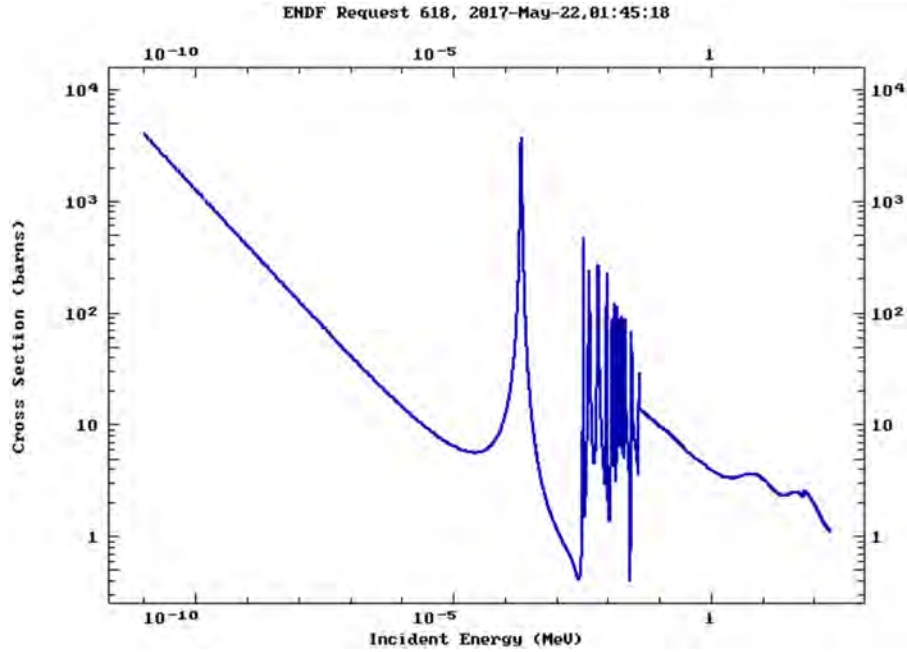
Figure 2.10. Total Neutron Cross Section for Interaction within Ni. Source: [23].

Utilizing Figure 2.10 and equation (2.23), the neutron-displacement cross section can be determined at all energies within Ni. The plot of displacement energy versus incoming-neutron energy within Ni is represented in Figure 2.11.

The displacement cross section increases with neutron energy even though the neutron cross section for interaction decreases. This relationship occurs because the displacement from a

26
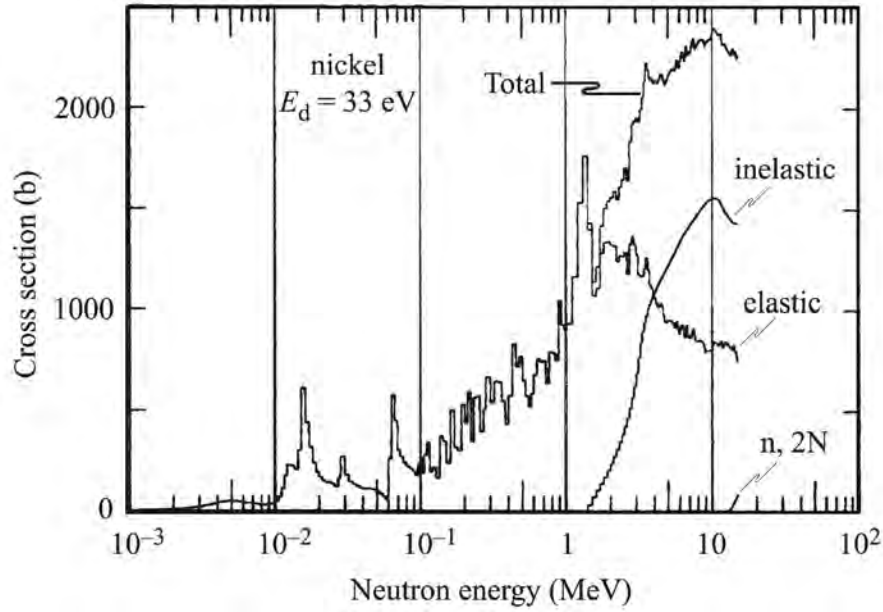
Figure 2.11. Neutron Displacement Cross Section for Ni. Source: [4].

high-energy collision will cause a large cascade of displacements from the PKAs produced in the initial interaction even though the probability of a high-energy neutron is lower than that of a lower-energy neutron.

2.5 Neutron Damage in GaN Devices

Before explaining the design of this experiment it is important to discuss the previous experiments conducted on neutron damage in GaN devices and their findings. There has been a big push for the understanding of neutron radiation damage in GaN devices since about 2005, when Polyakov irradiated GaN-on-Sapphire AlGaN/GaN heterojunctions with an equivalent of 1-MeV neutrons to a fluence of $1.7 \cdot 10^{17} n/cm^2$ [24]. This experiment was completed at a WWR-c-type reactor at the Karpov Institute by irradiating a number of devices to different fluences of neutrons and measuring their characteristics before and after the experiment. It was found that the change in the device characteristics began after around $10^{14} n/cm^2$, and the 2DEG concentration remained stable until about $1 \cdot 10^{17} n/cm^2$ [24]. A deep-level optical spectroscopy (DLOS)/deep-level transient spectroscopy (DLTS) system was utilized the characterize the trap energies within the GaN devices, and it was shown that a 0.21-eV trap energy was observed at low fluence. At higher fluence, the traps energies

27

were at 0.3 eV and 0.45 eV which correlated to two different damage products within the device [24].

After Polyakov found the major changes in device characteristics at high fluences of high-energy neutrons, known as fast neutrons, the study of this type of radiation on GaN material was desired. In 2006, Polyakov utilized a fast reactor to irradiate MOCVD and MBE grown undoped n-GaN films with fast neutrons up to $1 \cdot 10^{18} \text{n/cm}^2$ [25]. Polyakov discovered that the Fermi level within GaN was locked in the 0.8 to 0.95 eV range independently of the initial purity of the GaN [25]. Polyakov hypothesized that this demobilization of the Fermi level in irradiated GaN was caused by gallium interstitials acting as donors at the 0.8-eV energy level and nitrogen interstitials acting like acceptors in the 0.95-eV energy level [25]. The interstitials theoretically created a virtual floor and ceiling for the movement of the Fermi level within GaN.

In 2007, Polyakov looked at the irradiated undoped n-GaN films before and after receiving a fluence of $1 \cdot 10^{18} \text{n/cm}^2$ [26]. In this experiment, Polyakov looked at the trap states that form within the GaN due to high fast-neutron fluence. It was found that these devices developed deep traps states at 0.75 eV [26]. There was also the development of strong photocapacitances that persisted throughout the devices. This result was hypothesized to be due to the high-energy displacement damage caused by the fast neutron flux [26]. This experiment also verified the pinning of the Fermi level at around 0.85 eV, as was previously seen.

Continuing the research into neutron damage in GaN devices, in 2009, Petrosky irradiated AlGaN/GaN heterojunction field-effect transistors (HFETs) up to a fluence of $1 \cdot 10^{12} \text{n/cm}^2$ when the devices were cooled to 85 K [27]. This experiment looked at studying the effects of the radiation on the gate leakage and provide a theory toward how the damage occurs. The gate leakage was fit using a four-parameter-thermionic-trap-assisted tunneling model to discover the trap concentration and energy within the device [27]. It was discovered that the trap concentration had increased by 25 percent while the mean trap energy increased by 7 mV. The hypothesis behind this discovery was that the neutrons were undergoing elastic collision under the gate in the AlGaN region causing defects that increased trap numbers and energy [27].

In 2010, Polyakov conducted another neutron experiment that irradiated the same undoped-

GaN films as before, but to a neutron fluence of $1.5 \cdot 10^{17} \text{n/cm}^2$ with equal number of low-energy neutrons, known as thermal neutrons, and fast neutrons [28]. The experiment was designed to look at damage differences between thermal and fast neutrons as well the annealing of the damage at different temperatures. It was found that the GaN films underwent a slight recovery of conductance when heated to between 200°C and 300°C. A reversal of annealing occurred from temperatures between 300°C and 500°C, and a broad-spectrum recovery took place at temperatures between 800°C and 1000°C [28]. The major discovery found from this experiment was that the damage from the thermal neutrons caused activation within the material by a transmutation of Ga to Ge as the thermal fluence increased to $2 \cdot 10^{16} \text{n/cm}^2$ [28]. The transmutation improved the performance of the devices at low fluences.

That same year, Gu irradiated SiN passivated AlGaN/GaN HEMTs to a 1-MeV neutron fluence of $1 \cdot 10^{15} \text{n/cm}^2$. Gu wanted to measure the electrical characteristics of SiN passivated devices in order to compare the characteristics of passivated and non-passivated devices and explore whether a passivation layer would help with the radiation hardness of the device [29]. It was found that the passivation layer indeed mitigated some of the degradation of the device by capturing some of the neutrons, causing defects in the passivation layer before they reached the device layers [29]. It was also shown that the transconductance degraded significantly due to the decrease in mobility. The reverse gate leakage also increased as the fluence increased from 10^{14} to 10^{15}n/cm^2. Based on these results, it was discovered that the gate region was more sensitive to the radiation than the access regions due to defects that occurred in the passivation layer [29].

The electrical characteristics of AlGaN/AlN/GaN HEMTs and InAlN/GaN HEMTs were compared in 2012 by Polyakov after being irradiated by 2-MeV neutrons to a fluence of $3 \cdot 10^{15} \text{n/cm}^2$. This experiment was conducted at a fast reactor, and it was found that the 2DEG mobility decreased while the threshold voltage shifted right [30]. This degradation was found in both HEMTs; however, it was discovered that HEMTs with a higher concentration of Al in the AlGaN layer were less radiation hard toward neutrons. The higher sensitivity to radiation occurred because the AlGaN layers that had higher concentrations of Al had a higher cross section which caused an increase number of traps to form from the displacement damage [30].

Also in 2012, Berthet irradiated AlGaN/GaN HEMTs to a low thermal-neutron fluence of $4.3 \cdot 10^{10}$ n/cm^2 and a low fast-neutron fluence of $1.8 \cdot 10^{12}$ n/cm^2. At these low fluences, the devices had improved characteristics with higher drain currents and decreases in access resistances [31]. The plot of the change in drain current shown in blue and on-state resistance shown in red given fast-neutron fluence is given in Figure 2.12.
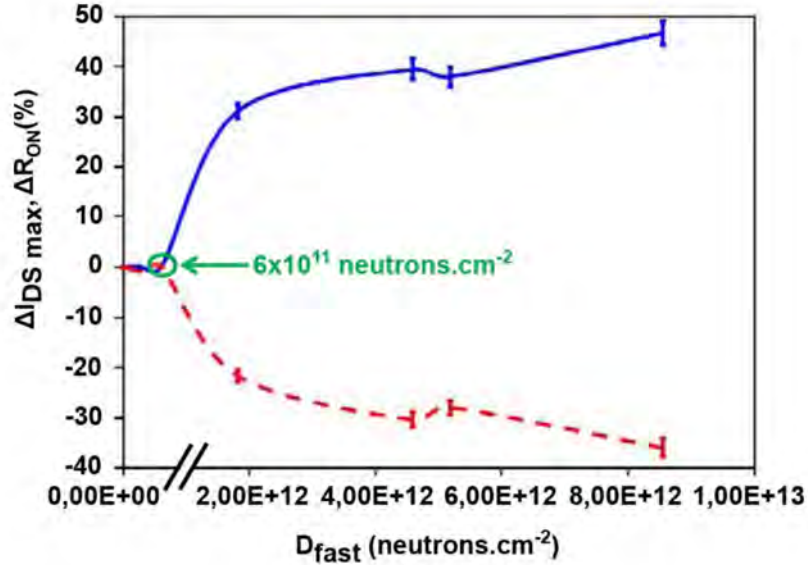
Figure 2.12. Graph of the Drain Current (blue) and On-State Resistance Changes (red) versus Fluence for a GaN/AlGaN HEMT. Source: [31].

This decrease in resistance and increase in drain current denotes an improvement from the thermal neutrons, which was associated with the Ga-Ge transmutation that was previous discovered by Polyakov. The improvement of device characteristics from fast neutrons was described as a function of the nitrogen vacancies and changes in the strain between the layers which occurred due to the high-energy displacement damage [31].

GaN-on-Sapphire Schottky diodes were explored in 2013 by Lin that used the OSU research reactor to irradiate the silicon doped GaN Schottky diodes with a neutron flux of $5 \cdot 10^{12}$ n/(cm$^2 \cdot$s) and a total fluence of $1.2 \cdot 10^{16}$ n/cm^2 for fast and $2.8 \cdot 10^{16}$ n/cm^2 for thermal neutrons [32]. It was discovered that the thermals caused metallurgical reactions to occur at the metal interfaces, while the fast neutrons caused displacement damage throughout the device. Lin took SEM images of the devices and found that the metallurgical reactions cause diffusion of the metal into the GaN. The device sensitivity to temperature showed that

temperatures would anneal damage causing a slight recovery in the device [32].

Berthet conducted a recent experiment in 2016 that irradiated AlGaN/GaN HEMTs, AlInN/GaN HEMTs, and AlInN/GaN metal-oxide semiconductor (MOS) HEMTs with a low-neutron fluence of $6 \cdot 10^{11}$n/cm^2 [33]. Berthet took an interesting approach by stressing half of the devices with a high voltage off-state period and keeping the other half of the devices unstressed [33]. The results showed that the stressed devices had increased drain current over the course of the irradiation, while the unstressed HEMTs had decreased drain current over the course of the experiment. This increased current denotes an improvement in the devices, and the decreased drain current was due to the degradation of the devices. The improvement and degradation was measured through the amplitude of the drain current achieved by sweeping drain voltage. A higher drain current was measured after irradiating the stressed devices, and a lower current was measured for the unstressed devices [33]. The difference between the stressed and the un-stressed devices response to irradiation can be explained by the effect of the stress on the trap states of the device. Stressing the device caused trap states to be filled with electrons, temporarily lowering the drain current. Irradiating the stressed devices caused the electrons to be emitted from the traps, increasing the drain current. The unstressed devices did not have the filled traps like the stressed devices, so they showed linear degradation, as would be expected from neutron radiation [33]. This Id-Vd relationship is shown for the stressed and non-stressed HEMTs before and after the irradiation in Figure 2.13. The solid-blue lines represent the data before the irradiation, and the dashed-red lines are the characteristics after the irradiation.
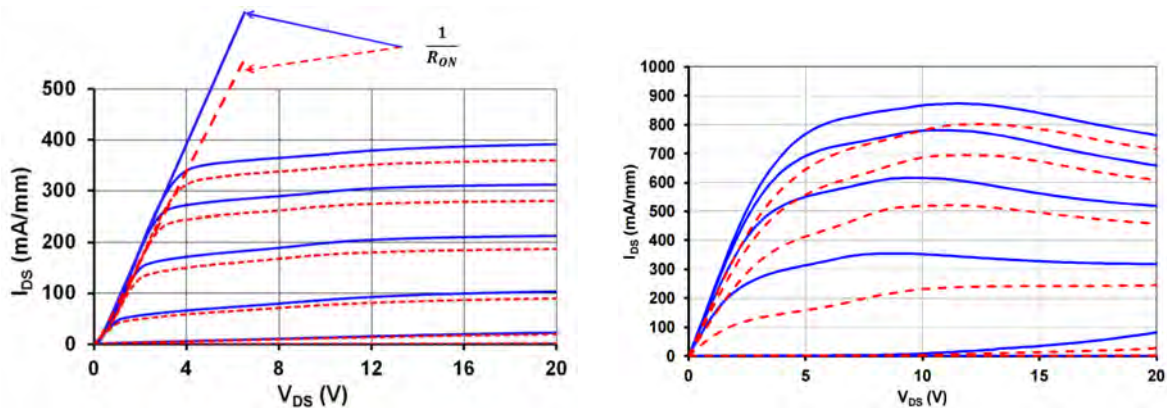
Figure 2.13. Id-Vd Plot of Before (blue) and After (red) Radiation for Stressed HEMT (left) and for the Unstressed HEMT (right). Source: [33].

31

A road map of how neutron damage effects GaN devices can be made and utilized when analyzing the results of this experiment by comparing the results of these experiments and noting the differences and similarities. The next chapter introduces the physics behind the neutron source used in this thesis work and describes the design of the experiment conducted to optimize fast-neutron flux.

CHAPTER 3:
Design and Testing of a High-Flux Fast-Neutron Photoneutron Converter

As previously discussed in Chapter 2, GaN is a radiation-hard material due to its wide band gap and its high-displacement threshold energy. While GaN devices have been extensively studied under gamma, beta, and proton irradiation, the research into high-fluence fast-neutron damage in GaN devices is lacking. To perform fast-neutron irradiation of GaN devices, high-flux neutron sources are required in order to achieve high neutron fluence in a reasonable time-frame. This chapter will discuss the advantages and disadvantages of each type of fast-neutron source, explaining the differences between reactor-based and accelerator-based sources. The physics of the photonuclear effect, which underpins LINAC-based neutron sources, will then be discussed. Finally, the simulation and testing of a photoneutron converter built at NPS in conjunction with the Idaho Accelerator Center (IAC) for the purpose of irradiating GaN components will be presented.

3.1 High-Flux Fast-Neutron Sources

Nuclear reactors, spallation sources, and LINACs provide possible sources of high-flux fast neutrons, but not all are feasible to use for this experiment. The requirements for the neutron source for this experiment were a high-ratio of fast-to-thermal neutrons, high flux of fast neutrons to achieve a high fluence in a reasonable time, and the ability to run in-situ electrical experiments. Here we will consider each type of neutron source a possible candidate. As a first comparison, a flux comparison of different neutron sources is illustrated in Figure 3.1. From this figure, the different types of neutron sources are shown to cover a wide spectrum of neutron fluxes, with LINACs in the low-flux region, reactors in the mid-flux region, and spallation sources in the high-flux region. LINACs were historically the first neutron sources, as shown on the graph; however, modern LINAC sources can produce neutron-flux levels competitive with spallation sources. While this plot refers to thermal fluxes, these neutron sources can be similarly correlated to fast-neutron fluxes.
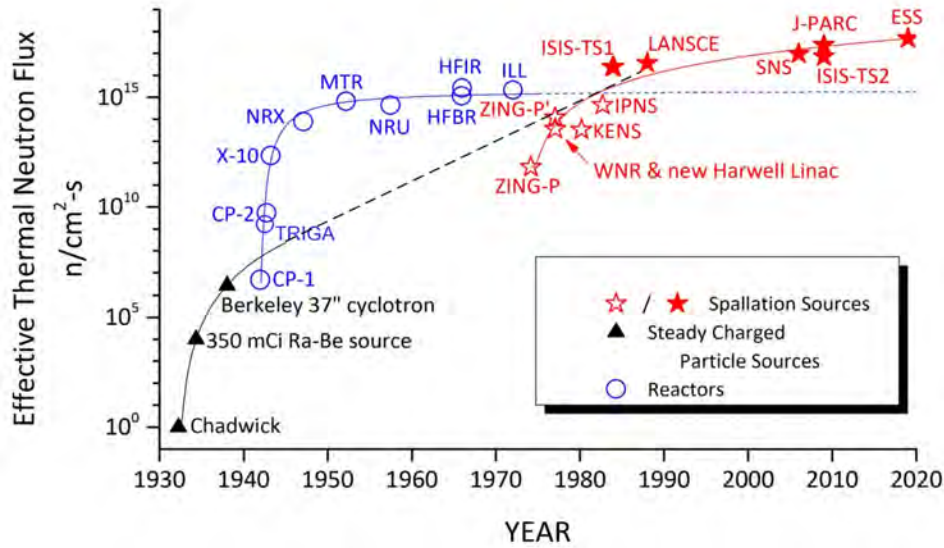
Figure 3.1. Comparison between Different Types of Neutrons Sources. Adapted from [34].

Nuclear-power plants utilize enormous amounts of neutrons in order to generate power; however, the main purpose of power reactors is to thermalize as many neutrons as possible in order to allow the fission process to feed itself and produce net energy for use [35]. By decreasing the energy of the neutrons, the cross section of the thermalized neutrons increases which allows the neutrons to be absorbed by the fuel within the reactor core [35]. Cross section is a measurement of the probability of interaction with a particle in units of barns [36]. The fuel is generally highly purified uranium-235 or plutonium-239, which are both fissile materials. The fission cross-section data based on the energy of the incoming neutron is shown in Figure 3.2. When the neutrons are absorbed by uranium-235, the stable distance between the nucleons is disrupted, which causes the nucleus to warp out of shape, making it unstable. This instability is the force that allows the nuclei to undergo fission and release an average of 2.45 neutrons per reaction [36].
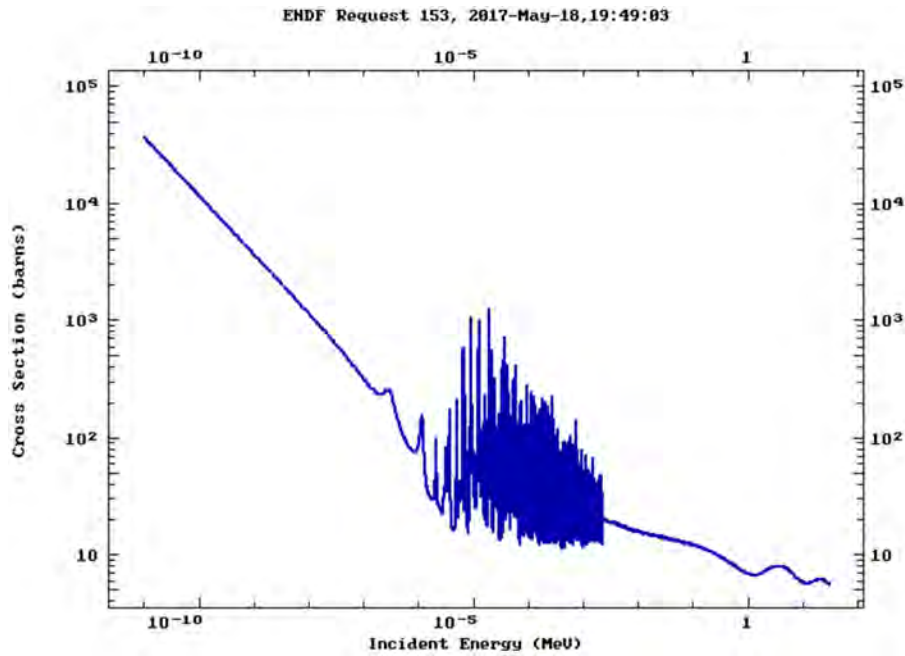
Figure 3.2. Uranium-235 Fission Cross Section Diagram based on Incoming-Neutron Energy. Source: [23].

The cross section for fission changes based on the energy of the incoming neutron; therefore, as the energy of a neutron increases its cross section decreases making it less likely to interact with the uranium nuclei. Fission reactors emit secondary neutrons at energies between 0.1 MeV and 1 MeV. These neutrons are called fast neutrons because they have energies higher than 1 eV. The fast neutrons have orders of magnitude lower fission cross sections than lower-energy neutrons which means the power reactor needs to moderate the fast neutrons in order to maintain reactor operation [35]. If the reactor is properly configured, the fast fission can be used to produce a fast-neutron source for experiment use.

A nuclear reactor that can be used as a neutron source would be a research reactor such as a TRIGA reactor. TRIGA reactors are research reactors with low-enriched fuel and easily accessible cores designed for radiation experiments. TRIGAs have a far lower flux of neutrons compared to a power-generating reactor due to the fact that TRIGA reactors use low-enriched fuel that has a lower efficiency of neutron generation compared to power-generating reactors. TRIGAs can be equipped with chambers outside the reactor core that can be shielded with boron to absorb and filter out the thermal neutrons [2]. Within these chambers, TRIGA reactors are able to achieve a total neutron flux of $6 \cdot 10^{10}$ n/(cm^2 · s)

and a fast-neutron flux anywhere between $1 \cdot 10^9$ n/(cm$^2 \cdot$ s) and $1 \cdot 10^{10}$ n/(cm$^2 \cdot$ s) [2]. This flux magnitude cannot achieve the desired fluence necessary to damage GaN devices in a reasonable amount of time.

While reactors provide a direct-neutron source, there are better sources that while indirect, provide higher-neutron fluxes with a higher fast-to-thermal neutron ratio. Spallation sources are capable of achieving fast-neutron fluxes anywhere between 10^{13} n/(cm$^2 \cdot$ s) and 10^{16} n/(cm$^2 \cdot$ s). Spallation sources collide high-energy protons with a target material with heavy nuclei in order to displace large numbers of high-energy neutrons via the direct ejection of nucleons from the nucleus. The spallation process is highly efficient at neutron production making such neutron sources the brightest ones available, but the major disadvantage is the cost. Spallation sources generally cost thousands of dollars to use per hour, which was quickly ruled out as an option for this thesis experiment.

LINACs needed to be investigated as an alternative neutron source since reactors and spallation sources were ruled out as possible neutron sources that could be utilized for this experiment. A LINAC is a machine that provides a source of electrons and accelerates them to velocities just below the speed of light. The acceleration occurs via the coupling of a high-power RF field, generated by a Klystron, with the electrons within a specifically designated waveguide [37]. The electrons focus into a beam through multiple stages of focusing lenses as the electrons accelerate through the vacuum. A LINAC on its own is not a neutron source, but can be used to produce neutrons if the accelerated electrons are collided with a thick, high-Z number target to produce high-energy photons, referred to from this point forward as gamma rays [38]. These gamma rays interact with the nuclei of the high-Z material through the photonuclear effect to produce fast neutrons. The following sections will explore the physics of the photonuclear effect and the design of a LINAC-based photoneutron converter.

3.2   Bremsstrahlung and the Photonuclear Effect

The ability to generate a high-flux fast-neutron source from a LINAC comes from two nuclear physics concepts: bremsstrahlung and the photonuclear effect. Each of these interactions must occur in sequence in order to transfer energy from the electron beam of the LINAC into a large flux of neutrons.

3.2.1 Bremsstrahlung

Bremsstrahlung means "braking rays" in German, which provides an accurate description of the underlying physics [1]. Bremsstrahlung is the release of gammas as high-energy electrons are decelerated by passing through the vicinity of a nucleus. Electrons can decelerate by colliding with an atom directly or by being slowed through the electromagnetic field between atoms. Gammas are emitted as the electrons decelerate with the gamma intensity depending upon the Z-number of the collision material [1]. Maximizing the bremsstrahlung intensity requires a material with large numbers of protons (high-Z) in order to efficiently transfer the energy from the electron into gammas. For thin targets, the bremsstrahlung-intensity spectrum can be found using the Bethe-Heitler cross section; however, as the target thickness increases the accuracy of this model diminishes [39]. The invalidity of the Bethe-Heitler cross section occurs in thicker targets since electrons emit multiple gammas as they continue to travel through the material. The Bethe-Heitler cross section only applies for electrons which interact once with the target material. A Monte-Carlo radiation-transport program needs to be used in order to accurately calculate the bremsstrahlung-intensity distribution. Monte-Carlo programs use statistical analysis to calculate the probability of interaction based on the cross sections for various particles and track the collisions and generation of nuclear particles, and will be discussed in section 3.3 [38]. The Monte Carlo N-Particle program (MCNP), an example of such a radiation-transport program, was used to simulate an example bremsstrahlung-intensity spectrum using a 31-MeV electron beam hitting a 1 cm thick tungsten block, shown in Figure 3.3.
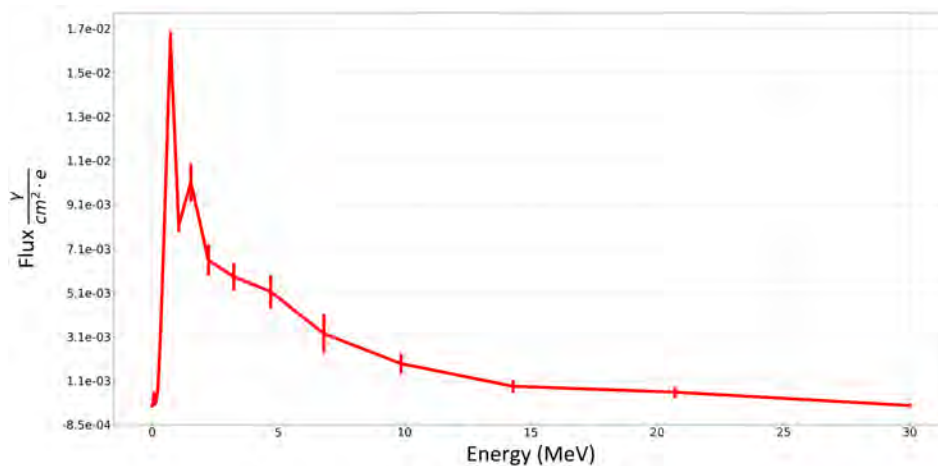
Figure 3.3. Gamma-Intensity Spectrum through a 1 cm Thick Tungsten Block

In Figure 3.3, it is important to note that the maximum number of gammas is around 1 to 2 MeV while there is an elongated tail at higher energies. This energy spectrum of photons is produced by the deceleration of electrons through the electromagnetic fields within the atomic structure of the collision material. The energy spectrum of photons is important to understand when analyzing the efficiency of the photoneutron converter because bremsstrahlung is the first particle interaction that occurs in order to generate neutrons from an electron source.

3.2.2   Photonuclear Effect

In Section 3.1, we discussed the process of fission by reactors which is initiated by the absorption of a thermal neutron by a U-235 or Pu-239 nucleus. The neutron puts the nucleus into an unstable state that causes the nucleus to break apart and release neutrons on a fission spectrum [22]. The photonuclear effect ejects neutrons from a nucleus through the absorption of a high-energy photon, while fission is induced by the capture of thermal neutrons within the reactor [35]. The interaction of a gamma with a nucleus is far different than the interaction of a neutron with a nucleus. The gamma ray must have a higher energy than the neutron-binding energy in order to cause a photonuclear event; this energy is usually around 7 MeV, depending on the Z-number [1]. The equilibrium of the strong force within the nucleus is interrupted when a gamma is absorbed by a nucleus creating a collective excitation between the nucleons [40]. The photonuclear cross section of tungsten is shown as an example in Figure 3.4.
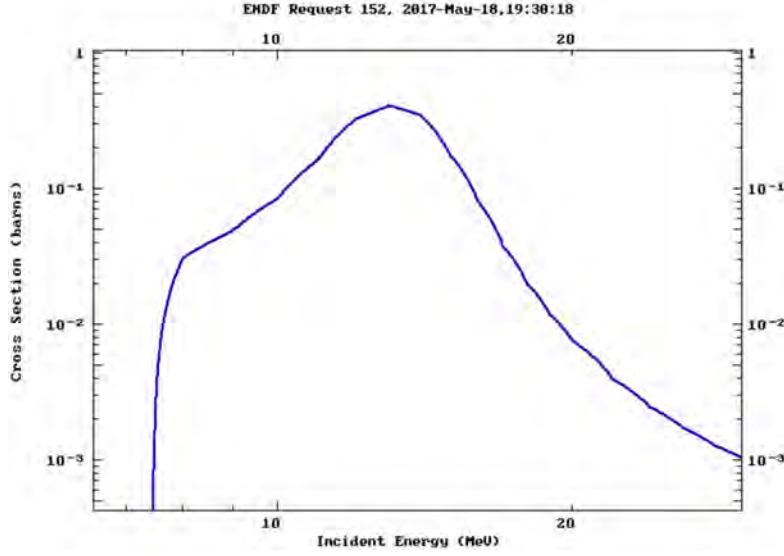
Figure 3.4. Photonuclear Cross Section for Tungsten given Incoming Photon Energy. Source: [23].

The giant dipole resonance (GDR) that occurs between 5 MeV and 15 MeV from the photonuclear effect within high-Z materials promotes a large increase in the probability of gamma interactions with the nucleus if the incoming-gamma energy is between 5 MeV and 15 MeV. This GDR occurs when a gamma of a particular energy achieves a resonance with the nucleus of an atom, which can be visualized as a set of nucleons connected by springs [40]. If a spherical nucleus is assumed, a Lorentzian distribution can be used to describe the cross section of photoabsorption σ_{abs} by the nucleus in the GDR as [40]

$$\sigma_{abs}(E_\gamma) = \frac{\sigma_R E_\gamma^2 \Gamma_{GDR}^2}{(E_\gamma^2 - E_{GDR}^2)^2 + E_\gamma^2 \Gamma_{GDR}^2}. \tag{3.1}$$

In equation (3.1), E_γ is the gamma energy, E_{GDR} is the energy of the GDR, Γ_{GDR} is the width of the GDR, and σ_R is the maximum cross section of the distribution. This model does not work for non-spherical nuclei because a non-spherical nucleus will have multiple GDRs at close, but different energies. The GDR energy E_{GDR} can be described by modelling the nucleons as a set of masses attached by springs at a given stiffness. The GDR energy is then found to be related to the resonance frequency ω of the mass-spring system as [40]

39

$$E_{GDR} = \hbar\omega = KA^{(-1/3)}, \tag{3.2}$$

where A is the atomic mass, $\hbar$ is the reduced Planck's constant, and K is the spring constant associated with the system. It is essential that the GDR of the target material is at relatively low energy in order to achieve higher cross sections and flux of secondary neutrons, optimizing the photonuclear effect. The nucleus could maintain enough stability to maintain its atomic structure if the gamma energy is not high enough. The nucleus would only release a gamma of different energy in order to de-energize its nucleus [22].

Neutrons emitted via the photonuclear effect are emitted around the mean energy of the nucleus, which is generally high after gamma absorption. Thus, photoneutrons are generally high energy, and the photoneutron spectrum has a high fast-to-thermal ratio. The energy spectrum of the ejected neutrons will be similar to the Watt spectrum of neutrons produced via fission if the photonuclear effect is utilized [35]. The neutron spectrum of tungsten via a 31-MeV electron beam is shown in Figure 3.5 as an example of a neutron spectrum emitted through the photonuclear effect.
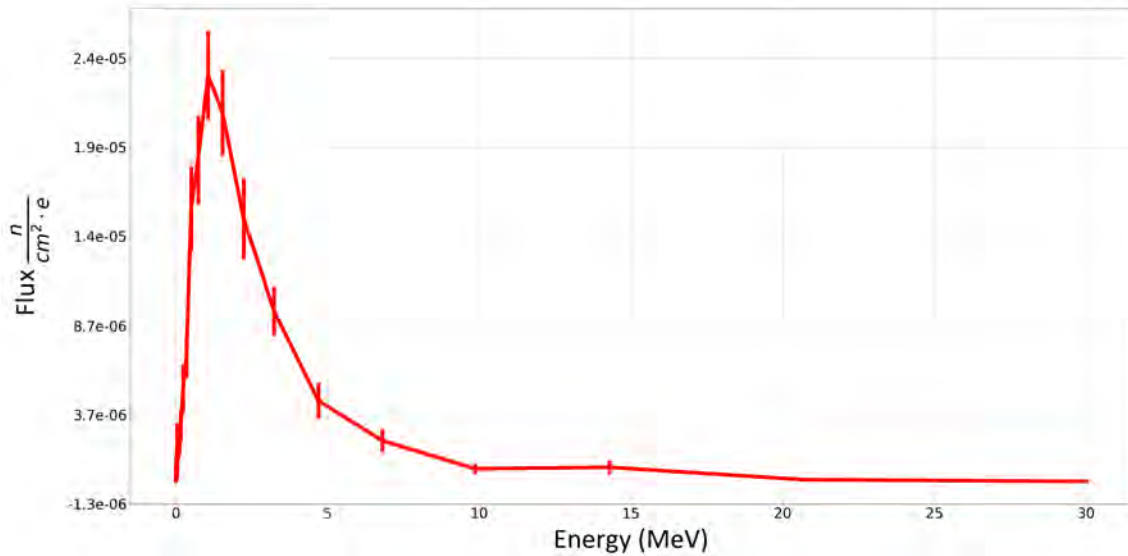
Figure 3.5. Neutron Spectrum of the Photonuclear Reactions within Tungsten

3.3 Photoneutron Converters using LINACs

LINACs provide a high-energy electron beam that can be utilized to produce fast neutrons via the photonuclear effect, as explained in Section 3.2. A photoneutron converter target can be designed to generate neutrons using the bremsstrahlung and photonuclear effect previously discussed in order to create a high-flux fast-neutron source using a LINAC [4]. An illustration of the reaction sequence that photoneutron converters use to convert high-energy electrons into fast neutrons is demonstrated in Figure 3.6. An appropriate photoneutron source will utilize a target material of a geometry such that the fast-neutron flux is maximized, while the gamma flux is minimized.
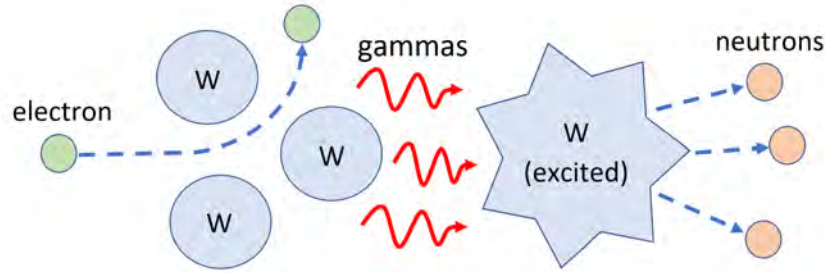
Figure 3.6. Illustration of the Bremsstrahlung and Photonuclear Reactions inside Photoneutron Converters

3.3.1 Stopping Power

The key behind using a photoneutron converter as a neutron source is optimizing the materials, geometry and shielding in order to maximize neutron production and minimize the production of other unwanted particles. Stopping power needs to be understood in order to optimize the bremsstrahlung and photonuclear reactions within the photoneutron converter. Stopping power is the rate of energy loss over a distance within a specific material [1]. The total stopping power of electrons $-\frac{dE}{dx}$ at the high energies used in LINAC operation consists of radiative loss and collision-energy loss given as [22]

$$- \frac{dE}{dx} = - \left(\frac{dE}{dx} \right)_{coll} - \left(\frac{dE}{dx} \right)_{rad}.$$ (3.3)

The collision-energy loss comes from the Bethe-Bloch formula taking into account the

relativistic effects of the high-energy electrons. The energy loss due to collisions is given as [4]

$$-\left(\frac{DE}{dx}\right)_{coll} = \frac{4\pi z^2 q^4}{mv^2} nZ \left[ln\left(\frac{2mv^2}{I}\right) - ln\left(1 - \frac{v^2}{c^2}\right) - \frac{v^2}{c^2} \right], \tag{3.4}$$

where I is the average-excitation energy, Z is the atomic number of the target material, c is the speed of light, and v is the electron velocity. The energy loss due to the emitting of bremsstrahlung radiation is given as [4]

$$-\left(\frac{dE}{dx}\right)_{rad} = KnZ^2E, \tag{3.5}$$

where K is a constant, E is the kinetic energy of the electron, n is the number of atoms per unit volume, and z is the charge number of the particle. It can be seen in equation (3.5) that the radiative electron-stopping power is highly dependent on Z showing that materials with higher-atomic number will be more efficient at generating bremsstrahlung than materials with low-atomic numbers. As an example, a plot of the electron-stopping power through tungsten is provided in Figure 3.7.
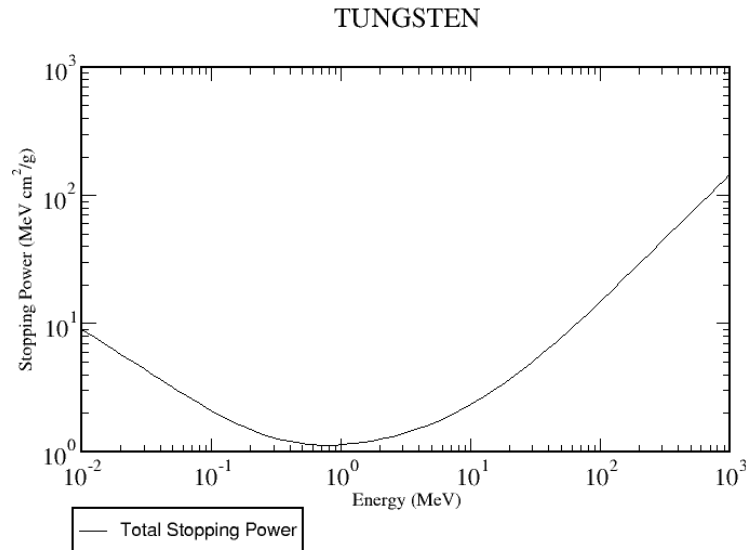
Figure 3.7. Plot of Stopping Power versus Incoming-Electron Energy through Tungsten. Source: [41].

42

3.3.2 Mass-Attenuation Coefficient

The generated gammas from the incident electron beam do not follow the same principles as the electrons; therefore, the stopping power equations used for the electrons cannot be used for the gammas. The mass-attenuation coefficient μ/ρ is the area of interaction per mass of a photon within a specific material. The range of the photon through the material is determined by dividing by the density of the collision material. The mass-attenuation coefficient varies given the incoming-gamma frequency. The distribution of the mass-attenuation coefficient versus the incoming-gamma energy is given in Figure 3.8.
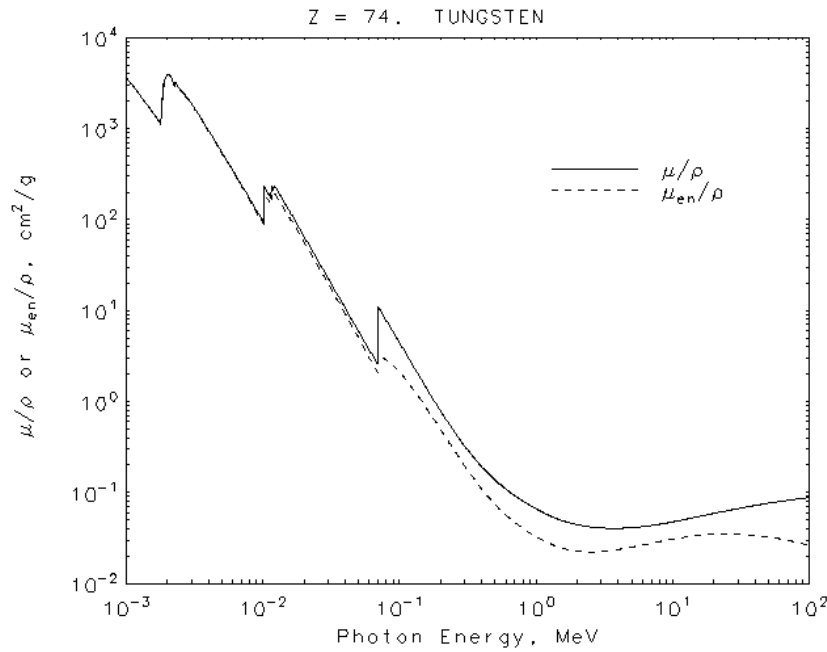
Figure 3.8. Distribution of the Mass-Attenuation Coefficient Versus Energy through Tungsten. Source: [42].

The intensity of a monoenergetic gamma beam $I(x)$ through a certain distance x of a material given a monoenergetic gamma beam of energy I_o is shown as [42]

$$I(x) = I_o e^{-(\mu/\rho)x}. \tag{3.6}$$

This equation needs to be integrated over the energies of the beam if the incident gamma beam is not monoenergetic. The total photon intensity I given the integration of the

incident-photon frequencies is shown as

$$I = \int_0^{\omega_{max}} I_o(\omega) e^{-\frac{\mu}{\rho}(\omega)x} d\omega. \tag{3.7}$$

The amount of material needed to stop the bremsstrahlung within the photoneutron converter can be calculated using the mass-attenuation coefficients. This thickness is optimized in order to maximize the utilization of the gamma beam in the photonuclear reactions.

3.3.3 Photoneutron Operation and Example

Stopping power and the mass-attenuation coefficients are important to understand to make an efficient-neutron source. The photon and electron distributions need to be contained as much as possible within the generating material in order to generate a maximum number of neutrons [38]. A high-Z material must be used to maximize the photoneutron production [21]. The large Z number increases the rate at which electron energy is converted to bremsstrahlung. The high-Z number provides a higher photonuclear-interaction probability due to the material's smaller GDR energy. The elements most commonly used for photoneutron production are uranium, lead, and tungsten since they are heavy elements with high stopping power [35]. High-Z materials allow for high-density neutron generation by absorbing the energy from the electron beam within a short distance [38].

An illustration of the electron beam of the LINAC entering the converter from the right and the bremsstrahlung and neutron-generation regions occurring within the converter are shown in Figure 3.9 to further illustrate the dual process of photon and neutron generation within the photoneutron converter. The condensed-electron beam is dispersed within the material due to the electrons being decelerated and the electromagnetic field of the atoms altering the trajectories. The bremsstrahlung makes a "tear drop" shape that becomes more elongated in the direction of the electron beam as the electron-beam energy increases [22]. The cross section for generation of neutrons from photonuclear reactions is isotropic; however, it is important to note that the full region of the neutron generation is not isotropic since the region of photons is not a point source [36]. The neutron region will be elliptical rather than spherical because from a higher-energy LINACs the photon-generation region is more elongated in the direction of the beam.
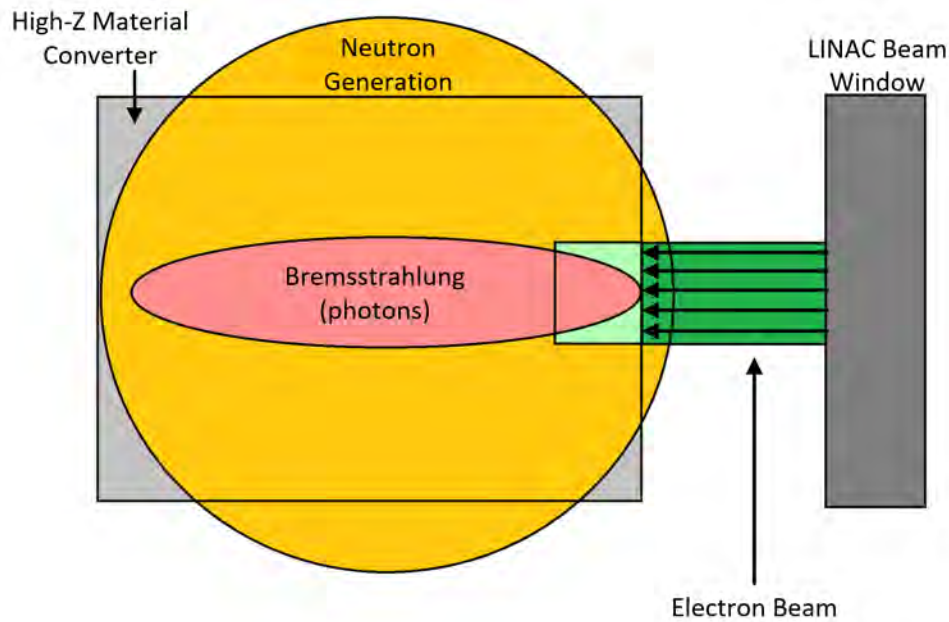
Figure 3.9. Illustration of Photoneutron Converter Operation

The process of using a LINAC and a photoneutron converter is commonly chosen to generate high-neutron yields for medical-isotope production [38]. Gohar from the Argonne National Laboratory developed a cylindrical converter concept that utilizes tungsten pieces of increasing thicknesses encased in an aluminum cylinder as an example of a photoneutron converter developed for medical-isotope production. Gohar designed his photoneutron converter around a 100-MeV LINAC. The exploded view of his 100-kW photoneutron-converter concept is demonstrated in Figure 3.10.

The purpose of the outside cylinder is to provide a casing for the cooling system. Water is pumped through the cylinder in order to keep the tungsten pieces cool during the neutron-generation process. The tungsten within the aluminum casing is the high-Z converting material that converts the incoming electrons into photons which in turn generate neutrons from the tungsten. There are two main reasons for using tungsten pieces with different thicknesses. The first is to make a consistent flux of neutrons, and the second is to absorb the entire energy spectrum of the bremsstrahlung emitted. The tungsten target elements closest to the incoming beam are thinner because the electron energy will be highest upon entry into the converter; therefore, more energy will be absorbed in a shorter distance. As you get further from the beam entry the energy of the electrons decrease. The thicknesses

45
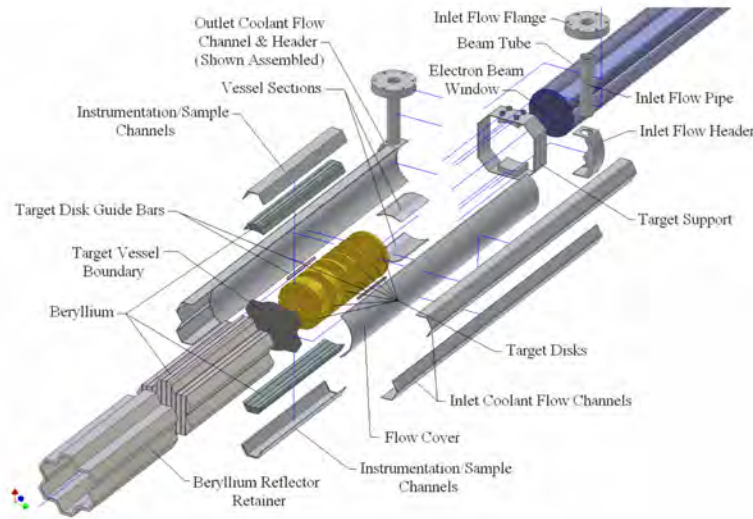
Figure 3.10. Cylindrical Photoneutron Converter Concept for Medical Isotope Production. Source: [38].

need to increase in order to absorb the same amount of energy from the beam at each tungsten piece [38]. Absorbing the same amount of the beam energy between each tungsten piece optimizes the energy transfer from electrons to photons and from photons to neutrons. The tungsten also needs to be thick enough to absorb the full spectrum of bremsstrahlung emitted from the electron collisions and decelerations. Absorbing the entire generation of bremsstrahlung is essential in order to minimize photon radiation outside of the converter.

At the same time, since the efficiency of bremsstrahlung generation is so low, most of the energy of the electron beam will be transferred into heat. While tungsten has a melting point of 3,422°C, the other parts of the converter need to be maintained at lower temperatures. Minimizing the excess heating is the purpose of the cooling system. The excess heat is pulled away from the converter through the separations between the tungsten because they allow water to flow over them.

3.4   Design of Photoneutron Converter

The material, shape, and size of the converter were optimized via simulation of the radiation transport using MCNP in order to design a photoneutron converter that would produce a large enough neutron yield for the desired experiment. MCNP is a Monte-Carlo radiation-

transport simulation program that uses statistics and elemental-nuclear parameters to set weights and probabilities to nuclear events. The program tracks particles through their lifetime in a target area, essentially simulating the total path of each particle. MCNP was used to run various simulations of an electron beam striking a high atomic-weight material in order to generate bremsstrahlung and consequently neutrons from the material. The statistical certainty of the outcome increases with the number of input particles used in the program. The variance of the outcomes in MCNP decreases as $1/\sqrt{N}$ where N is the number of input particles used in the simulation. Each input particle can generate millions of secondary particles through reactions during the lifetime of the particle, each of which is tracked by MCNP; therefore, the computational power needed to solve the simulation massively increases with input-particle number. MCNP becomes an extremely computationally intensive program when low variance is required. The simulation time required for some complicated simulations could take days, if not weeks, to complete. Massively-paralleled super-computing techniques were used in order to reduce the simulation time. The Hamming supercomputer at NPS was used to run multiple simulations in parallel using 64 processors for each simulation. The supercomputer was able to cut down the simulation times drastically where a week long simulation could be done in a few hours. The combination of Hamming and MCNP provided a robust simulation platform for exploring the design optimization of the neutron flux of a photoneutron converter.

3.4.1   MCNP Optimization of Neutron Flux through Geometries

MCNP uses what are known as input decks to set up the simulation geometry, materials, particle importance, physics models, desired measurements, and input-particle number of a simulation. The frame of the geometries is built by defining planes in 3D space. These surfaces denote the boundaries of the cells, specified by a density and material. The geometry is built around the (0,0,0) origin of the MCNP 3D space, and the desired tracking of specific particle types within the geometry can be expressed. The tracking of electrons, photons, and neutrons was essential in the simulation of a photoneutron converter. The location, energy, size, and directionality of a radiation source is entered into the program along with the number of particles desired to be simulated once the geometry of the simulation and the importance for each particle are specified. It was essential to use the parameters of the electron beam generated by the 44-MeV LINAC beamline from IAC in order to produce accurate simulations. A 31-MeV electron source was used with an

electron-beam diameter of 1 cm for the MCNP simulations in this thesis. Appendix B is an example of an MCNP input file using the designed photoneutron converter and a 31-MeV electron beam.

The first simulation that needed to be carried out for designing the optimal photoneutron converter compared the neutron production efficiencies of tungsten and lead. Both materials have high-Z number and could be used as efficient photoneutron targets. The geometry used to run this comparison was a simple 2.5 x 2.5 cm rectangular block with a varying length along the beam direction. The electron source was placed 2 cm away from the face of the block. The length needed to be varied while conducting this comparison because the stopping power and mass-attenuation coefficients between these materials are different; therefore, the length at which the maximum-neutron flux occurs could vary between the materials. A large cube of air was built around the target in MCNP because some particles may exit the converter and then reflect back in. To minimize the variance in the calculation, 10^6 input particles were simulated to find the average flux across the outgoing side of the converter. A comparison between the neutron fluxes of lead and tungsten at varying lengths of material is shown in Figure 3.11.
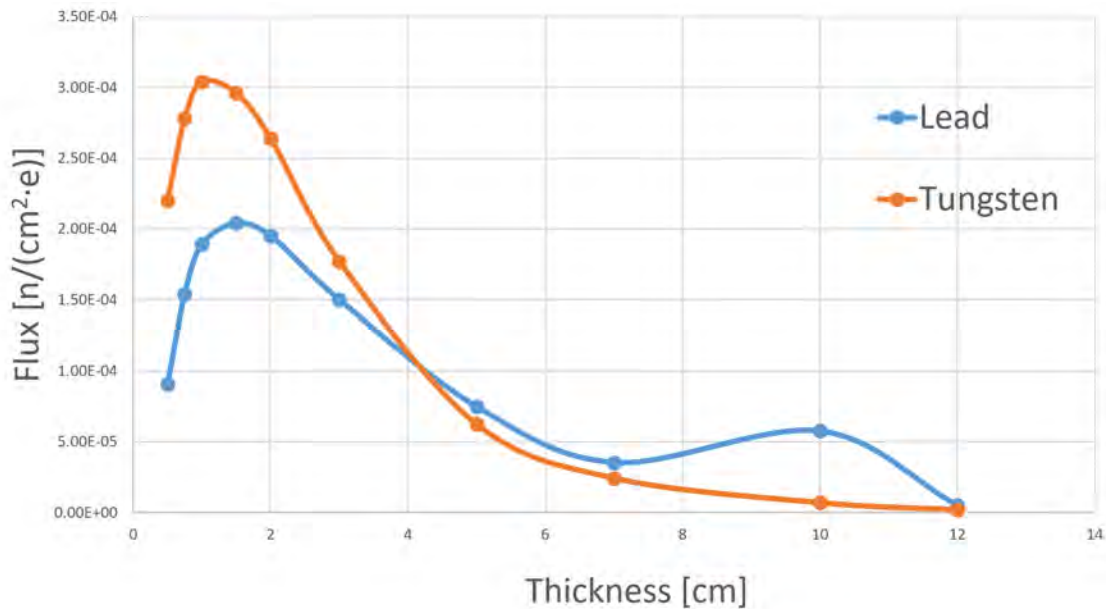

Figure 3.11. MCNP Simulation of Neutron Flux vs Length through Tungsten and Lead

While both are efficient neutron producers, tungsten has a 50 percent higher neutron flux at the optimal length. This flux difference occurs because the GDR energy of the tungsten is lower than that of the lead, increasing the interaction probability. One additional material which could be used as a photoneutron producer but was not investigated here is uranium. Uranium has been shown to outperform tungsten and lead as a photoneutron producer by about 50 percent due to photofission [43], but the cost, availability, and safety issues of uranium make it unattractive for use in this thesis work.

The next design step was to determine the change in neutron yield based on the width of the material. The neutron-generation region should be fairly isotropic; however, the bremsstrahlung-generation region within the tungsten is lengthened in the direction of the beam since the beam of electrons is biased in one direction. It was determined that placing the device measurement platform on the sides of the converter off axis from the electron beamline would allow for a higher-neutron flux and a low-gamma flux since the flux of gammas needs to be minimized while maintaining the neutron flux. An MCNP simulation that used a 31-MeV electron beam on a tungsten block with a varying width to find the optimal neutron flux on the side of the tungsten converter was conducted. The length and height of the block was set at 2.5 cm, and the width was varied from 1.5 cm to 2.3 cm. The maximum-neutron flux off the side of the tungsten converter with varying width is shown in Figure 3.12.
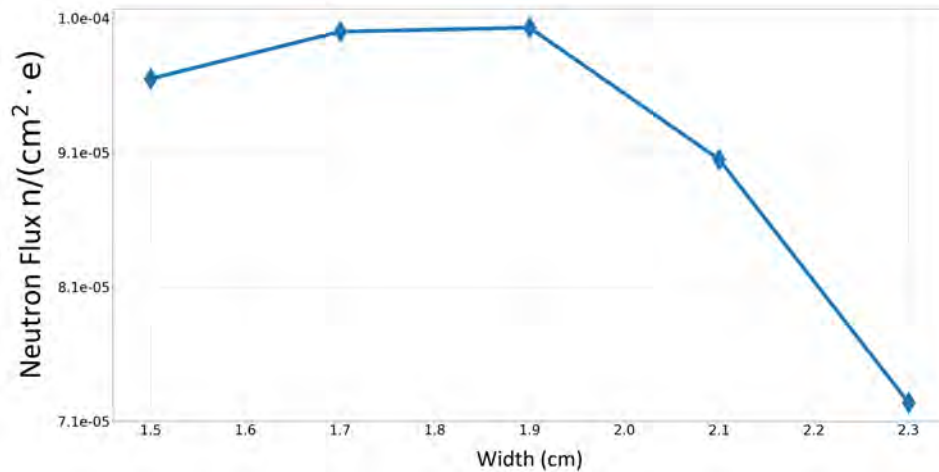

Figure 3.12. MCNP Simulation of Neutron Flux vs Width of Tungsten

Results showed the neutron yield increases as the tungsten width increases until the point

where the photon-generation region falls off within the material. The neutron yield decreases rapidly as the width is increased past the generation region. A 2-cm tungsten-target width was determined to be optimal. In addition, the gamma flux on the back and the side of the target were examined. A comparison of the gamma flux on the back and side of the target is shown in Figure 3.13. This MCNP simulation was done on a 2.5 x 2.5 x 2.5 cm tungsten cube with the left plot taken on the back face and the right plot taken on the side of the converter.
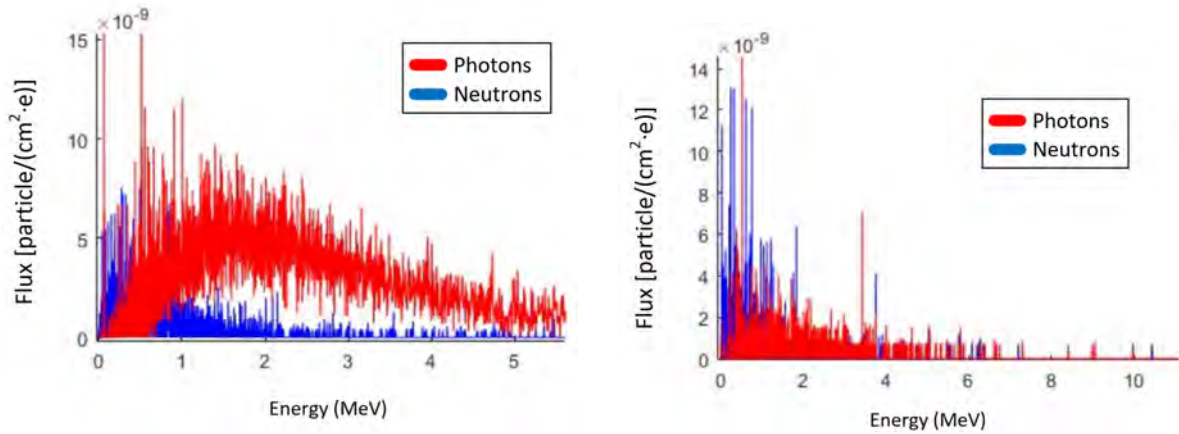
Figure 3.13. Flux Spectrum of Photons and Neutrons In-Line with the Beam (left) and Off to the Side of the Beamline (right)

The distributions of Figure 3.13 demonstrate that the gamma flux is indeed elongated in the direction on the electron beam. Using the sides of the converter minimizes the gamma flux at the point of neutron irradiation. The neutron flux on the sides of the converter is comparable to the flux in the direction of the beamline since the neutron-generation region is generally isotropic. A rectangular target design provides two regions where the devices can be irradiated, the left and the right side.

3.4.2   Split Converter Design for Cooling

Another cooling feature was the splitting of the tungsten into three pieces in the direction of the beamline with the top and bottom sides of the converter left free for running water through to cool the converter. By splitting the tungsten, water is allowed to flow in between the three tungsten parts pulling away the heat produced from the electron beam's inefficiency of bremsstrahlung generation. The tungsten was cut perpendicular to the beamline instead

50

of parallel to the beamline in order to keep from having a plane of water moderate the neutrons on the side of the converter. The entire electron beam needed to be absorbed within the first block so the energy is not lost within the water. Equation (3.2) was modified to calculate the distance required to fully stop the electron beam. The modified equation from (3.2) is expressed as

$$\Delta x = \int_{E_o - \Delta E}^{E_o} \frac{1}{\left(\frac{dE}{dx}\right)} dE, \tag{3.8}$$

where Δx is the distance through the target, E_o is the initial energy, and ΔE is the change in energy through Δx of material. Using the 31 MeV designation by IAC as the electron-beam energy, the first tungsten block needed to absorb the complete-energy spectrum to maximize the bremsstrahlung generation from the tungsten target. A demonstration of the use of equation (3.6) on the stopping-power distribution and the calculation of the tungsten thickness is shown in Figure 3.14.
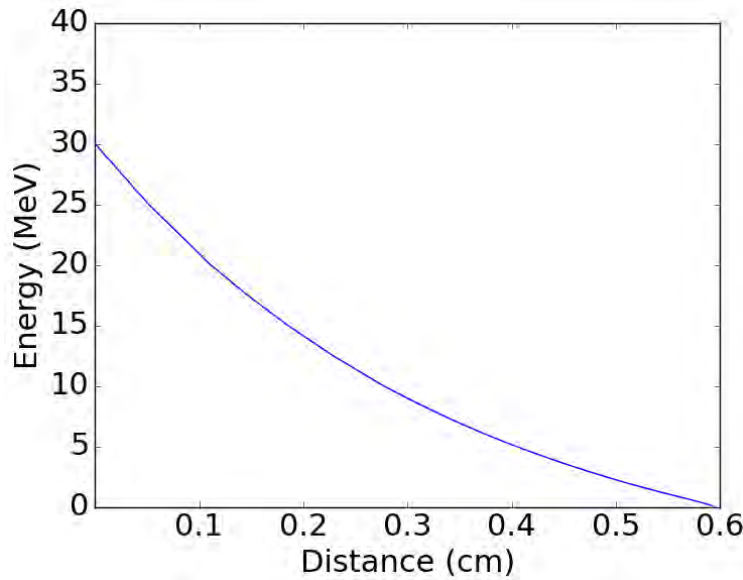

Figure 3.14. Stopping-Power Distribution Showing the Length of Tungsten Needed to Absorb the Entire Electron Beam

The thickness needed to be at least 0.6 cm in order to fully absorb the electron beam within the first block; therefore, the first block was designed to be 0.7 cm in order to ensure the

electron-beam absorption. The second two blocks were separated in order to promote the flow of water through the converter for cooling purposes, while being thick enough to utilize the entirety of the bremsstrahlung generated in the first block. The width of the tungsten target was determined to be optimal at 2 cm, while the thicknesses of the three tungsten blocks were determined to be 0.7 cm, 0.9 cm, and 3 cm in order to absorb the entire electron beam and bremsstrahlung.

3.4.3 Tungsten Photoneutron Target

A SolidWorks model was built to adhere to the optimized parameters and provide a design for fabrication. The fabricated tungsten target is shown in Figure 3.15.
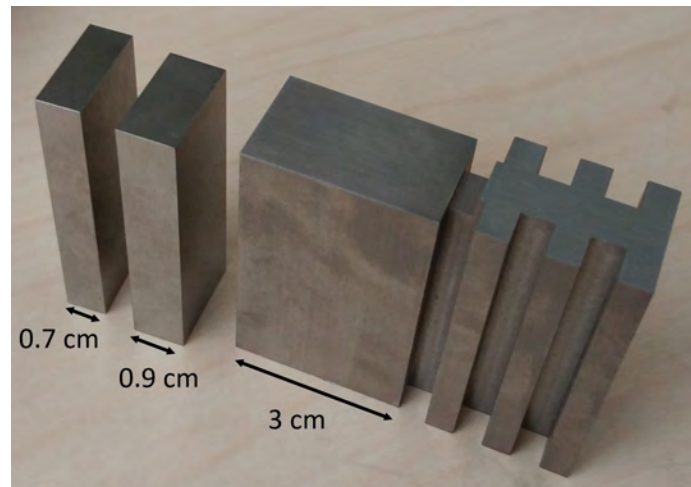
Figure 3.15. Fabricated Tungsten Photoneutron Converter

The third tungsten part included a finned portion in order to increase the surface area for the cooling apparatus to run water over and cool more efficiently. The fabrication of the tungsten converter design was done by Midwest Tungsten Service Inc. The two smaller blocks were cut and sized from a larger block, while the third more complicated part was fabricated by making a mold of the part and sintering the tungsten in that mold. All three components were made with greater than 99.95 percent pure tungsten.

3.4.4 Design and Fabrication of Target Cooling System

The goal for the cooling system was to cool the tungsten target using an active-convective system in order to minimize heating of the irradiated components, which needed to be

as close as possible to the tungsten to maximize the neutron flux received during the experiment. An active convective-cooling system using flowing water in direct contact with the tungsten would allow the most heat to be carried away from the tungsten. The cooling system needed to enclose the entirety of the tungsten converter in a casing with a water tight seal. This casing was designed to be aluminum as the activation products of aluminum have short half-lives and decay away quickly. Using aluminum minimizes any unnecessary activation from the cooling system.

Based on the design of the tungsten converter, numerous design parameters needed to be met for the aluminum in order to optimize cooling and minimize neutron-flux reduction/moderation. The aluminum needed to be thin on the sides of the converter to keep from shielding the neutron flux. The neutron flux would still be lowered if the aluminum was too thick on the sides even though aluminum has a low cross section for neutrons. Another desired design parameter was the ability to hold a circuit board with the components to be irradiated held over the optimized neutron flux. Holding the boards on the sides of the converter would allow for consistent results and utilization of the maximum-neutron point along the side of the converter. Lastly, the cooling assembly needed to have spacers that kept the tungsten parts separated at fixed distances to allow for water to flow from the inlets to the outlets in between the tungsten. The cooling was essential because the tungsten acts as the heat source as the electron beam deposits a small portion of its energy into bremsstrahlung and the rest into heat. The final SolidWorks model of the photoneutron converter is provided in Figure 3.16. The fabrication of the aluminum casing is provided in the right image of Figure 3.16. A more detailed view of the converter design can be found in Appendix C.

Figure 3.16. Full SolidWorks Converter Design (left) and Fabrication of Aluminum Casing (right)

The aluminum parts were fabricated using Aluminum 6061 alloy through CNC milling by ProtoLabs Inc. The aluminum casing had to be split into three separate parts in order to allow the tungsten target components to be placed inside, as shown in the open converter in Figure 3.17. The final converter was built by placing the tungsten parts into the aluminum casing and welding the interfaces of the aluminum to create a water tight seal around the tungsten. This design ensured that the tungsten did not need to be welded and was only held in place by the aluminum. Note that not needing to weld tungsten was an important consideration for the design because the high melting point of tungsten makes it difficult to weld tungsten. Aluminum is much easier to weld because its melting point is far lower.

3.4.5 Full Photoneutron Converter Simulation

With the full converter design complying to the optimizing parameters discovered from the initial MCNP simulations discussed in Section 3.4.1, the SolidWorks model of the full photoneutron converter and cooling system was imported into the MCNP interactive program called VISED. MCNP models are developed by detailing various planes, cylinders, and spheres within a space in order to build a 3D object. Building complex geometries within the original MCNP program is tedious and difficult; however, VISED allows for SAT files to be imported from SolidWorks and built into the necessary planes for the geometry. The model geometry used inside VISED to create the MCNP input file is illustrated in Figure 3.18. The blue represents the simulated air, the yellow represents tungsten, the green

54

Figure 3.17. Open Converter Showing the Tungsten Component Locations inside the Aluminum Casing

represents aluminum, and the red denotes water.

The split-design of the photoneutron converter can be imported into MCNP using VISED. The full simulation of the converter is necessary as the flux distribution is heavily dependent upon the geometry of the photoneutron converter. Taking neutron and photon flux tallies in MCNP along the side of the converter along the circuit board slot location from the incident face to the back of the converter allows the point of peak neutron and photon flux to be found. The neutron and photon fluxes at increasing distances from the electron-beam incident face are shown in Figure 3.19.
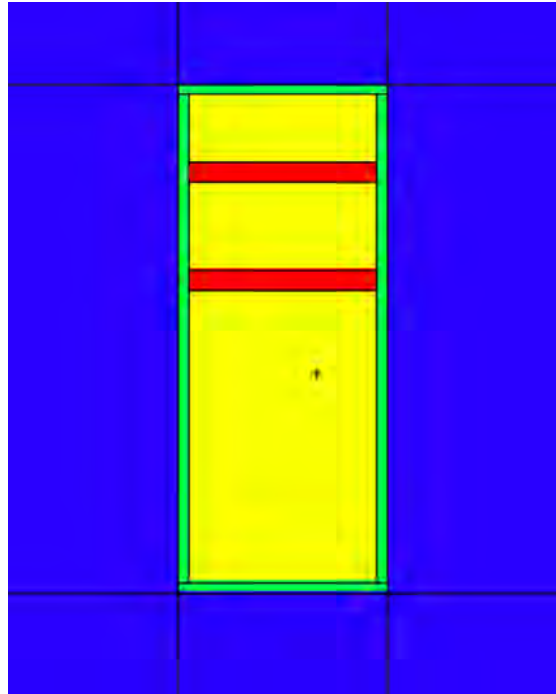
Figure 3.18. VISED Model of Simplified Photoneutron Converter without Cooling System
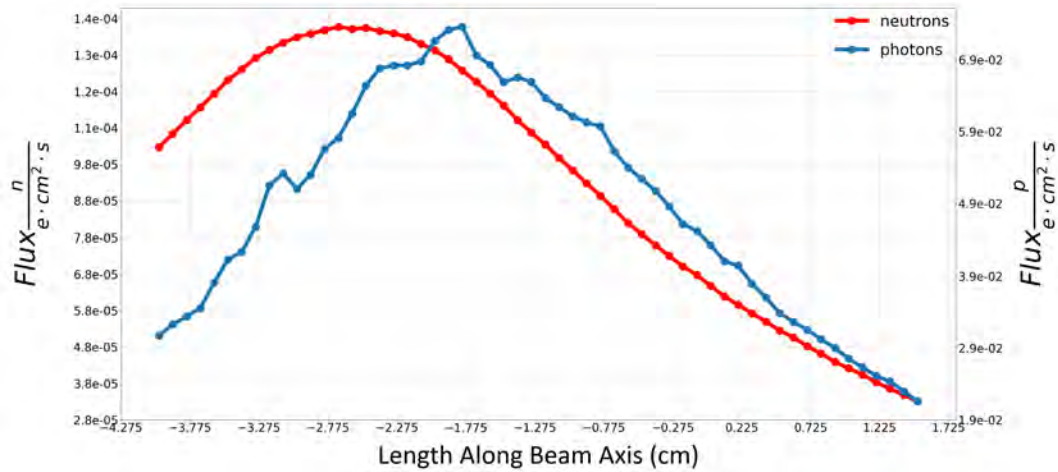
Figure 3.19. MCNP Simulation of Neutron and Photon Fluxes Along the Side of the Converter

It was predicted through MCNP that the maximum-neutron generation would occur within 1.75 cm of the beam-incident face because the electronic stopping power of tungsten is so high. The photon flux is shown along the side of the converter in Figure 3.19, and

56

shows that the peak of the photon flux occurs 0.75 cm behind the peak of the neutron flux. The difference in location of the maximum-flux points demonstrates that the photon flux is elongated and biased in the direction of the electron beam, while neutrons are generally generated isotropically.

A neutron-flux image was also generated in order to measure the complete neutron distribution off the side of the converter where the device-under-test (DUT) would be. The simulated flux image as a contour map with dark red being the highest flux and dark blue being the lowest flux is shown in Figure 3.20. In Figure 3.20, the electron beam would be entering the converter from the left of the image since the image is a side view of the neutron field off the converter.

Figure 3.20. MCNP Neutron-Flux Image Off the Side of the Converter

The isotropic generation of neutrons can easily be seen from the spherical flux image which verifies that the neutrons are not biased in the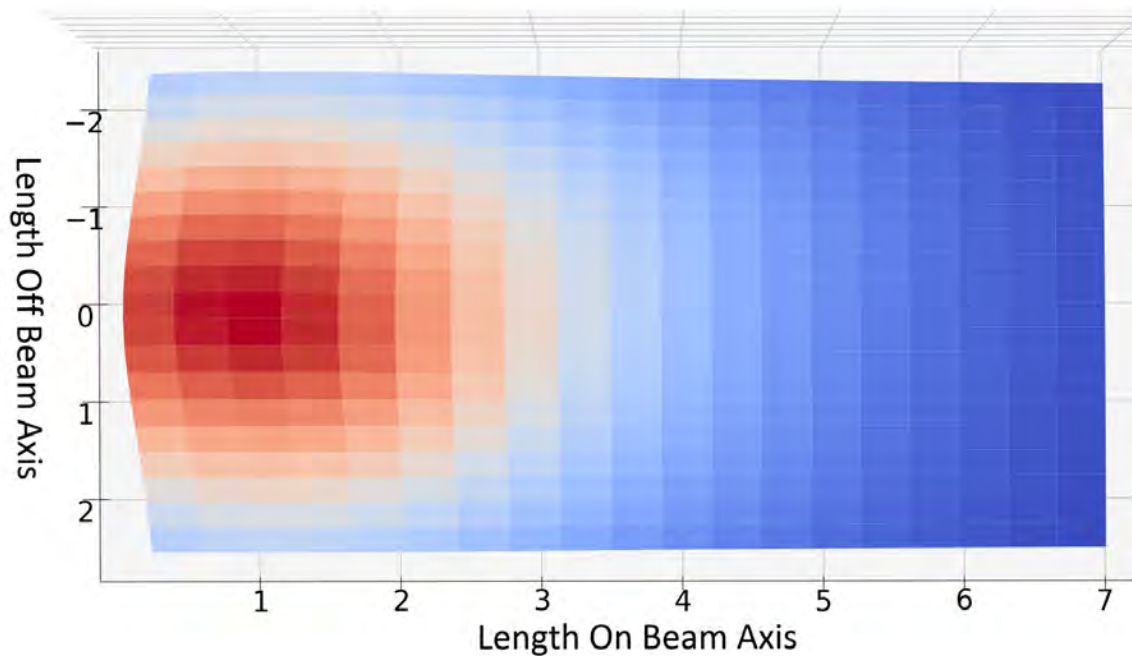 direction of the electron beam and using the sides of the converter is valid. The location of the maximum-neutron flux is shown to be a little over 1 cm from the incident face. This result varies slightly from the simulations done previously that placed the maximum point at 1.75 cm, which means the device being tested needed to be placed about 0.5 cm closer to the incident face than previously thought. The maximum-neutron flux taken from this flux image was $2.2 \cdot 10^{-4}$ n/(cm^s · e). The units of flux output by simulation are neutron per source electron which is independent of the machine parameters used to produce the source. The output flux of the converter by irradiation from a given LINAC is calculated as

$$\Phi = \frac{\lambda f I_m \phi}{q}, \tag{3.9}$$

where ϕ is the flux per electron, I_m is the max current of the LINAC, f is the pulse repetition frequency, and λ is the pulse width. The max current for the IAC 44-MeV LINAC was 200 mA, while the pulse repetition frequency was 180 Hz. The pulse width was 2.5 μs, and the energy used was 31 MeV in order to achieve a 2 kW power rating. With the conversion to the flux that would be achieved with the 44-MeV LINAC at the IAC, the neutron flux would be $1.2 \cdot 10^{11}$ n/(cm^2 · s). Over the course of a 25-hour radiation experiment, the total fluence is calculated to be $1.08 \cdot 10^{16}$ n/cm^2.

The converter design was also input into ANSYS in order to get an accurate temperature prediction of the converter cooling performance. ANSYS is a physics simulation software that include fluid dynamics and heat transfer simulations. An IGES file from SolidWorks can be imported into ANSYS in order to build the desired simulation structure. The boundaries and cells are initialized on the structure and physics models and equations are set for the desired cells. Heating and fluid flow simulations were performed for the metals of the target. In addition, cooling by natural convection was modeled by placing the target model in a large cube of air. A heat source specified using a cylinder with the same radius and power as the electron beam was placed inside the tungsten representing the heating from the electron beam within the converter. The heat source was a diameter of 1 cm and the power emitted from the source was 1.5 kW, matching the parameters of the 44-MeV LINAC beamline at IAC. The water through the converter was simulated running from the

inlets to the outlets at a rate of seven gallons per minute, which was the pump rating at IAC. The cooling system was designed in order to achieve turbulent flow in between the tungsten blocks to increase heat transfer.

The cross-sectional view through the center of the converter illustrating the water-velocity magnitude given a seven gallon per minute input velocity is given in Figure 3.21. Turbulent flow can be clearly seen in the channel between the tungsten pieces.
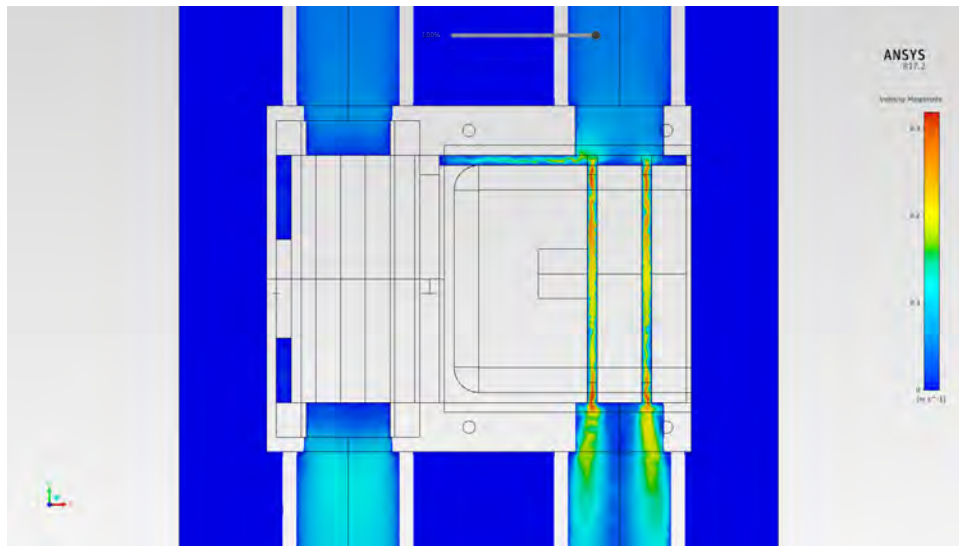
Figure 3.21. ANSYS Simulation of Flow-Velocity Magnitude through the Photoneutron Converter

Heating behavior within the tungsten blocks was simulated with the inlet temperature of the water set at 30°C, as shown in Figure 3.22. A maximum temperature of 152°C was simulated in the front tungsten block. Note that this is a pessimistic estimate of heating within the converter as it is assumed all of the electron energy is converted into heat.
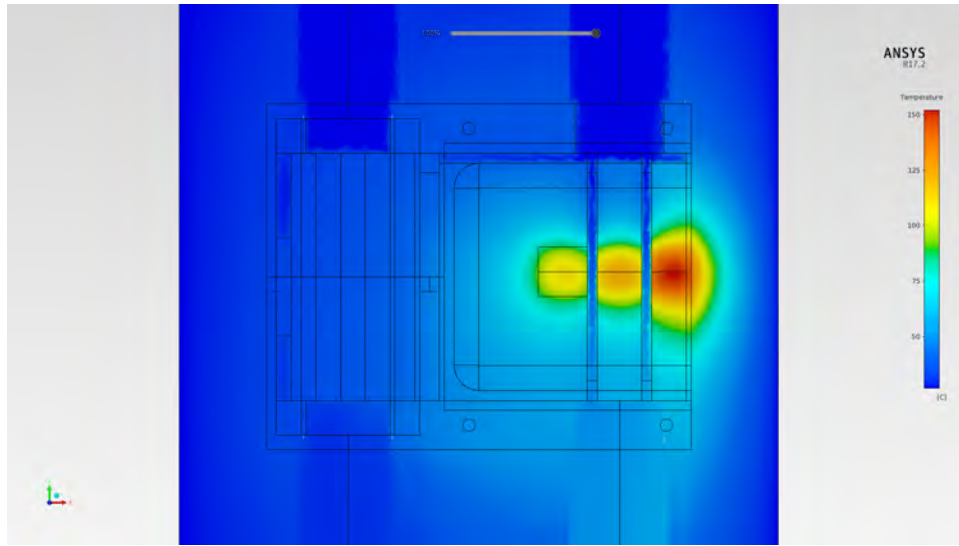
Figure 3.22. ANSYS Simulation of Heat Generation inside the Tungsten Blocks

Similarly, the temperature distribution along the plane at the device location was simulated and shown in Figure 3.23. The simulation showed that the max temperature inside the tungsten was 152°C and the maximum temperature at the circuit-board slots was 63°C. These temperatures mean that the cooling system was able to decrease the temperature at the device location down by 59 percent of the maximum converter temperature. A temperature of 63°C is significant; however, it is far below the temperature that these devices are rated at.
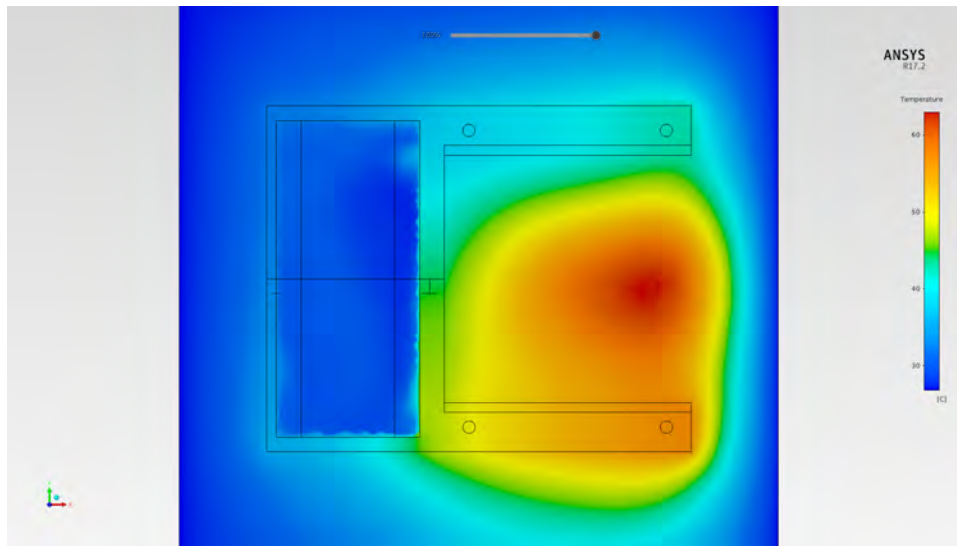
Figure 3.23. ANSYS Simulation of Heat Distribution along the Side of the
Converter at the Device Location

3.5   Testing and Results of the Photoneutron Converter

Fox Welding out of Marina, CA welded the cooling system around the tungsten converter,
and the final product is shown in Figure 3.24. The setup of the converter with the LINAC
consisted of connecting the converter to the water cooling system for the LINAC and the
centering of the converter in the beamline in close proximity of the beam window in order
to test the converter flux output. The photoneutron converter was connected to the LINAC
cooling system by attaching a hose to the front bottom pipe, connecting the top two pipes of
the converter together, and having the bottom back pipe connect back to the LINAC system.

The cooling system was tested and was able to cool the side of the converter down to about
115°C with the DUT board location reaching a maximum temperature of 70°C when the
LINAC was on. This amount of cooling was sufficient to place our devices next to the
converter and know that they would not fail due to overheating. The converter setup with
the LINAC is shown in Figure 3.25. The converter setup in Figure 3.25 shows the LINAC
beam window on the left and the aligned converter on the right. The cooling hose can be
seen attaching the inlets of the converter.

After the photoneutron was centered on the window of the LINAC, the circuit boards with
the dosimetry coupons were inserted into the card slot of the converter and screwed into the

61
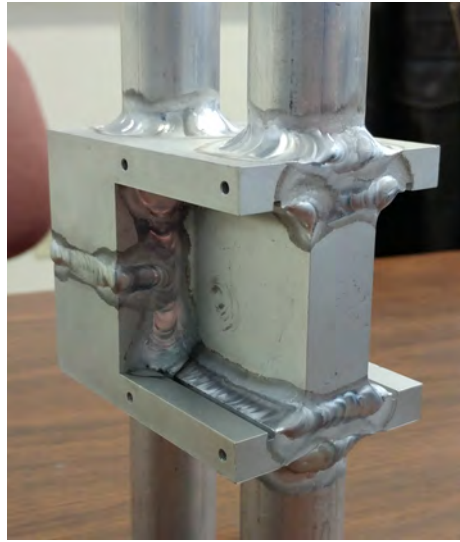
Figure 3.24. Complete Fabrication of the Photoneutron Converter including the Welded Cooling System
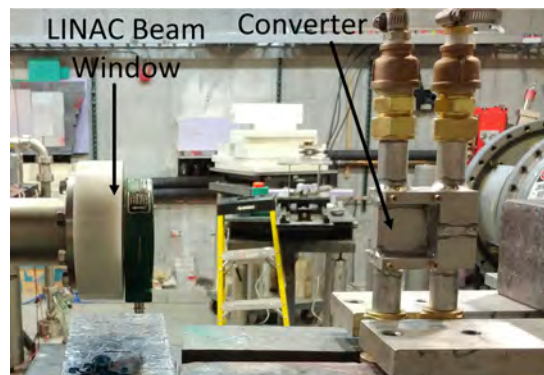
Figure 3.25. Photoneutron Converter Alignment with LINAC

side of the converter. IAC utilized the gold (Au)/Indium foil-activation technique in order to measure the dosimetry of the converter. The activation foils were placed at three positions on an un-populated DUT board and four positions on an un-populated breakout board. The illustration of the positioning of the Au/Indium foils for the photoneutron converter testing is shown as Figure 3.26. The coupons were placed on the DUT board and breakout board for neutron-flux dosimetry measurements with the front of the converter on the left side of the boards.

These positions were determined by simulating a neutron-flux image in MCNP on the full converter design at the DUT board and breakout-board locations. The DUT board is located
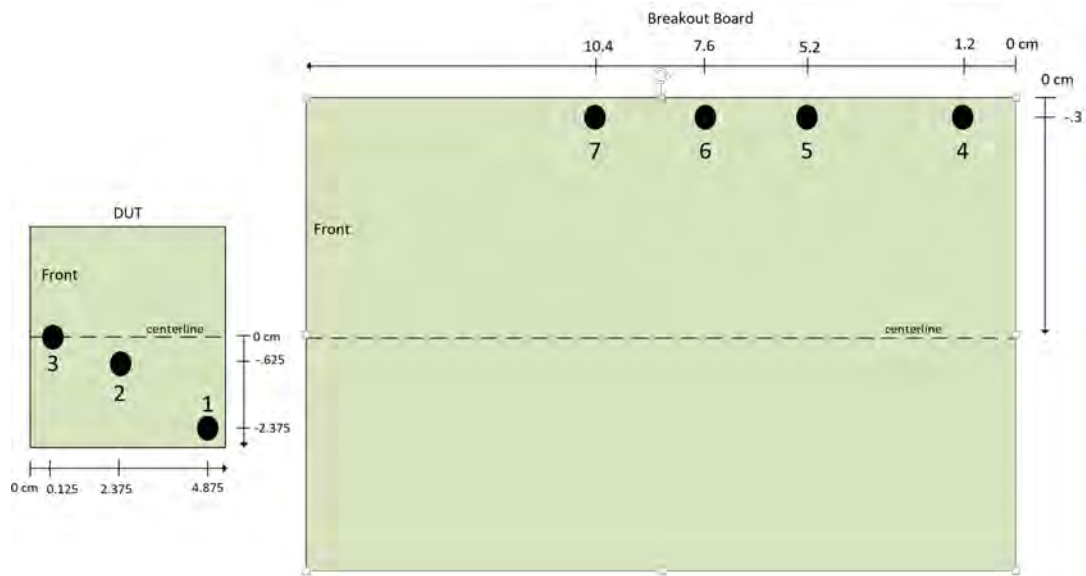
Figure 3.26. Gold/Indium Foil Locations for Dosimetry

1 cm from the side of the converter, and the breakout board is roughly 3 cm from the side of the converter. This simulation was completed to locate the positions of a linear decrease in flux from the maximum flux of $1 \cdot 10^{-4}$ n/(cm$^2 \cdot$e) at coupon position 3 to the minimum flux $2.5 \cdot 10^{-6}$ n/(cm$^2 \cdot$e) measured at position 4. The varied positions distributed the coupons in order to lower the uncertainty of the dosimetry measurement. A picture of the un-populated DUT and breakout boards fitted with the Au and Indium foils is shown in Figure 3.27. The coupons were placed on the DUT board and breakout board for neutron-flux dosimetry measurements with the front of the converter on the right side of the boards.
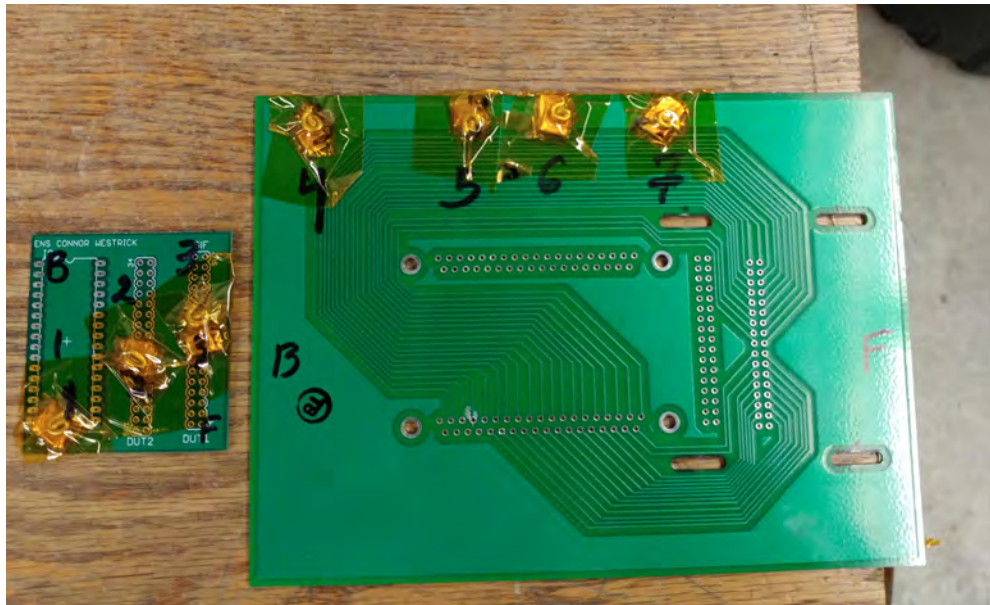
Figure 3.27. Gold/Indium Foil Placement for Dosimetry

IAC used a thermalizing-dosimetry technique to measure and test the neutron flux of the photoneutron converter. Polyethylene plastic was used to surround the converter and thermalize the fast neutrons emitted from the converter. This thermalizing technique was used to give the neutrons higher cross sections for interaction with the foils. By thermalizing, the measurement is an average count of the total neutrons in the thermalized area. The thermal cross section was calibrated by measuring the neutron flux for two hours inside a thermalizing chamber with a Plutonium-Beryllium source of known neutron flux. The thermal test was done to get an accurate measurement of the magnitude of flux achieved by the photoneutron converter.

After placing Au and Indium foils in the radiation field, the activation technique measures the activation of the foils, and from that activation the neutron flux can be determined. The activation is used to measure the flux of neutrons because the gamma decays from the foils are far easier to detect than neutrons. The measurement of this activation is done using gamma spectroscopy with an Ortec High-Purity Germanium detector. The activation of the foils is proportional to the neutron flux that passed through the foils. IAC determined the neutron flux Φ from the cross section determined through the calibration with the Plutonium-Beryllium source, which is calculated as [44]

$$\Phi = \frac{R}{\sigma_{act} N^T},\tag{3.10}$$

where R is the rate of activation within the sample, σ_{act} is the microscopic-activation cross section, and N^T is the total number of nuclei activated. The polyethylene blocks were placed around the converter to simulate a thermalizing chamber for the thermal dosimetry test once the boards were in place along the converter. The electron beam was turned on and the coupons were irradiated for 19 minutes and 30 seconds in order to significantly activate the foils, but refrain from hitting a saturation of activation based on the size of the foils. The foils were then removed, measured, and the neutron flux was calculated. The results of the thermal-dosimetry measurements using the Au/In foil-activation technique are shown in Table 3.1.

Table 3.1. Flux Measurements at the Designated Positions

Coupon Location Number	Neutron Flux
1	$1.97 \cdot 10^{11}$
2	$1.89 \cdot 10^{11}$
3	$1.91 \cdot 10^{11}$
4	$1.38 \cdot 10^{11}$
5	$1.83 \cdot 10^{11}$
6	$2.25 \cdot 10^{11}$
7	$2.3 \cdot 10^{11}$

These flux measurements used a Au/In foil-activation technique while thermalizing the neutron output.

The fluxes measured ranged from $1.38 \cdot 10^{11}$ n/(cm$^2 \cdot$ s) to $2.3 \cdot 10^{11}$ n/(cm$^2 \cdot$ s) with an uncertainty of about one percent. These flux measurements validated the simulation done through MCNP and actually showed that the converter outperformed the simulation predictions. The measured neutron flux correlates to an estimated neutron fluence of $1.8 \cdot 10^{16}$ n/cm^2.

The dose rate of photons was also measured to verify that the photon dose would be low enough so that it does not cause significant damage within the devices. Since photons are much easier to measure than neutrons, they were measured directly using a thermoluminescent dosimeter (TLD). The dose rate measured off the side of the converter where the

devices were tested was 8.3 Rad/s. The dose rate measured correlated to 750 kRad absorbed throughout the 25 hours of the experiment.

The design, simulation, and testing of a photoneutron converter optimized for maximum-neutron production were explained in detail in this chapter. The testing results measured a fast-neutron flux of roughly $2 \cdot 10^{11}$ n/(cm$^2 \cdot$ s), which was close to the values predicted in the MCNP simulations. The cooling system was effective in bringing the side of the converter down to 70°C, which provided a cooled area for the tested parts to be placed for the radiation experiment. The next chapter discusses the design and implementation of an in-situ testing system used to measure the GaN HEMTs.

CHAPTER 4:
Experimental Methodology

The design and implementation of the experimental procedure for testing the GaN-on-Si HEMTs are discussed in this chapter. First, the device's heterostructure and electrical parameters are discussed to explain what was measured in the experiment. Next, the design of the hardware in-situ measurement system is presented followed by the explanation of the static and dynamic DC measurements conducted on the devices during the experiment.

4.1 Device Under Test

The HEMTs tested in this experiment were fabricated by the Naval Research Laboratory (NRL). NRL provided NPS with GaN-on-Si heterojunction HEMTs with AlGaN-buffer layers and Au/Ni gates. The GaN-on-Si substrate was grown via a MOCVD method from Nitronex Inc. The heterostructure consists of a substrate layer, buffer layers, GaN layer, piezoelectric-insulating semiconductor, and metal contacts. The buffer layers and the piezoelectric-insulating layer all consist of different mole fractions of AlGaN. The thickness of the Si substrate t_{Si} is 750 μm. The thicknesses of the silicon nitride (Si2N3), AlN, $Al_{0.7}Ga_{0.3}N$, $Al_{0.6}Ga_{0.4}N$, GaN, $Al_{0.27}Ga_{0.73}N$, Ni, and Au layers are $t_{Si2Nx} = 100 - 200$ nm, $t_{Au} = 300$ nm, $t_{Ni} = 30$ nm, $t_{AlGaN1} = 17.5$ nm, $t_{GaN} = 800$ nm, $t_{AlGaN2} = 300$ nm, $t_{AlGaN3} = 400$ nm, $t_{AlN} = 300$ nm, $t_{Si2N3} = 2$ nm, and $t_{Si} = 750$ μm respectively, and are labeled on an illustration of the GaN-HEMT gate stack in Figure 4.1.
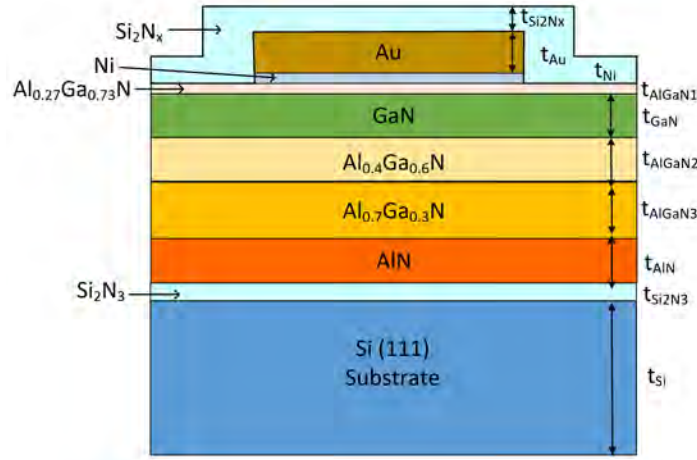
Figure 4.1. GaN/AlGaN-HEMT Gate Stack. Adapted from [45].

The AlN layer of the Nitronex wafer was first grown on the Si substrate to create a poly-crystalline AlN layer with a favorable lattice orientation in the c-direction. The use of AlN allows AlGaN to be grown on top of the AlN layer and further filter out the lattice mismatch. As the growth process continues, the AlGaN buffer layers have continually decreasing Al mole fractions in order to get a closer lattice match to the GaN crystalline structure and larger c-direction preference for the lattice. This process is able to filter out the majority of the original dislocations by the end of the buffer layers. The growth of device quality GaN is then possible without producing too many dislocations and other defects within the material. A list of the significant fabrication parameters and a list of the common device characteristics for the GaN-on-Si HEMTs that were tested is given in Table 4.1.

Table 4.1. List of Fabrication Parameters (left) and Common Device Characteristics (right)

X_{AlN}	0.27
t_{AlGaN}	17.5 nm
Gate Metal	Ni/Au
Ohmic Contact	Ti/Al/Ni/Au Alloy
Substrate	Si (111)
Passivation	SiN$_x$

Voltage Threshold	-2 V
Subthreshold Slope	136 mV/dec
Gate Leakage	-30 μA
Electron Mobility	500 cm^2/(V · s)
n_{2DEG}	$5.55 \cdot 10^{12}$ cm^{-2}

4.2 Measurement System Design for In-Situ Testing

The objective for the design and implementation of an in-situ testing platform was to develop a Kelvin (4-wire) system that could automatically switch between a number of packaged devices over a long distance. The automated switching is imperative since the experiment room will be activated when the LINAC is powered on. The Kelvin system is also essential since the control and measurement needs to be at a long distance from the devices in order to keep the equipment and personnel out of the radiation field. The Kelvin system mitigated the effects of increased resistance over the distance using a force and sense wire for every connection.

The flow chart that represents the experimental testing system designed for this experiment is given in Figure 4.2. A LabVIEW program controls every piece of equipment through a GPIB network except for the LINAC which is controlled by the LINAC operator. Using a GPIB network to connect all the equipment allowed for easy automation and control of the entire system within a single LabVIEW program. The equipment included a DUT board, a breakout board, an Agilent B1500 Semiconductor Analyzer, a Keithley 707 Switching Matrix, and a control computer with LabVIEW. An Agilent B1500 provided the means of biasing and testing the device characteristics of the HEMTs. The Keithley 707 parallels multiple matrices of mechanical switches that were used to connect the input signal to multiple outputs.
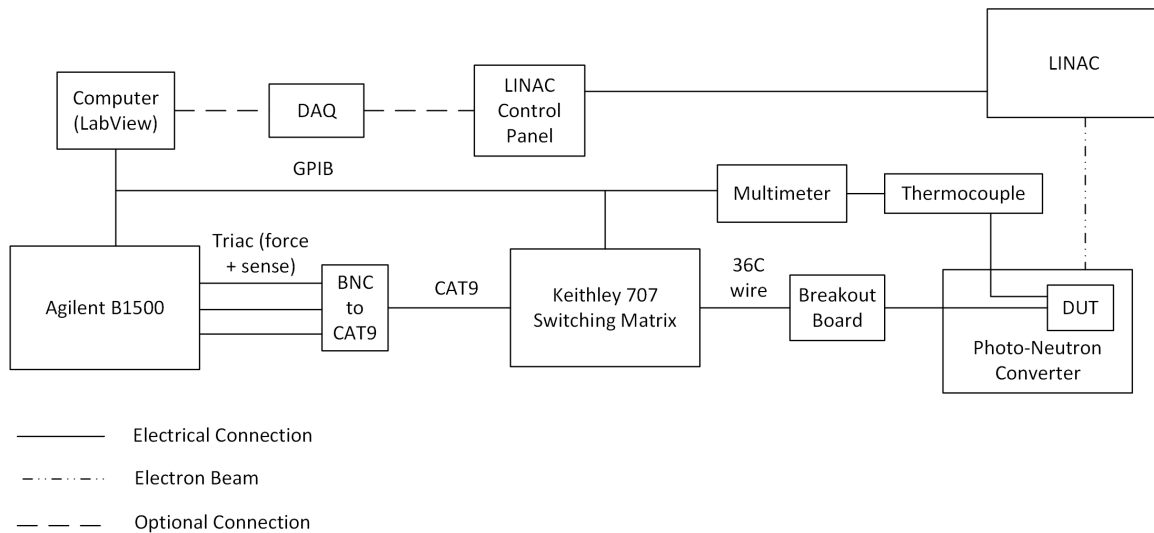

Figure 4.2. Experiment Setup Flow Chart

69

The design of the testing platform began at the device level with the design and fabrication of a device-under-test circuit board and breakout circuit board. The DUT board was designed to be as small as possible in order to fit the small radiation window of the photoneutron converter. The DUT board held a 32-pin DIP socket and two 32-pin female sockets that interfaced with a breakout board. The breakout board is used to take the connections from the smaller DUT board and convert them into connectors that can be connected to the testing equipment which were too large for the DUT board. The breakout board includes male connectors that match the connectors on the DUT board and two 37-pin female DSUB connectors. The breakout board also maintains the integrity of the Kelvin measurement by keeping the force and sense lines separate. The circuit boards were designed in Easily Applicable Graphical Layout Editor (EAGLE) CAD software. The boards were fabricated by Advanced Circuits Inc. and populated in the Microelectronics Laboratory at NPS.

The final hardware design consideration was for a system to connect the three source measurement units (SMUs) that are required to make the necessary electrical measurements with each of the ten HEMTs. One SMU is required for the drain, source, and gate of the transistor; therefore, each of the three SMUs needed to make ten connections each to be able to connect to all ten devices. Each SMU has a force and a sense connection which needed to be carried to the device as separate signals to carry out the device connections. To accomplish this task, two 36-conductor shielded wires needed to be modified to interface with the 37-pin DSUB connectors and transfer the signals out of the LINAC room to the control room. The two cables were then split into four 25-pin DSUB connectors that interfaced with the output of a 707 Keithley Switch Board Matrix. The switch board matrix holds the task of taking the six SMU signals and distributing them to each of the ten devices in sequence. This ensured that no connections needed to be physically reconfigured once the experiment began. The last stage of the in-situ set up was to use a BNC to CAT9 converting circuit and a CAT9 to 25-pin DSUB wire to take the SMU signals and input them into the switch board matrix. This test set up is ideal for in-situ measurement because it can be controlled by a LabVIEW program that will automatically trigger the switch board matrix and the B1500 while the experiment is underway. The LabVIEW program developed was ran at hour intervals when the LINAC was powered down. The program controlled the switch board to make the necessary connections between the B1500's SMUs and the correct pins on each of the transistors. The static and dynamic DC tests were measured and the

data collected for each device before, during, and after the experiment. The experimental set up between the computer, B1500, switch matrix, breakout board, and DUT board in the NPS Microelectronics Laboratory which was tested and verified before conducting the experiment at IAC is shown from right to left in Figure 4.3.

Figure 4.3. In-Situ Experiment Setup

4.3 Testing Techniques and Analysis

A collection of LabVIEW programs was developed and integrated into the experimental setup in order to automatically run the electrical tests on the devices during the experiment. LabVIEW was used because it allows for easy communication between testing equipment and easy control based on the equipment command structures. Four static-DC measurements and one pulsed-DC measurement was measured to characterize the GaN transistors relative to the radiation dose received during the experiment. Threshold voltage, gate leakage, active-region mobility, subthreshold slope, and access resistances of the source and drain were measured from the four static measurements. Dynamic on-state resistance was measured using a pulsed-DC measurement. Kelvin connections to the devices allowed the signal integrity of the DC measurement to remain intact, negating the effect of the series resistance of the wires. The dynamic on-state resistance measurement was a multi-channel pulsed test with the fastest pulse being 1000 Hz. The signal integrity was acceptable at a long distance due to the low-frequency measurement. Both types of measurements provide valuable information regarding the internal state of the tested device during irradiation, and will be explored in this section.

4.3.1   DC Id-Vg and Ig-Vg

The first program designed in LabVIEW measured the drain current(Id)-gate voltage(Vg) transfer characteristics of the device at a constant drain voltage (Vd) of 100 mV and a source voltage (Vs) set to ground. It was important to keep the drain voltage low because increasing voltage would have caused the devices to self-heat, possibly annealing some of the damage caused by the experiment and skewing the results. The gate voltage was swept from -4 V to 1 V. The common response for the GaN HEMTs is for the drain current to increase as the device turns on until the current saturates. Gate current (Ig) was measured simultaneously with the drain current. The general $I_d - V_g$ response of a GaN-on-Si HEMTs is shown in Figure 4.4, while the general $I_g - V_g$ response is demonstrated in Figure 4.5.
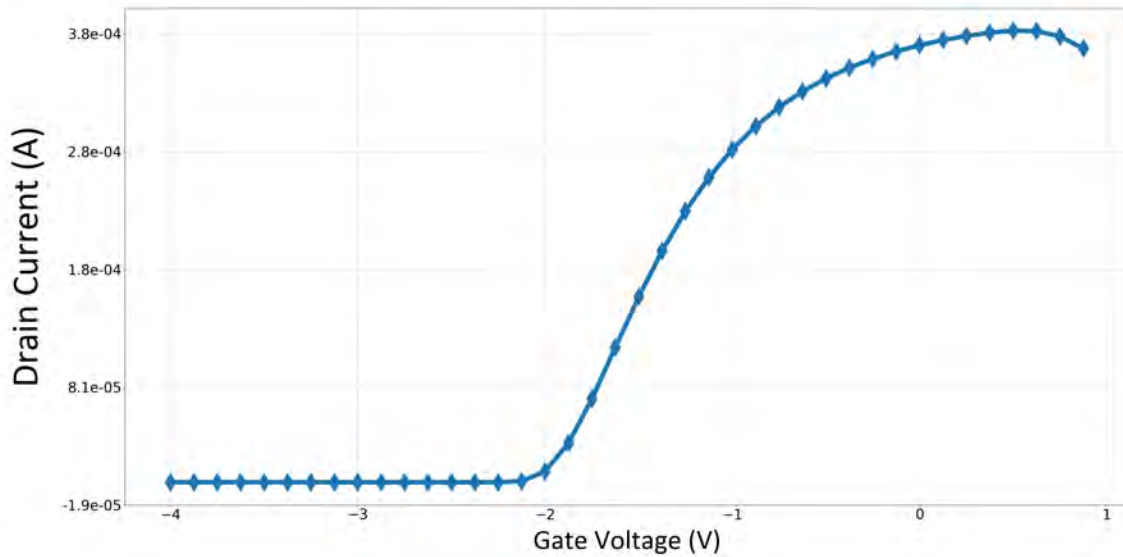

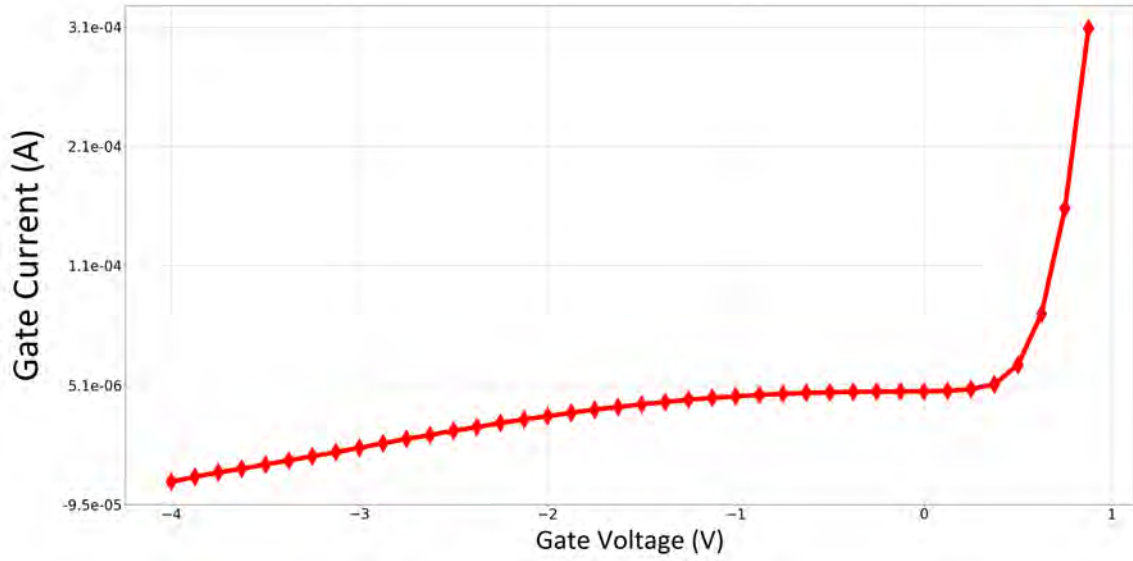Figure 4.4. Traditional Id-Vg Characteristic of a GaN-on-Si HEMT

Figure 4.5. Traditional Ig-Vg Characteristic of a GaN-on-Si HEMT

The gate leakage was evaluated by measuring the gate current at a gate voltage of -4 V from the $I_g - V_g$ measurement. The device properties obtained from the $I_d - V_g$ measurements are the threshold voltage, subthreshold slope, and active-region mobility. The threshold voltage is obtained by doing a linear-regression fit to the linear portion of the $I_d - V_g$ relationship. The threshold voltage is the x-intercept of that linear fit. The logarithmic of the drain-current data was plotted versus the linear gate voltage to find the subthreshold slope. Taking the logarithm linearized a portion of the data below the threshold voltage. The subthreshold slope can be obtained by fitting a linear regression to this portion of the data and taking the inverse of the slope. The last parameter that can be divulged from the $I_d - V_g$ measurements is the active-region electron mobility. The mobility is derived from the slope of the linear region of the I-V curve that was fit in order to find the threshold voltage. The mobility μ is given as

$$\mu = \frac{mL}{W C_{eff} V d (1 - m R s)},$$ (4.1)

for small values of $V_g - V_{TH}$, where m is the slope from the linear fit, L is the gate length, W is the gate width, C_{eff} is the effective capacitance, Vd is the drain voltage, and Rs is the source access resistance which will be discussed in the next section. It can be seen that the

73

active-region mobility is not proportional to the slope of the $I_d - V_g$ characteristic, but it can be derived from it. Mobility can be used to gauge radiation damage within GaN HEMTs because the mobility is directly dependent upon the degree of radiation damage.

4.3.2 Access Resistance Measurement

Another LabVIEW measurement program was developed to measure the drain and source access resistances, $R_D + R_C$ and $R_S + R_C$, via the gate-probe method. The gate is forward biased with constant current I_g in the gate-probe method. The voltage drop across the Schottky barrier V_B of the gate is given as [12]

$$V_B = \eta \frac{kT}{q} ln\left(\frac{I_g}{I_s}\right).$$

(4.2)

The gate voltage V_{GS} is related to the drain current as

$$V_{GS} = V_B(I_g) + I_D(R_S + R_C),$$

(4.3)

where R_C is the contact resistance. Note that this relationship is only valid if the drain voltage V_D is applied, inducing a drain current to flow. This measurement must be performed in the linear region of the $I_D - V_D$ characteristics of the device, which can be accomplished by constraining the drain voltage to between 0 V and 0.3 V. This measurement was also done on the source side of the transistor in order to characterize the drain access resistance $R_D + R_C$. The source current was measured while the source voltage was swept from 0 V to 0.3 V and the gate was kept at a constant current. The gate was also varied to examine the variation of the access resistance.

The resistance is easily calculated by finding the slope of the linear relation between the drain current and the drain voltage where voltage is on the y-axis. This was done within LabVIEW using the linear-fit block in the mathematics tool-kit. The gate-probe measurement was repeated for gate currents of 1nA to 1uA in 100 nA steps. The slopes of each test give the access resistance of the drain. The calculated resistances were plotted versus the increasing gate current in order to examine the variation of access resistance

74

against gate bias; such variation is indicative of polarization field induced scattering [46]. The shape of this relationship often varies drastically from device to device, and also varies significantly with different geometries. This geometry variation makes it difficult to compare values between devices, but the neutron damage can be compared within the same device for different neutron-fluence levels. The source access resistance was also used to calculate the mobility as discussed in Section 4.3.1.

4.3.3 Dynamic On-State Resistance Measurement

A multi-channel pulsed test was designed in LabVIEW in order to measure the dynamic on-state resistance of the devices. The test consisted of a staircase-pulsed sweep of the drain voltage and a constant-pulsed voltage for the gate applied simultaneously. The drain was kept at a stress voltage ranging between 5 V and 20 V in the off-state of the pulse, while the gate was kept at a voltage of -4 V. After a three second hold time at the stress voltage, both channels pulse to their respective on-bias voltages for 1 ms. The drain pulses down to between 0 V and 1 V and the gate pulses up to 0 V in the on-bias state of the pulse. This pulse causes the device to turn on and the drain current to be measured at the end of the pulse. After the current is measured, the SMUs return to the stress voltages and maintain those voltages for the hold time of three seconds. This pulse sequence repeats while the drain bias voltage sweeps up from 0 V to 1 V, and the drain current is measured every time the device is pulsed on. The test is repeated for drain stress voltages ranging from 5 V to 20 V. This measurement probes the region at the edge of the gate on the drain side of the transistor, as explained in Chapter 2. Dynamic on-state resistance allows for the effective traps at those points to be characterized.

Resistance was calculated from the I-V data obtained from the pulsed test in the same fashion as the access resistances. The slope of the linear relationship was the resistance and this resistance was plotted versus the increasing stress voltage by applying the linear-fit block from LabVIEW. The general trend in these devices is an increasing dynamic $R_{DS,on}$ value for increasing stress voltage. The common trend of increasing resistance as stress voltage increases is shown in Figure 4.6.
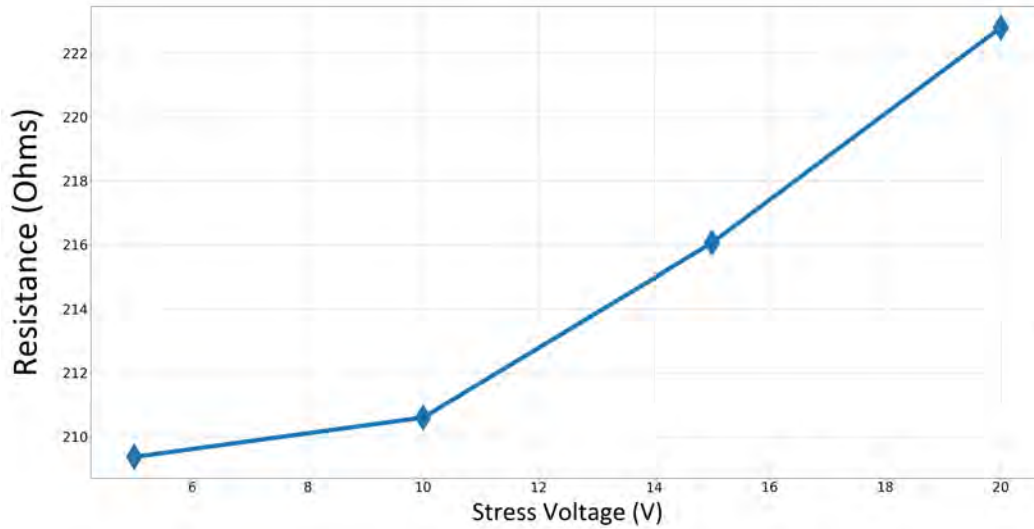
75

Figure 4.6. Dynamic On-State Resistance versus Drain Off-State Stress Voltage of a GaN-on-Si HEMT

4.3.4   Experiment LabVIEW Control Program

LabVIEW was used to create a central control program to automate the entire measurement sequence. The designed LabVIEW program controls each piece of measurement hardware directly by using a GPIB network. The panel view of the LabVIEW control program is shown in Figure 4.7.

This program was used to connect and control the Keithley 707 switch matrix, Agilent B1500, breakout board, DUT board, and ultimately the devices under test. The GPIB addresses for the switch matrix and B1500 were input in the top left panels in order to create a VISA connection and open a communication path. The group of control panels directly underneath the GPIB addresses are the control blocks for setting up the $I_d - V_g$ and $I_g - V_g$ measurements. The group of control blocks beneath these are the control panels for measuring the access resistances. The final control blocks at the bottom of the LabVIEW panel window control the dual-pulse measurement of dynamic $R_{DS,on}$. The graphs for these tests are shown on the right of the window and give instant results during the measurements. Instant results were imperative to observe the degradation in real time and evaluate potential pre-failure device behavior.

This program controls the measurement by first closing the correct cross-points on the
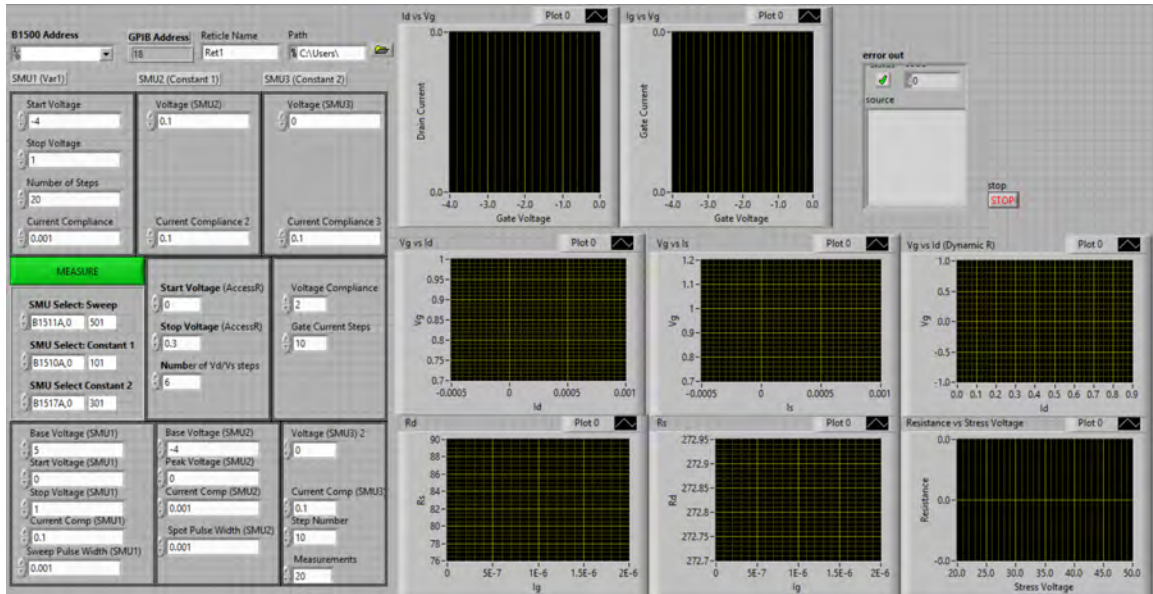
Figure 4.7. LabVIEW Control Program

switch matrix to connect each of the three SMUs to the gate, drain, and source of the first transistor to be measured. The connection between the B1500 and the device is set once the cross-points are closed, so the SMUs are enabled and the I-V measurement is run. Next, the access resistance measurements and then the dynamic on-state resistance test is completed in sequence. The graphs update immediately and the data is saved directly to separate data files for each test. After the measurements for the first device are complete, the computer sends a command to the switch matrix to open the closed cross-points and close the new cross-points for the next device. This sequence of events is done automatically until all devices are measured. Separate data files are created for each device and each measurement in order to keep the data organized and easy to analyze after the experiment.

The design and implementing of a fully-automated Kelvin-measurement system including a full suite of LabView device tests were discussed in this chapter. Static and Dynamic IV measurements were designed to measure the threshold voltage, electron mobility, 2DEG concentration, gate leakage, subthreshold slope, source and drain access resistance, and dynamic on-state resistance. The results from the experiment conducted at the IAC are presented in the next chapter.

THIS PAGE INTENTIONALLY LEFT BLANK

CHAPTER 5:
Experimental Results and Analysis

The device parameters discussed in the previous chapter are essential toward evaluating the speed at which fast-neutron radiation damages GaN-on-Si HEMTs. These parameters needed to be measured in-situ during irradiation to fully characterize the damage within the devices. Measuring the device characteristics with respect to increasing fluence allows us to see where there are behavior changes, predict failures, and measure the parameters sensitivity toward fast-neutron radiation. Linear degradation of device parameters was hypothesized because neutrons should theoretically act on the atomic structure with only displacement damage and not ionizing damage. The issue with this hypothesis is that it does not take into account the effects of the secondary particles born from initial neutron damage. This chapter provides the results and analysis of a single device from the experiment to illustrate the common trends seen in all the devices. The device characteristics measured during the experiment from one of the devices tested will be provided in the following sections. Appendix A provides the same measurements described in this chapter but for the other seven devices that were irradiated.

Operating a LINAC for continuous high power operation for high-fluence neutron generation is normally not done because it is difficult to control the electron beam for long durations of time. A LINAC uses various lenses and magnetic couplings to focus the electron beam down to a small cross-sectional area. The electrons will scrape the sides of the LINAC and heat up the metal casing if the beam is too large. Heating from the electrons scraping the vacuum walls can be disastrous for operation because if the metal casing of the LINAC heats up too much, the LINAC vacuum that contains the electron beam can be lost. The only way to keep excess heating from occurring is to position the lenses and magnetic couplings in the perfect alignment for electron beam focusing.

The neutron experiment was conducted at the IAC in Pocatello, ID over the course of four days. The in-situ hardware setup discussed in Chapter 4 was set up in the LINAC control room, and the 36 conductor wires were fed into the LINAC operating room. The initial measurement was taken on each device in order to get the pre-experiment data after the

photoneutron converter was setup in the beamline with the wires from the in-situ setup and the hoses from the cooling system connected. The LINAC was then turned on with an energy of 31 MeV, a pulse-repetition frequency of 180 Hz, a pulse width of 2.5 μs, and a max current of 200 mA. The LINAC was shut down at hour intervals in order to measure the device characteristics for every hour of irradiation. The results of the in-situ measurements against the increasing neutron fluence from the experiment is described in the following sections.

5.1   DC I-V Characteristics

The $I_D - V_g$ transfer characteristics is the first piece of data that needs to be analyzed since it shows the general trend of degradation for these devices. The Id-Vg device response change over the course of irradiation is given in Figure 5.1.
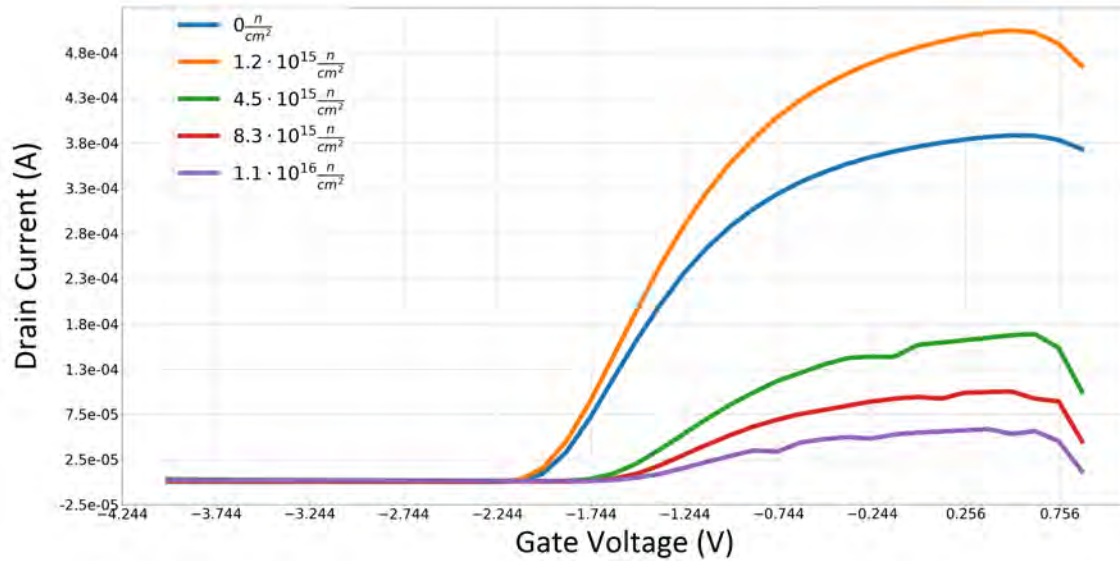

Figure 5.1. Comparison of the Id-Vg Relationship Before Irradiation and at Increasing Neutron Fluence

There are two discernible degradation factors that can be pulled from the information shown in Figure 5.1. First, it can be seen that there is current collapse within these devices, shown by the magnitude drop in the drain current. Interestingly, the device actually improves from the start of the experiment to a fluence of about $1.2 \cdot 10^{15}$ n/cm^2 with an increase in drain current. This fluence correlates with about two hours of irradiation. The device is exposed

to a low level of ionizing dose due to gammas and electrons. This low level of ionizing radiation could be the cause of this brief device improvement. The second degradation factor is the voltage threshold shift to the right showing that the device turns on closer to 0 V after irradiation. This shift indicates that there is a degradation of the equilibrium 2DEG concentration under the gate. These two points of degradation will be investigated further when we look specifically at the change of voltage threshold and the resistances.

5.2   Threshold Voltage

The threshold voltage is plotted versus neutron fluence in Figure 5.2. Each data point represents a measurement taken during the experiment, and as a reference to the timing, these data points were collected every hour of irradiation.
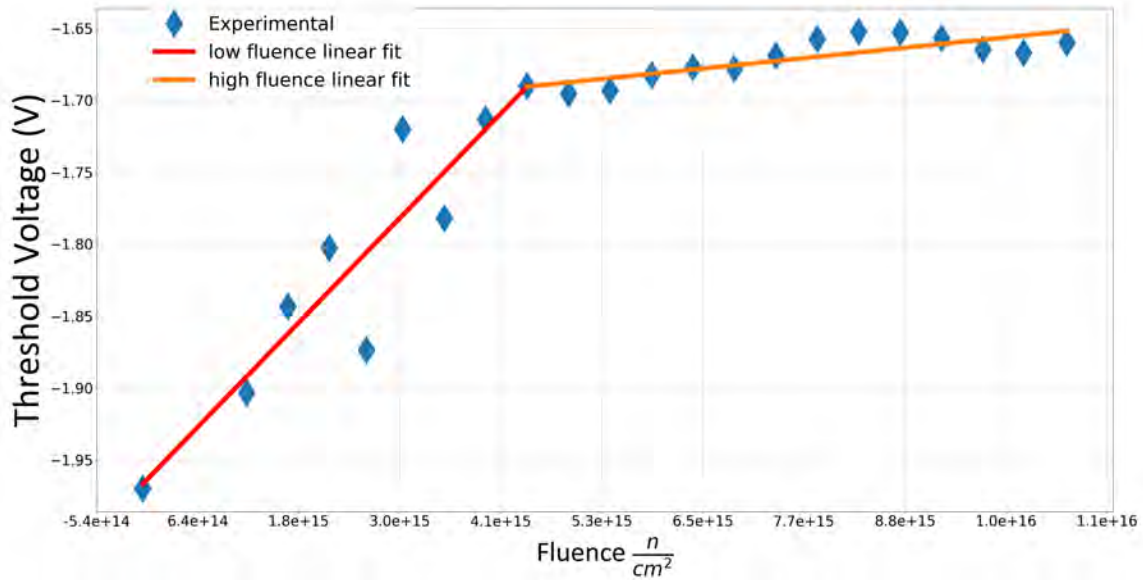

Figure 5.2. Threshold Voltage vs. Neutron Fluence

It can be seen there are two different device behaviors that occur during the irradiation. There is a linear relationship between threshold voltage and fluence with a high rate of change at low fluences and after $4.1 \cdot 10^{15}$ n/cm^2 the device behavior changes and the rate of change slows. Initially, it was thought that this change could have been due to a sudden failure in the experimental set up; however, this was eliminated as a possibility due to that fact that this change occurred at different fluences and therefore different times within different devices. We noted that some devices had such a decrease in their rate of change at $3 \cdot 10^{15}$ n/cm^2 while others were at $5.3 \cdot 10^{15}$ n/cm^2, which corresponds to a 5 hour difference. Linear fits were taken for the low-fluence portion and the high-fluence portion in order to derive the characteristic transfer function for the change of the parameter with respect to fluence. The change in the parameter is proportional to the slope of the linear fit at low fluence α_L since the relation is linear which is $6.2 \cdot 10^{-17}$ (V $\cdot$ cm^2)/n. The slope for the high-fluence region α_H was $6.2 \cdot 10^{-18}$ (V $\cdot$ cm^2)/n. This behavior change shows that the rate of change of the threshold voltage decreases by an order of magnitude at the behavior change point. A 16 percent shift in threshold voltage was seen from the start to the end of the experiment.

5.3   2DEG Concentration

The 2DEG concentration can be determined from the threshold voltage and similarly plotted versus fluence. The 2DEG concentration is important because the performance of the device is directly related to the concentration. HEMTs are able to achieve such high transconductance because the channel accumulates high densities of electrons. Equation (2.10) provides the relationship between the voltage threshold and 2DEG concentration; therefore, a good approximation of the equilibrium 2DEG concentration is given as [12]

$$n_{2DEG} = \frac{V_{TH}C_{eff}}{q}.$$

(5.1)

The effective capacitance C_{eff} of the GaN-on-Si HEMT under review is calculated to be 444 nF/cm^2. The degradation of the equilibrium 2DEG density versus fluence is shown in Figure 5.3. The total degradation of 2DEG density over irradiation was about $1 \cdot 10^{12}$ e/cm^2. The α_L is $-1.7 \cdot 10^{-4}$ e $\cdot$ cm^3 while the α_H is $-1.7 \cdot 10^{-5}$ e $\cdot$ cm^3. This order of magnitude decrease in rate of change was predictable due to the linear relationship between threshold

voltage and electron concentration of the 2DEG, as is the 16 percent shift from the beginning of the experiment to the end.
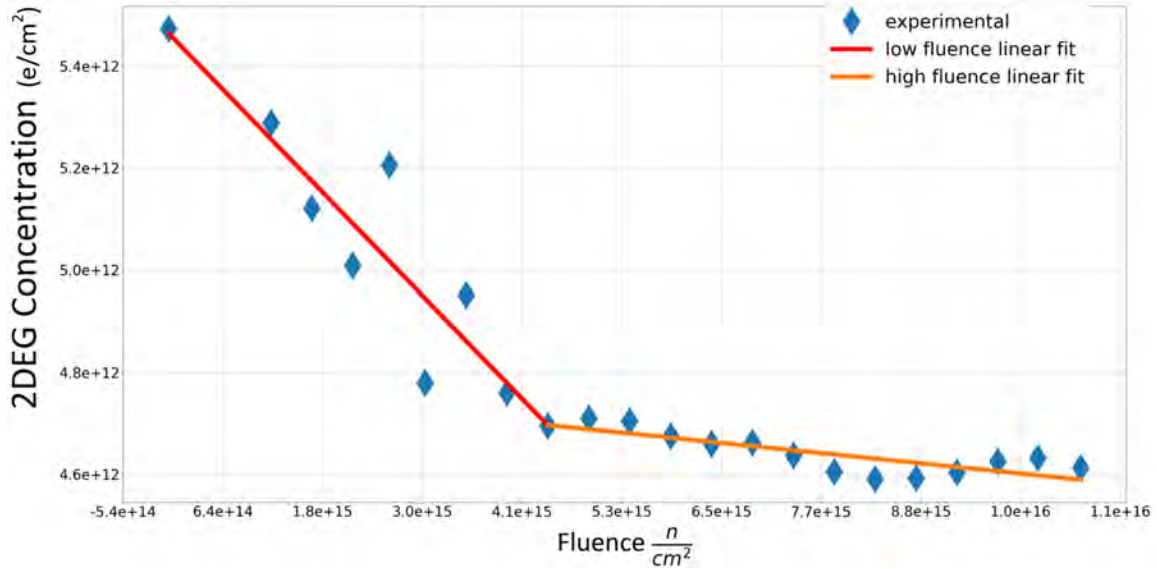

Figure 5.3. 2DEG Concentration vs. Neutron Fluence

5.4   Gate Leakage

The gate leakage is important to measure in order to characterize the performance of the gate control. The less the gate leaks, the better control the gate has over the 2DEG concentration and the functioning of the device. The gate leakage was found at lower fluences to actually decrease as the fluence increased and then remained fairly constant after a fluence of $4 \cdot 10^{15}$ n/cm^2, as shown in Figure 5.4.

The gate leakage was found to predict the catastrophic failure of the devices. It was discovered that the device gate leakage would drastically increase by about two orders of magnitude before device failure. This increase in gate leakage magnitude is not shown in Figure 5.4 because it occurred at the next fluence point and skewed the scaling of the plot, so the two linear behaviors shown were not discernible due to the magnitude difference. The sudden increase in gate leakage indicates that there is a catastrophic damage threshold for these devices. This increase occurs at different fluences per device due to the inherent differences between the devices; however, this increase occurred for most of the devices as the fluence got close to $1 \cdot 10^{16}$ n/cm^2. This data also demonstrates that the gate leakage is

83
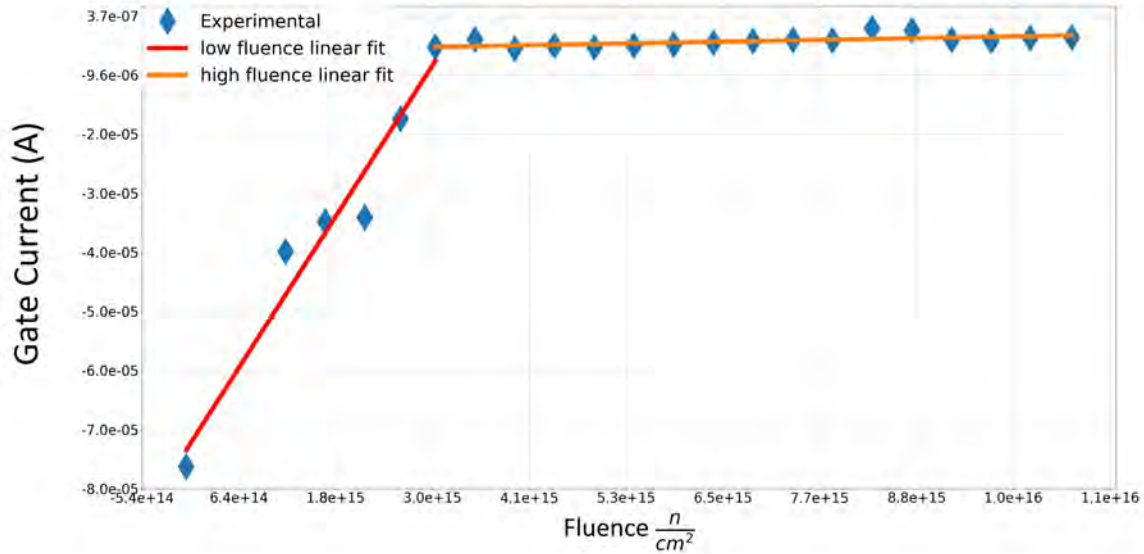
Figure 5.4. Gate Leakage vs. Neutron Fluence

actually quite insensitive to irradiation past $3 \cdot 10^{15}$ n/cm^2. The gate leakage will remain fairly steady as long as the device does not get irradiated to the point of failure. The lower region slope was found to be $2.17 \cdot 10^{-20}$ (A $\cdot$ cm^2)/n while the high region slope was $2.55 \cdot 10^{-22}$ (A $\cdot$ cm^2)/n. Overall, the gate leakage decreased by 96 percent of its original value over irradiation.

5.5   Subthreshold Slope

The subthreshold slope is essential for the analysis of the damage within these HEMTs because it demonstrates the performance of the gate in modulating the drain current. The creation of defects can degrade the magnitude of the control of the gate over the channel. Hence, radiation which induced displacement damage such as neutron radiation causes the subthreshold slope to increase and by association, hinders the gate modulation of drain current. The increase of the subthreshold slope with neutron fluence is demonstrated in Figure 5.5. It is imperative to note that the variation in subthreshold slope in the low-fluence region is non-linear, in contrast to the high-fluence region.

The high region slope was $8.7 \cdot 10^{-15}$ (mV$\cdot$cm^2)/(n$\cdot$dec). The subthreshold slope increased by 140 percent of its original value. This increase in subthreshold slope indicates that the gate of the device is decreasing in its ability to modulate the channel. The subthreshold slope
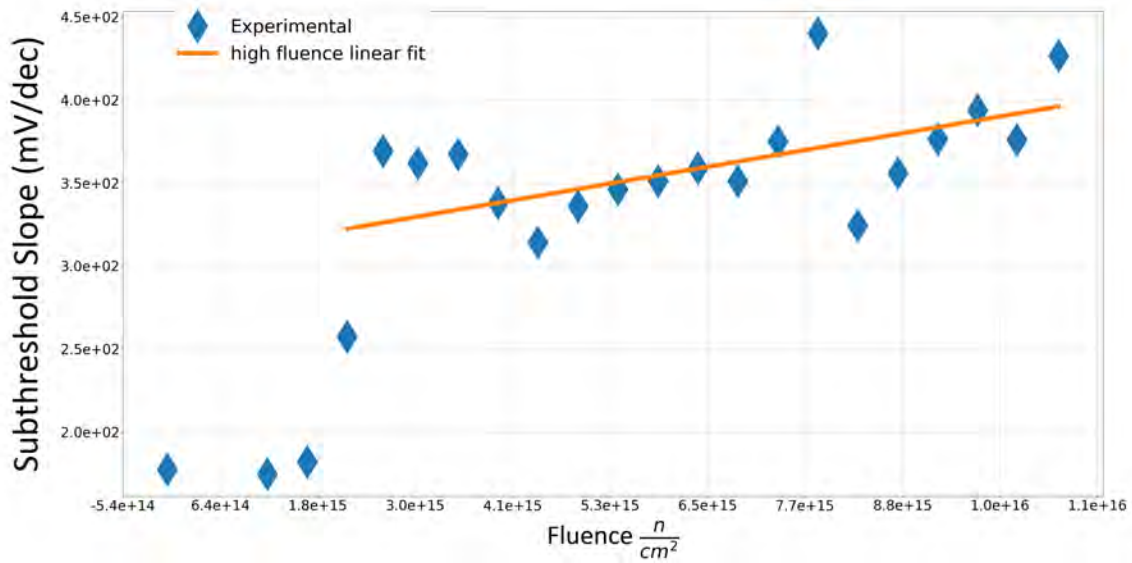
84

Figure 5.5. Subthreshold Slope vs. Neutron Fluence

decrease results from the build up of charge under the gate. The increase in subthreshold slope could be due to neutrons displacing atoms within the device causing defects to build up, screening the 2DEG.

5.6   Active-Region Electron Mobility

The electron mobility is a key parameter that can be used to monitor the quality of the 2DEG channel. HEMTs have increased mobilities over other transistors because the 2DEG is quantum confined, isolating 2DEG electrons from dopant induced scattering, as discussed in Chapter 2. However, the presence of dopants can still negatively effect mobility. Defects introduced via irradiation can degrade the mobility of electrons in the 2DEG channel by creating defect sites in or near the channel region. These GaN-on-Si HEMTs are research devices; therefore, their mobility is not optimal. Equation (5.1) provides the equation for the slope of the drain-gate current relationship in the triode region. This slope is related to the mobility; therefore, the mobility can be calculated from the slope. The change in mobility due to increasing neutron fluence is illustrated in Figure 5.6.

Again the low-fluence region is not linear, but it can be seen that there is little change in the mobility up to a fluence of $2 \cdot 10^{15}$ n/cm^2. This is important to note because the neutron experiment conducted by Iobst described in Chapter 1 was only completed to a fluence of
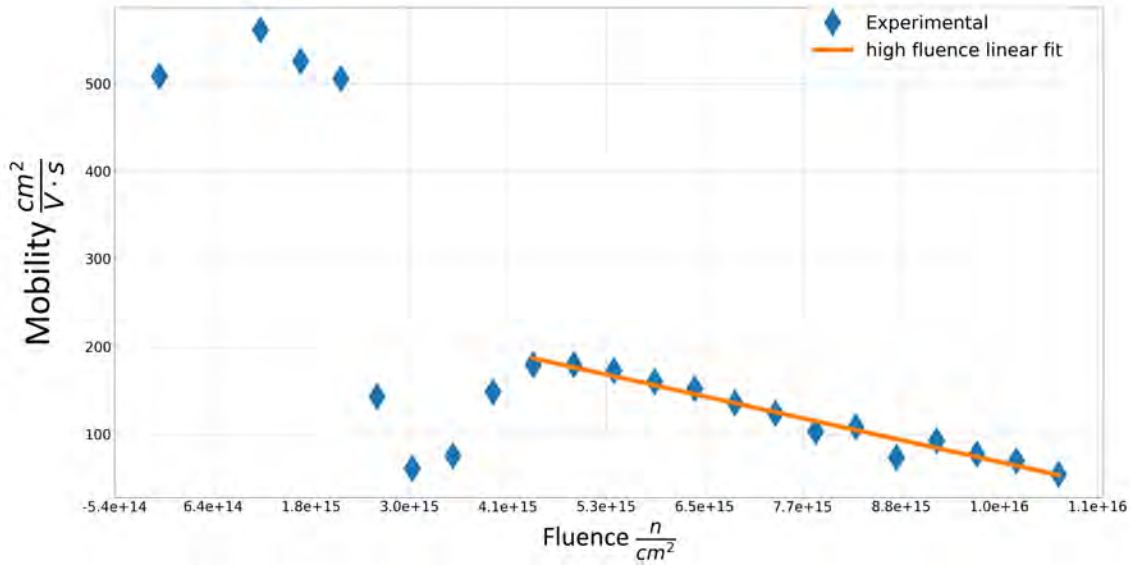
Figure 5.6. Active-Region Mobility vs. Neutron Fluence

about $1.4 \cdot 10^{15}$ n/cm^2. This means that Iobst would not have seen any of these major changes in mobility due to the low fluence achieved in his experiment. There is a major decrease in mobility just above $2 \cdot 10^{15}$ n/cm^2 and a slight recovery shortly after. This response was consistent for all devices irradiated. After this point, the mobility decreases linearly with fluence. The slope of the linear fit was $-2.1 \cdot 10^{-14}$ cm^4/(V · s · n)/n with a total change of 97 percent from the original mobility value.

It is difficult to explain the low-fluence behavior of the mobility, but the most likely explanation is that early on the neutrons create traps within the material, while the ionizing radiation frees electrons at a similar rate. This explanation accounts for the stability of the mobility early on in the experiment, but as the neutron fluence continues to increase it overwhelms the ionizing radiation damage completely, accounting for the dramatic decrease in mobility. The mobility continued to decrease in a linear fashion as predicted once the neutron displacement damage became the leading degradation factor.

5.7   Source Access Resistance

The variation of the device access resistances will be examined next. The source access resistance began as a much lower resistance than the drain resistance due to the geometry of the devices. The source to gate region is much smaller than the drain to gate region

which inherently leads to a lower resistance. However, this resistance decreased further as the device was irradiated, as shown in Figure 5.7.
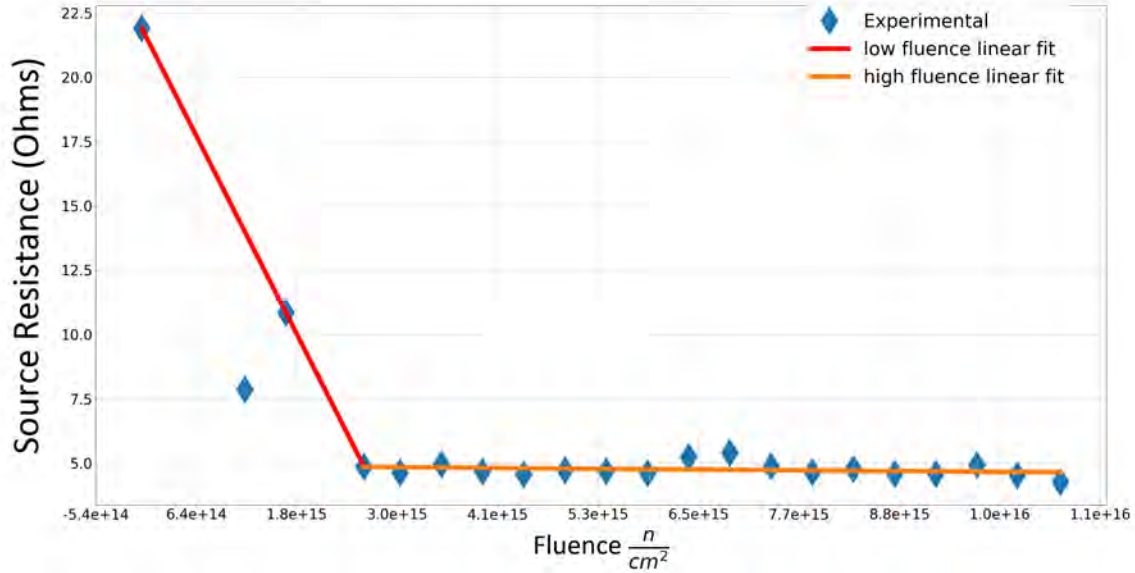

Figure 5.7. Source Access Resistance vs. Neutron Fluence

There is a similar two-region linear relationship between source access resistance and fluence as the threshold voltage and gate leakage. The source resistance drops quickly after a few hours of irradiation, but then continues to change slowly after around $3 \cdot 10^{15}$ n/cm^2. This point corresponds to the point of similar behavior change in the other device parameters. The slope of the low-fluence behavior was $-6.6 \cdot 10^{-15}$ ($\Omega \cdot$ cm^2)/n, the high-fluence data had a slope of $-2.7 \cdot 10^{-17}$ ($\Omega \cdot$ cm^2)/n, and the total change in source access resistance was a 78 percent decrease. This discovery is almost contradicting to the discovery that the gate-channel mobility decreases with neutron fluence; if source access resistance decreases, it is most likely that any decrease in electron mobility is offset by a shift in the equilibrium 2DEG density within the device. However, based upon the behavior of the device characteristics beneath the gate, it would be expected that the access region would experience a simultaneous drop in 2DEG density and mobility. This data could imply that there is a non-uniform distribution of damage within the device. The access regions differ from the active region of the device by the use of Au/Ni/Al/Ti-alloy ohmic contacts. The titanium within the contacts is not present in the gate region; therefore, further investigations need to be conducted into the possibility of the titanium causing different

87

damage effects than the other materials of the gate. The drain access resistance needs to be compared with the source access resistance to see if the drain access resistance follows the same relationship as the source access resistance and provide further evident towards this hypothesis.

5.8 Drain Access Resistance

The drain access resistance only differs from the source access resistance by its magnitude due to the length to the gate. Unfortunately, the data reading at lower fluences were missed for this measurement, so there is a small gap in knowledge of the drain access resistance response to neutron radiation. However, the drain access resistance can be successfully compared to the source access resistance with the test carried out before the experiment and the successful tests at higher fluence levels. The shape of the data is found to be very similar. The relationship of the drain access resistance to neutron fluence is shown in Figure 5.8 and conforms to the rest of the data with a linear relationship at high fluences.
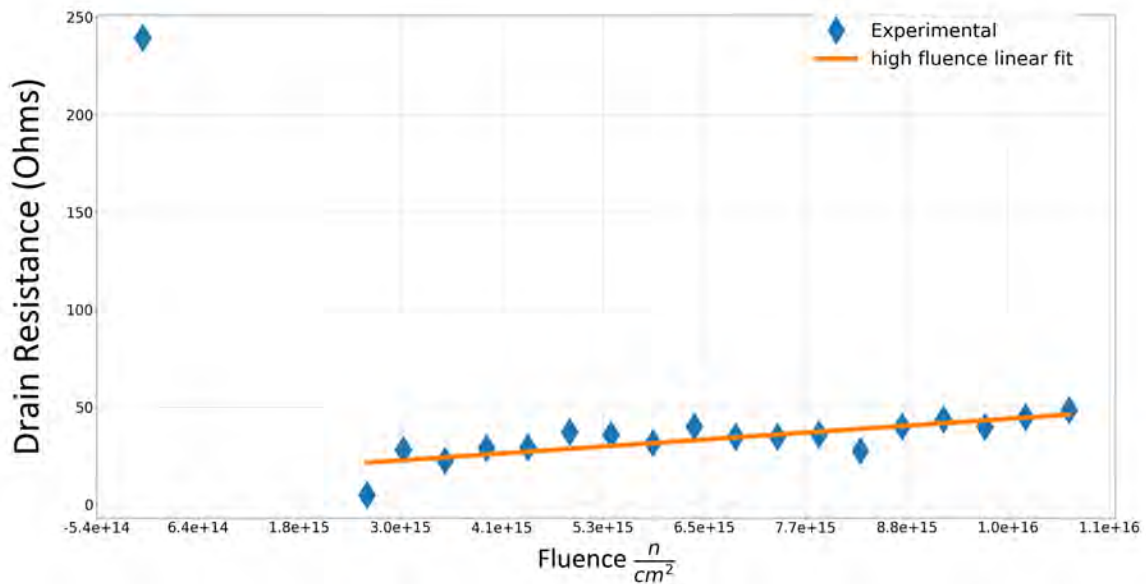

Figure 5.8. Drain Access Resistance vs. Neutron Fluence

The slope of the high-fluence fit to the measured data was $3 \cdot 10^{-15}$ $(\Omega \cdot \text{cm}^2)/\text{n}$, and the total change in drain access resistance over the course of the experiment was 81 percent. Both source and drain access resistances show a quick decrease in resistance and then

a slow increase after the fluence point of behavior change around $3 \cdot 10^{15}$ n/cm^2. This finding provides further evidence that at lower fluences, the ionizing radiation frees traps at deep levels within the device that have long time constants while the displacement damage overtakes the ionization damage at certain fluence point within the device. The drain access region seems to be more sensitive to the radiation; this could be due to the longer source-drain length and source-drain area in which damage can occur.

5.9 Dynamic On-State Resistance

The dynamic $R_{DS,on}$ measurement was different from the others because it was a pulsed-DC measurement instead of a static measurement. Dynamic $R_{DS,on}$ measurements probe the charge state of the traps within the gate-drain access region of the device by measuring the effects of drain current collapse, as discussed previously. Thus, the dynamic on-state resistance is expected to be highly sensitive to radiation damage. The dynamic resistance measurements for each stress voltage as a function of fluence is shown in Figure 5.9.
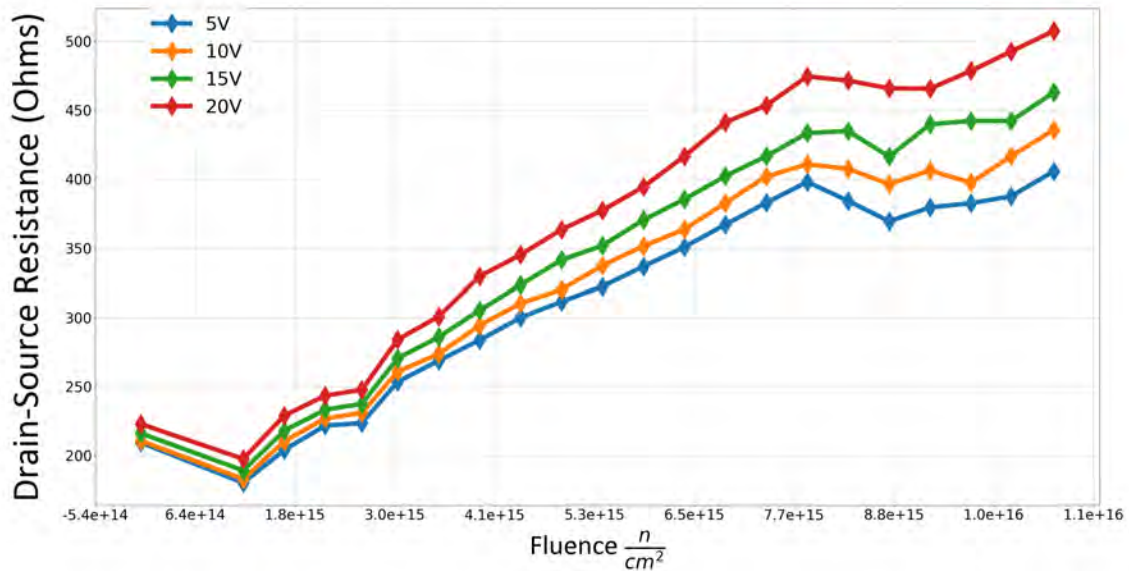

Figure 5.9. Dynamic $R_{DS,on}$ vs. Neutron Fluence

This parameter proved to be the most sensitive with a total parameter change of 150 percent from the original value before irradiation. There are a few regions of fluence that need to investigated and discussed within this measurement. The first is during the region from the first data point to the second. This region shows a decrease in resistance similar to the

other measured resistances, but at a much lower magnitude than the decrease seen by the measurements of the DC source and drain access resistances. The second region consists of the next few data points were there seems to be a non-linear relation to fluence. The third region is the high-fluence region up to about $8 \cdot 10^{15}$ n/cm^2, and the last is the remaining data points at the highest fluence levels. This dynamic $R_{DS,on}$ response was consistent for all irradiated devices with some variations in the fluence level that causes the device behavior change. The majority of the parameter change with respect to neutron fluence level is linear, especially at higher-fluence levels, which can be correlated to the fast-neutron displacement damage.

5.10 Analysis of Neutron Damage in GaN-on-Si HEMTs

The analysis of the degradation due to displacement damage with the GaN-on-Si HEMTs can be clearly seen from the linear change of the device parameters that was just revealed. Additional details are provided in the next section where the calculation of total displacement damage will be conducted and compared to the proton damage found in Koehler's experiment and the low-fluence neutron damage discovered in Iobst's experiment.

5.10.1 Displacement Damage Calculation

The number of displacements within each layer of the device is crucial for determining the damage and the effects of this damage on the device characteristics. This section will utilize the equations introduced in Chapter 2 Section 2.4 to calculate the rate of displacement per unit volume for each of the main layers of the GaN-on-Si HEMT. These layers include the Au, Ni, AlGaN, GaN, and Si layers of the device as well as the Au/Ni/Al/Ti-alloy ohmic contacts. The total displacements per volume of each layer can be derived from the rate of displacements. This section will go through the calculation for the GaN layer as an example of the total displacements calculation and then provide the results for each of the layers specified. The elastic cross-section data for the gallium and the nitrogen for the GaN layer of the device were used from the Evaluated Nuclear Data File (ENDF) database. The elastic cross section changes with respect to the incoming-particle energy. The cross section decreases as the incoming-particle energy increases. The incoming particles for this experiment are neutrons with the majority of the flux from $1 \cdot 10^{-4}$ MeV to 30 MeV. The elastic cross section for Ga-69 is shown in Figure 5.10. The other element

in GaN is Nitrogen-14, which has a far different elastic cross-section relationship, which is demonstrated in Figure 5.11.
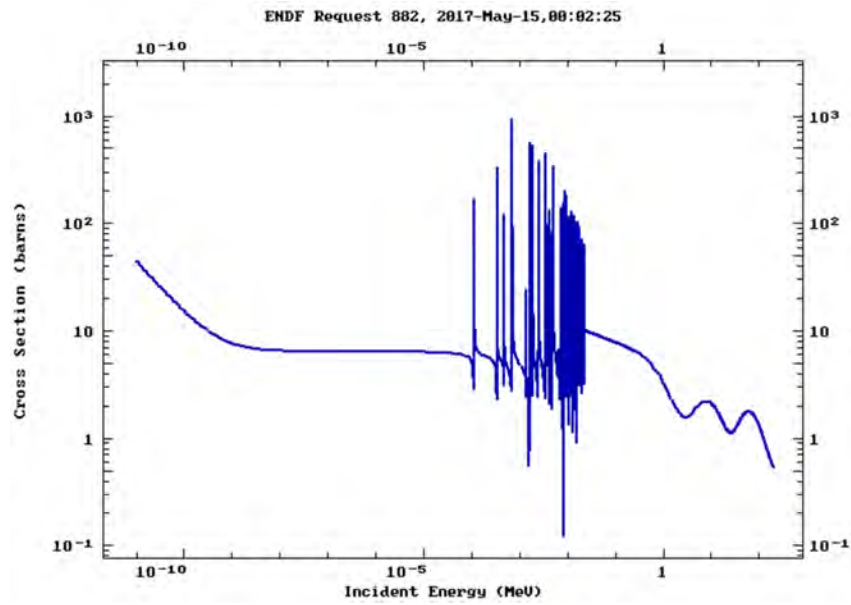

Figure 5.10. Elastic Cross Section for Ga-69 vs. Incoming Neutron Energy. Source: [23].
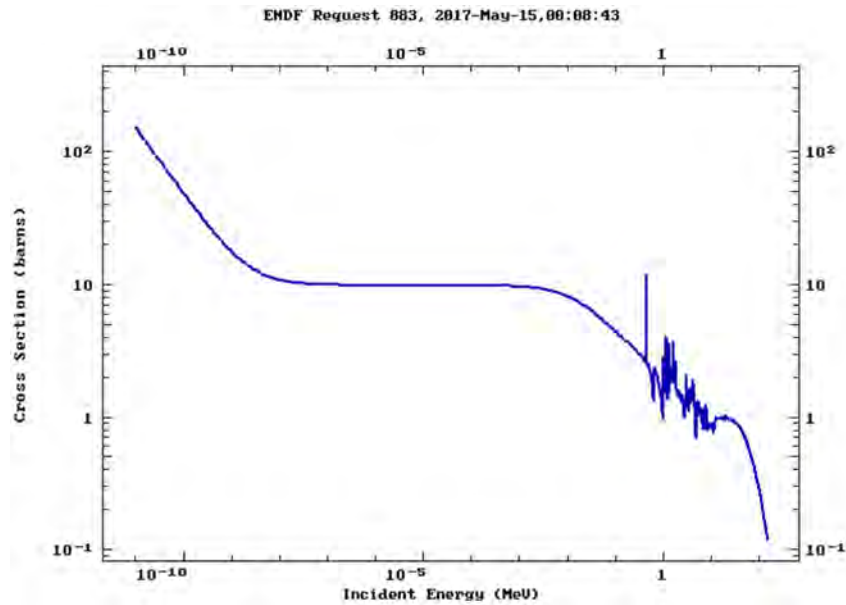

Figure 5.11. Elastic Cross Section for N-14 vs. Incoming Neutron Energy. Source: [23].

The next piece of information received is the minimum displacement energy for the material in each layer. The displacement energy for the Au, Ni, Al, Ga, N, Si, and Ti are given in Table 5.1 [45].

Table 5.1. List of Elemental Displacement Energies

Element	E_d
Al	72
Au	25
Ni	25
N	34
Ga	72
Ti	25
Si	15

The displacement energies are given in units of eV.

The displacement cross section for each energy bin of the neutron spectrum is calculated using the simplified version of Equation (2.16) from Chapter 2. The equation is used with the known elastic cross sections for gallium and nitrogen, the displacement energy, and the energy spectrum of the incoming neutrons. The displacement cross section is expressed as [4]

$$\sigma_D(E_i) \approx \frac{\sigma_S(E_i)}{\gamma E_i} \int_{E_d}^{\gamma E_i} \nu(T) dT, \tag{5.2}$$

where σ_S is the elastic cross section, E_i is the incoming-particle energy, E_d is the displacement energy for the specific atom, $\gamma = 4A/(1 + A)^2$, A is the atomic mass of the displaced atom, and $\nu(T)$ is the number of displacements given the energy of the PKA. The number of displacement per PKA can be simplified by following the Kinchin and Pease model if the Born-Mayer model is used to describe the neutron interactions [4]. This assumption allows us to use the Born-Mayer model and the Kinchin and Pease model to simplify the equation for displacement cross section $\sigma_D(E_i)$ down to

$$\sigma_D(E_i) = \frac{\sigma_S(E_i)}{\gamma E_i} \left(\int_{E_d}^{2E_d} 1 dT + \int_{2E_d}^{E_c} \frac{2T}{E_d} dT + \int_{E_c}^{\gamma E_i} \frac{E_c}{2E_d} dT \right), \tag{5.3}$$

92

where T is the energy transferred to the PKA after the initial displacement, and E_c is the cut-off energy where higher energy particles will cause a constant number of displacement. This equation can be further simplified by evaluating the integrals which gives

$$\sigma_D(E_i) = \frac{\sigma_S(E_i)\gamma E_i}{4E_d}.$$ (5.4)

We can make a reasonably good calculation for the displacement cross sections of the materials within the GaN-on-Si HEMTs using this simplified equation. The displacement cross section vs incoming-particle energy for gallium is illustrated in Figure 5.12, while this relationship for nitrogen is shown in Figure 5.13.
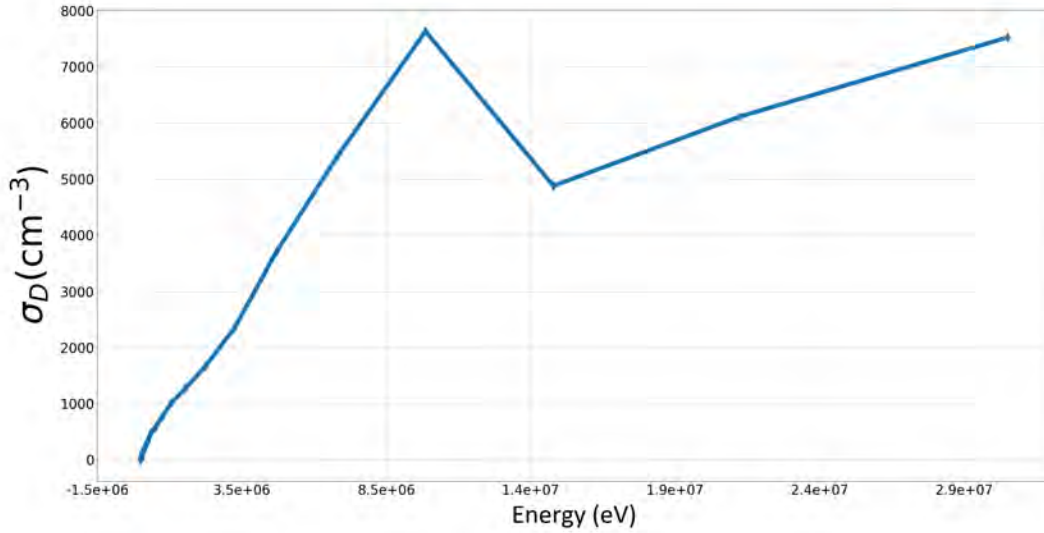
Figure 5.12. Displacement Cross Section for Ga-69 vs. Incoming Neutron Energy
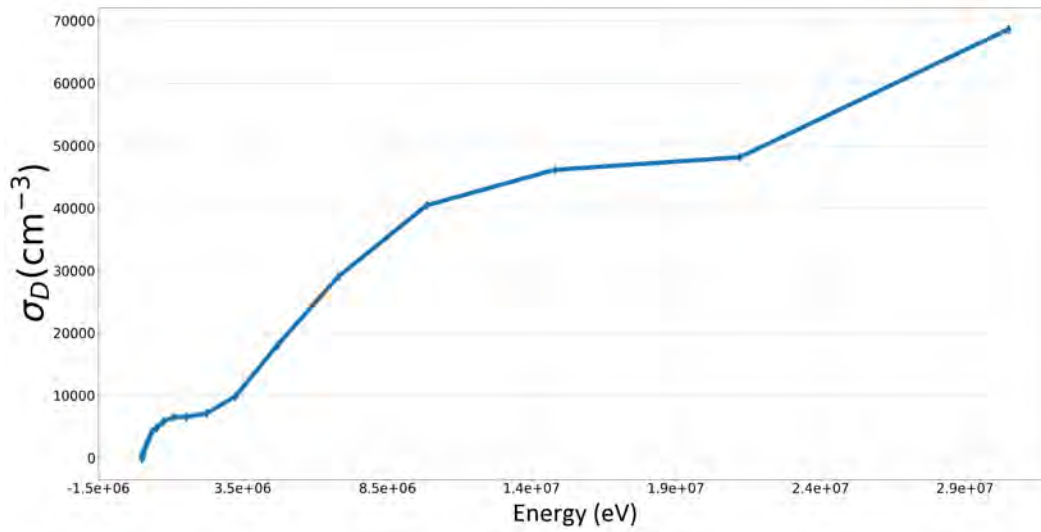
Figure 5.13. Displacement Cross Section for N-14 vs. Incoming Neutron Energy

It is important to note that many elements have isotopes that are stable and naturally occur within the material. These isotopes have different elastic cross sections than their counterpart isotope so it important to take into account any isotopes that have a naturally occurring abundance in the material. In the case of GaN, Ga-69 is about 60 percent of the naturally occurring Ga while Ga-71 makes up the other 40 percent. A single gallium elastic cross section spectrum can be achieved by taking the elastic cross sections of both of these isotopes and interpolating between them.

Equation (2.17) is used to calculate the displacement rate per volume of gallium and nitrogen now that the displacement cross sections are calculated for both the gallium and the nitrogen. The two displacement rates are then added weighed by their masses to derive the total displacement rate within GaN for a given neutron flux/energy spectrum. The displacement rate within GaN was calculated to be $5.67 \cdot 10^{13}$ atoms/(cm$^3 \cdot$ s). The total displacements within the GaN can be calculated versus fluence similar to the way the device characteristics were shown in the previous sections of this chapter. The total displacements to fluence relationship with a logarithmic x-axis scale is provided in Figure 5.14. The neutron displacements are shown in comparison with the proton displacements calculated from the experiment done by Koehler with 2 MeV protons to show the difference in displacement damage achieved.
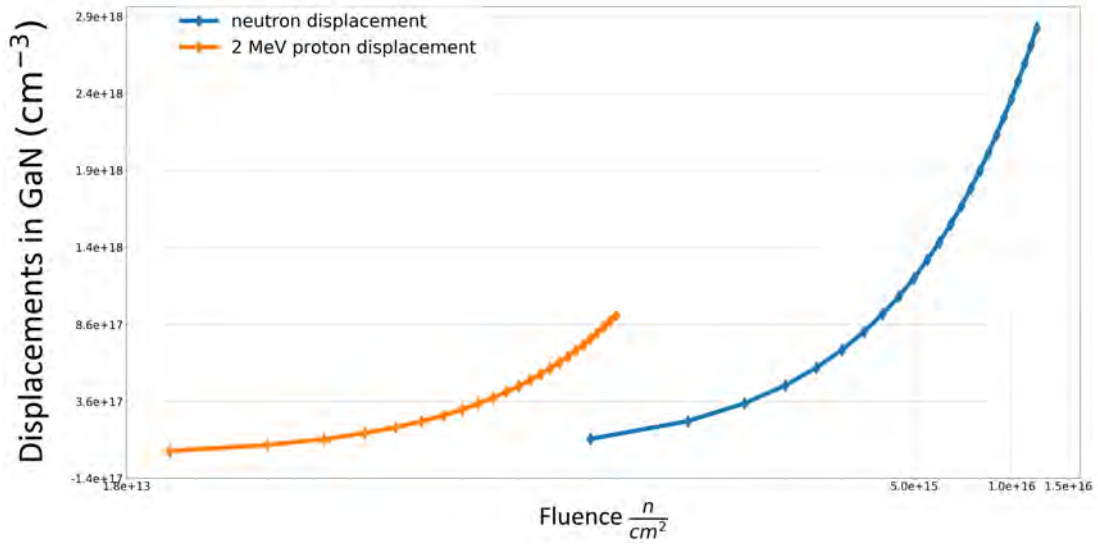
94

Figure 5.14. Total Displacements per Volume of GaN vs. Fluence

The GaN layer received 25 hours of irradiation over the course of the experiment at a flux of around $2 \cdot 10^{11}$ n/(cm$^2 \cdot$ s). The total number of displacements within the GaN layer per cm^3 due to neutrons was $5.1 \cdot 10^{18}$ atoms/(cm^3) when the flux is multiplied by the rate of displacement. The total displacements correlate to about one displacement for every 8,600 atoms within GaN. This displacement ratio is extremely high which accounts for the major changes in the device characteristics. In comparison, the protons have a much higher rate of displacement than neutrons; therefore, in order to achieve the same amount of displacements as the protons, the neutron fluence needed to be 7 times higher. This result demonstrates that a neutron fluence of $4 \cdot 10^{15}$ n/(cm^2) should result in similar device characteristic changes from displacement damage as those obtained with the $6 \cdot 10^{14}$ H/(cm^2) fluence level. The 2 MeV proton experiment showed a 28.9 percent decrease in the mobility at this fluence and a 12.1 percent decrease in 2DEG density as shown in Figure 5.15 [47]. Comparing this to the neutron experimental data at a neutron fluence of $4 \cdot 10^{15}$ n/(cm^2), the neutron experiment found the mobility decreased by 60 percent, while the 2DEG concentration changed by 16 percent.
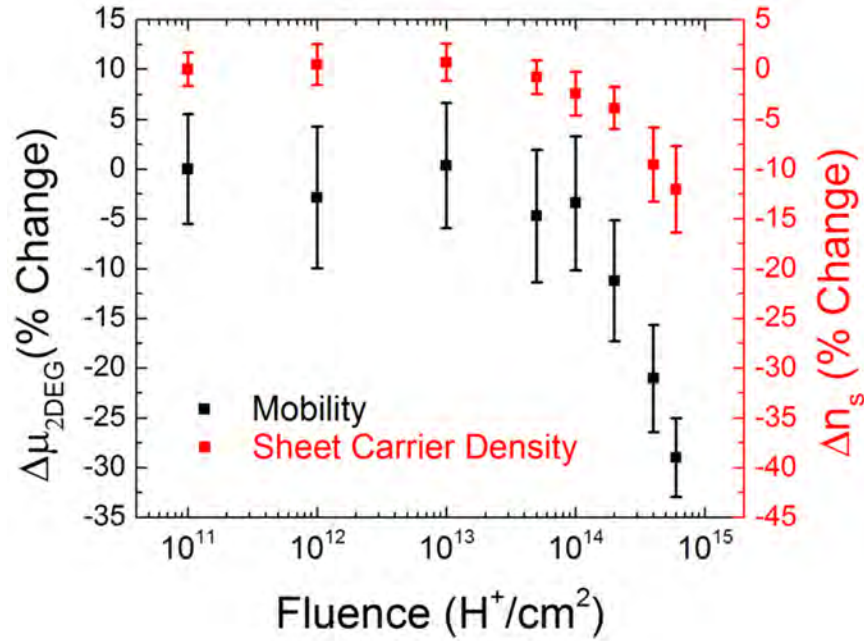
Figure 5.15. Percentage of Change of Mobility and 2DEG Concentration vs.
2 MeV Proton Fluence. Source: [47]

The total displacements per volume for each of the major layers within the GaN-on-Si
HEMT, given the total neutron fluence achieved over the course of this experiment, is
provided in Table 5.2.

Table 5.2. List of Total Displacements per Layer

Layer	Total Displacements per volume
Au	$2 \cdot 10^{18}$
Ni	$5.5 \cdot 10^{18}$
AlGaN	$4.8 \cdot 10^{18}$
GaN	$5.1 \cdot 10^{18}$
Si	$7.1 \cdot 10^{18}$
Ohmic Contact	$5 \cdot 10^{18}$

The total displacements are given in units of atoms/cm^3.

Results show the damage yield for fast neutrons is much higher than for thermal neutrons
even though high energy neutrons have low cross sections for interacting with atomic
structures compared to low energy neutrons. Thermal neutrons may activate materials

more readily, but high energy neutrons provide large numbers of displacements when they collide with the atoms of a material. The displacement values are fairly low at low fluences, but the rate of displacement is high enough so that the number of displacements is two orders of magnitude higher than the number of neutrons hitting the devices. This high magnitude of displacements indicated that there is a large secondary atom recoil effect due to the initial neutron damage, which explains why the shifts in the device characteristics are so high when the device reach fluences above $5 \cdot 10^{15}$ n/cm^2.

The results of the fast-neutron experiment conducted on GaN-on-Si HEMTs showed that the devices incurred neutron damage that caused linear changes in the device parameters at high-fluence levels. At low-fluence levels, the device parameters changed quickly and sometime non-linearly. The conclusions drawn for these results and recommendations for future work needed are discussed in the next chapter.

THIS PAGE INTENTIONALLY LEFT BLANK

CHAPTER 6:
Conclusions

6.1 Experiment Outcomes

The three phases of this experiment were the design and implementation of a high-flux photoneutron converter, the development of an in-situ HEMT measurement system, and the testing and analysis of GaN-on-Si HEMTs and their degradation versus neutron fluence. The photoneutron converter was designed to optimize the bremsstrahlung and photonuclear generation of neutrons in order to maximize the fast neutron flux on the side of the converter. The converter was fabricated to hold a DUT board over the maximum neutron flux point and provide an active cooling system for the tungsten. The photoneutron converter was tested at the Idaho Accelerator Center on the 44-MeV, 2-kW LINAC beamline, and the dosimetry was conducted using the gold/indium foil-activation technique. The cooling system was able to cool the side of the converter down to 70°C, which was cool enough to confidently place packaged parts next to the converter without fear of failure due to the heating of the converter. A neutron flux of $2.2 \cdot 10^{11}$ n/(cm$^2 \cdot$ s) was achieved using the photoneutron converter. Comparing these results to Iobst's neutron experiment, the fast-neutron flux achieved in the TRIGA reactor in UC Davis was about $5 \cdot 10^9$ n/(cm$^2 \cdot$ s). The photoneutron converter obtained a fast-neutron flux that was 40 times larger than that provided by the TRIGA reactor. This flux allowed us to get to an order of magnitude larger neutron fluence than what was achieved in Iobst's experiment in a similar amount of time. The extra high fluence data from this experiment allows us to further understand how GaN-on-Si HEMTs degrade in fast neutron environments.

The design of the in-situ testing system was critical toward the success of this experiment due to the numerous difficulties encountered when characterizing irradiated parts. Safety was the number one objective in the experimental system design, while the signal integrity was an important secondary objective. The hardware system was designed around the use of a switch matrix that allowed us to isolate and make 60 different connections between the ten packaged HEMTs in order to provide a safe experimental setup. Using the switch matrix meant that the entire system could be automated and no manual connection changes

were needed. Automation was important due to the fact that once the experiment began, we would not have access to the devices and their connections due to the activation in the LINAC room. The other essential objective was maintaining the signal integrity of the measurement. There was potential for large-noise interferences if the hardware set up was not designed properly since the measurements needed to be done over a distance of about 100 ft. A Kelvin system was utilized to minimize the resistance along the measurement paths. The long wires were also shielded well in order to decrease any noise attempting to infiltrate the measurement system. The system proved to work well in both aspects of design as the automation worked as expected and the pulsed DC measurement was able to operate without any major pulse distortions. Low-pulse distortion allowed for clean and accurate in-situ measurements of the HEMTs during irradiation.

The GaN-on-Si HEMTs were measured with static and dynamic DC measurements that included Id-Vg, Ig-Vg, Vd-Id, Vs-Is, and a dynamic dual-pulsed I-V sweep. The parameters extracted from these measurements were threshold voltage, 2DEG concentration, subthreshold slope, active-region mobility, gate leakage, source access resistance, drain access resistance, and dynamic on-state resistance. It was discovered that the dynamic $R_{DS,on}$ parameter was the most sensitive to irradiation with a 150 percent shift over the course of the experiment. Every parameter had a linear relationship versus fluence at high-fluence levels. The parameters actually changed faster early in the irradiation than at larger fluences later in the experiment, but several of the parameters, including gate leakage, actually improved at the low fluences. There was a behavior shift in the devices when the neutron fluence reached a level above $3 \cdot 10^{15}$ n/cm^2. Displacement calculations were conducted for each of the major layers within the GaN-on-Si HEMTs, and these results showed a linear relationship to fluence which provides further evidence towards our hypothesis that fast-neutron displacement is the cause of the linear parameter change at high-fluence levels. The GaN layer had $5.1 \cdot 10^{18}$ atoms/cm^3 of total displacements per cm^3, which means there is a displaced atom for every 8,600 atoms within the material. When compared to the 2-MeV proton experiment, the displacement rate of the protons on GaN is seven times greater than that of neutrons in GaN. The percentage changed by the 2DEG concentration was almost identical at the same displacement level for neutron and proton irradiation. The mobility dropped 60 percent when irradiated with neutrons instead of the 21.9 percent decrease from the protons. These results revealed that the device is overwhelmed by the large number of

secondary displacements occurring per incoming neutron and quickly degrades due to a collapse in current and a decrease in 2DEG concentration.

6.2   Future Work

Further research is underway at NPS to fully characterize the energy-trap states of the GaN-on-Si HEMTs using an analog DLOS/DLTS system. This work will use optics and temperature to probe different energy levels within these devices in order to find the energy levels of the various inherent traps and their density within the semiconductor. The photoneutron converter created in this work will be utilized to irradiate the DLOS characterized HEMTs and measure how the physical trap states within these device change due to fast-neutron damage. These measurements all provide further insight into the state of the device following high-fluence fast-neutron irradiation.

THIS PAGE INTENTIONALLY LEFT BLANK

APPENDIX A:
Other Device Data

While only one device was discussed in Chapter 5, seven other devices were irradiated and tested before, during, and after the experiment. The scope of data obtained varies for each device because the devices failed at different point of the experiment. Some failed early on, while others survived the testing. This appendix provides the rest of the data for each of the remaining devices.
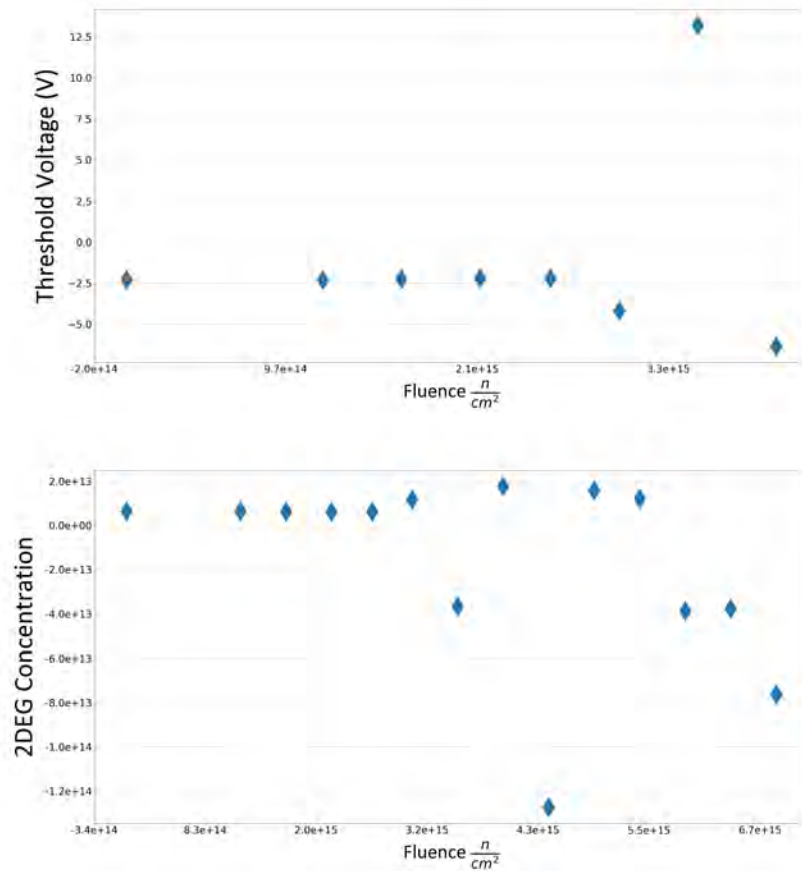
Figure A.1. Device 1 Threshold Voltage vs Fluence (top) and 2DEG Concentration vs Fluence (bottom)
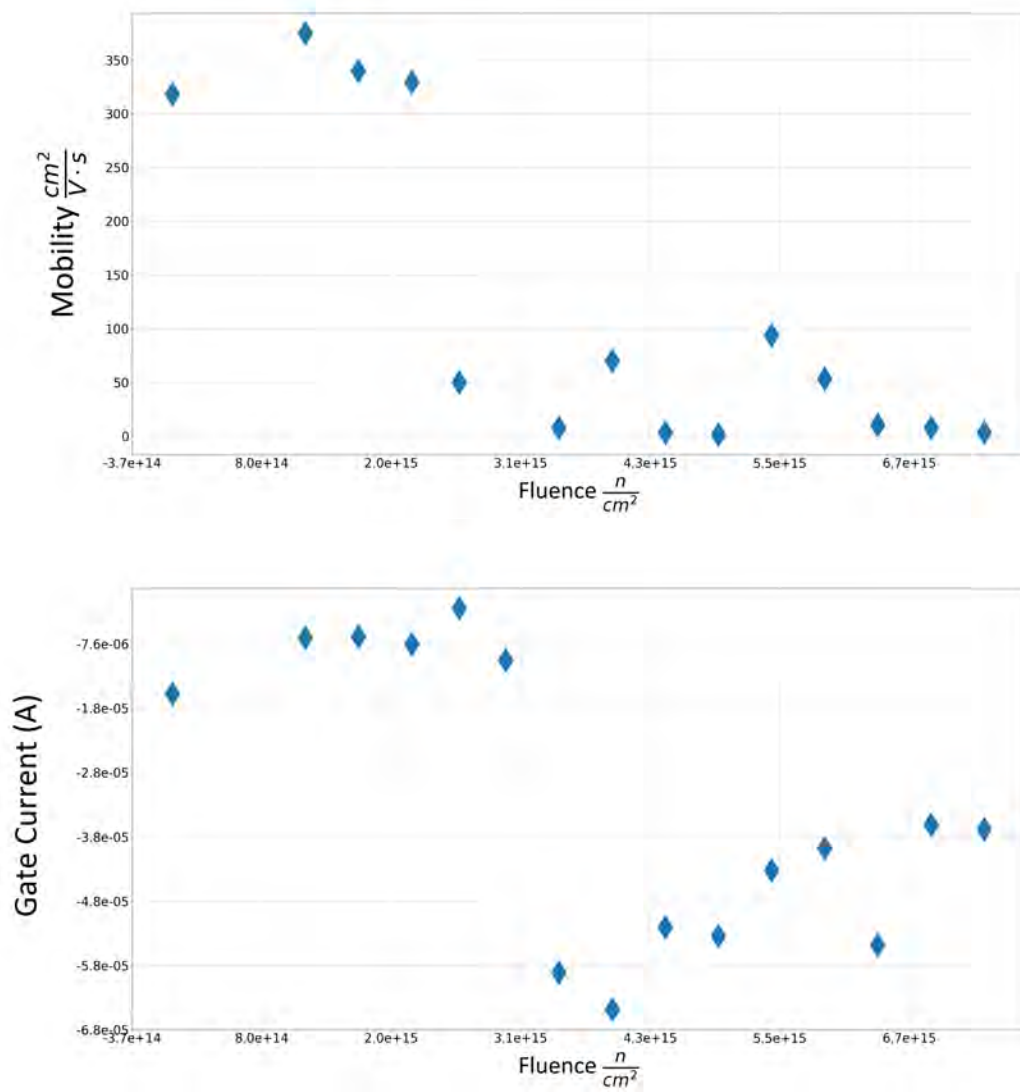
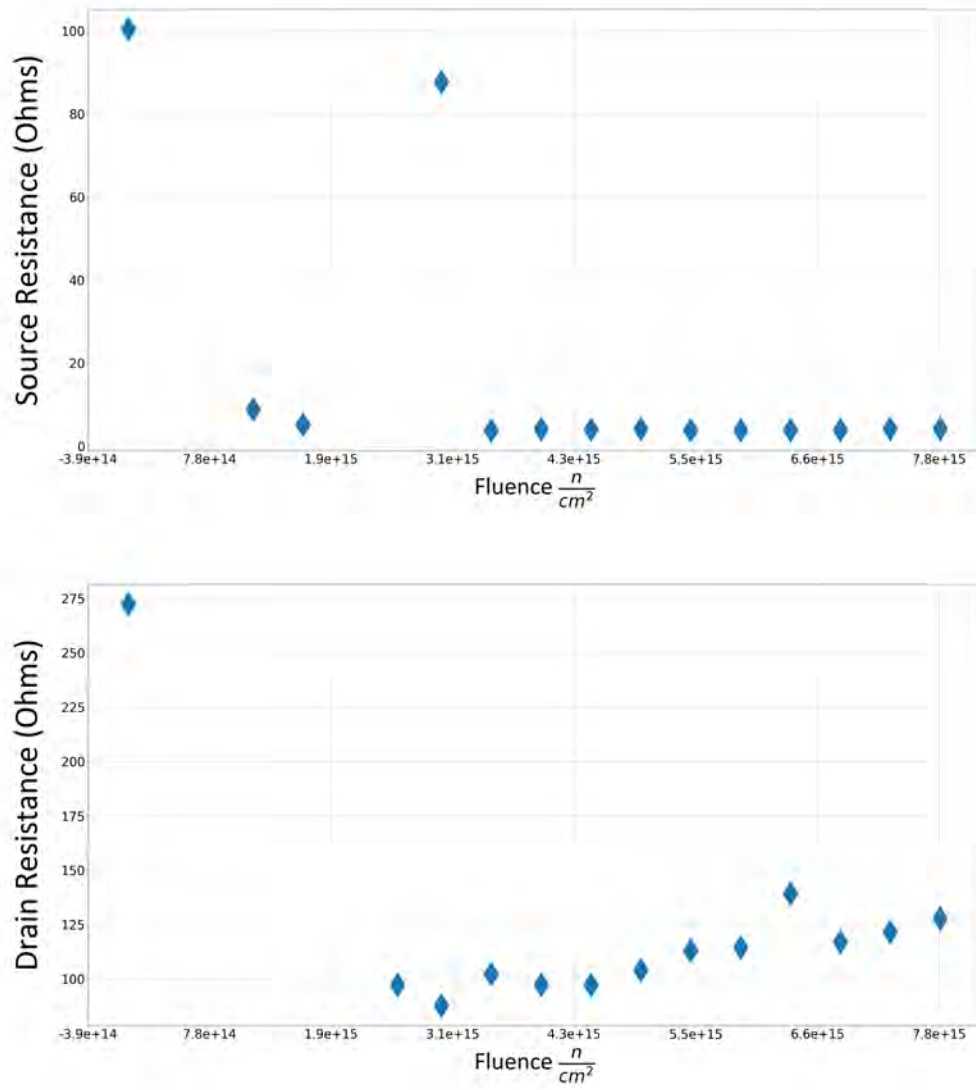Figure A.2. Device 1 Mobility vs Fluence (top) and Gate Leakage vs Fluence (bottom)
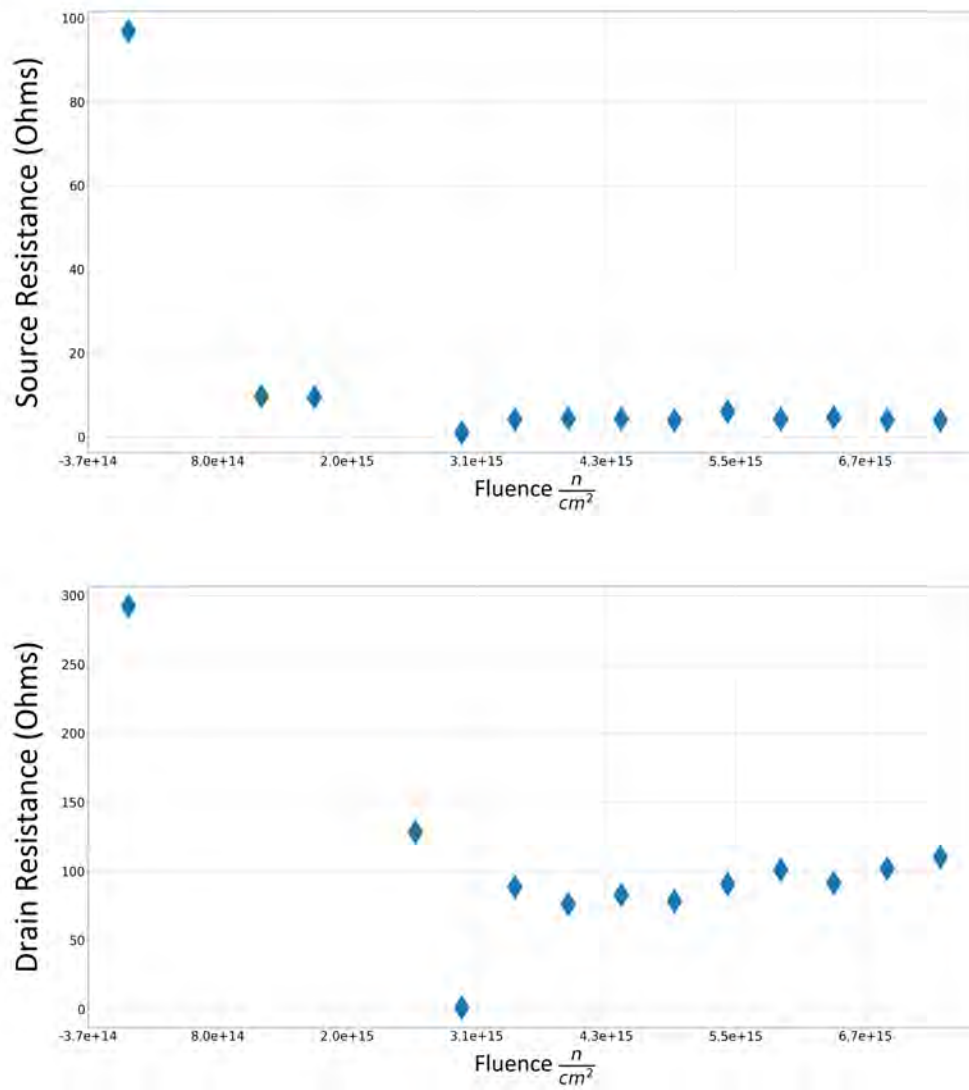
Figure A.3. Device 1 Source Access Resistance vs Fluence (top) and Drain Access Resistance vs Fluence (bottom)
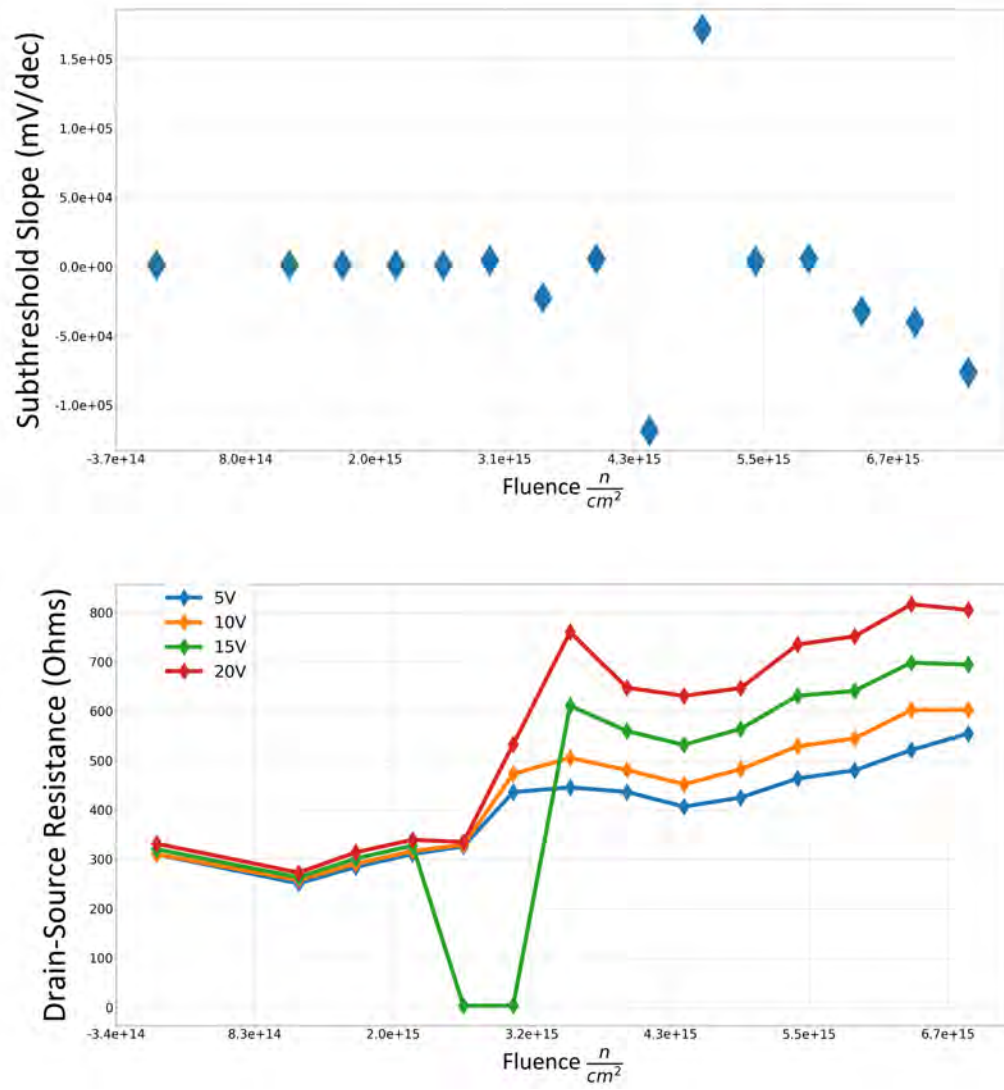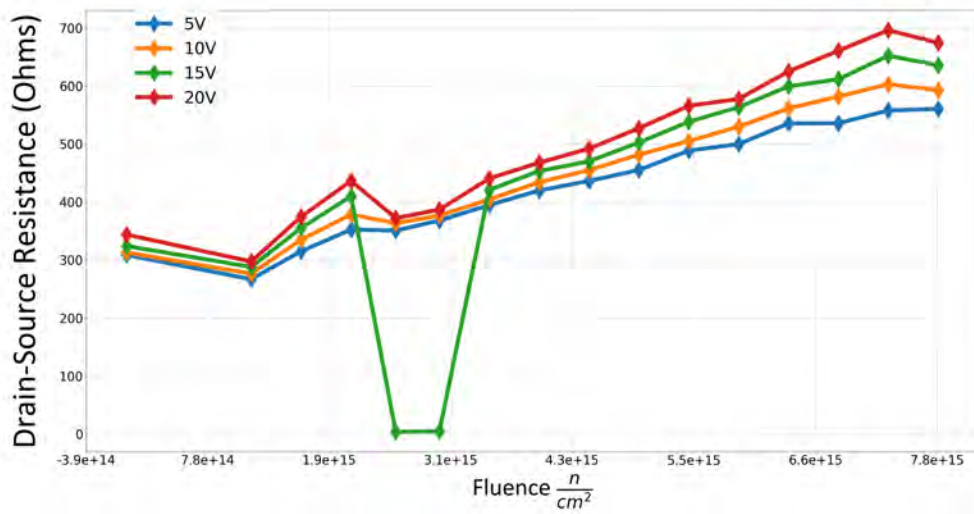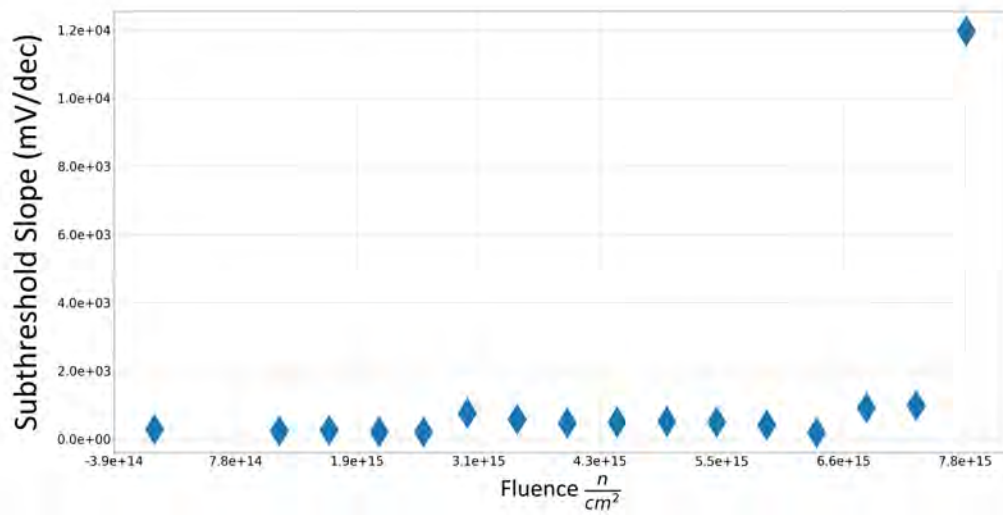
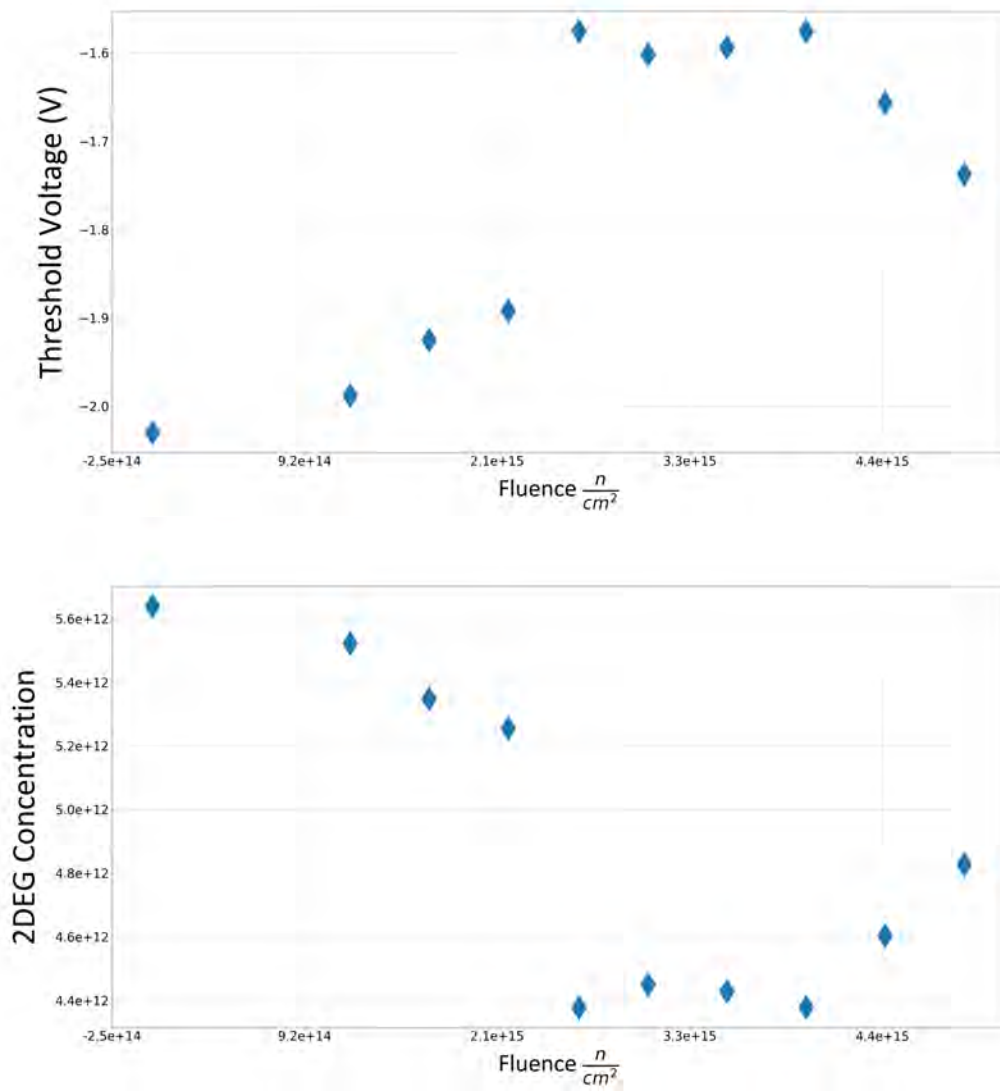Figure A.4. Device 1 Subthreshold Slope vs Fluence (top) and Dynamic On-state Resistance vs Fluence (bottom)
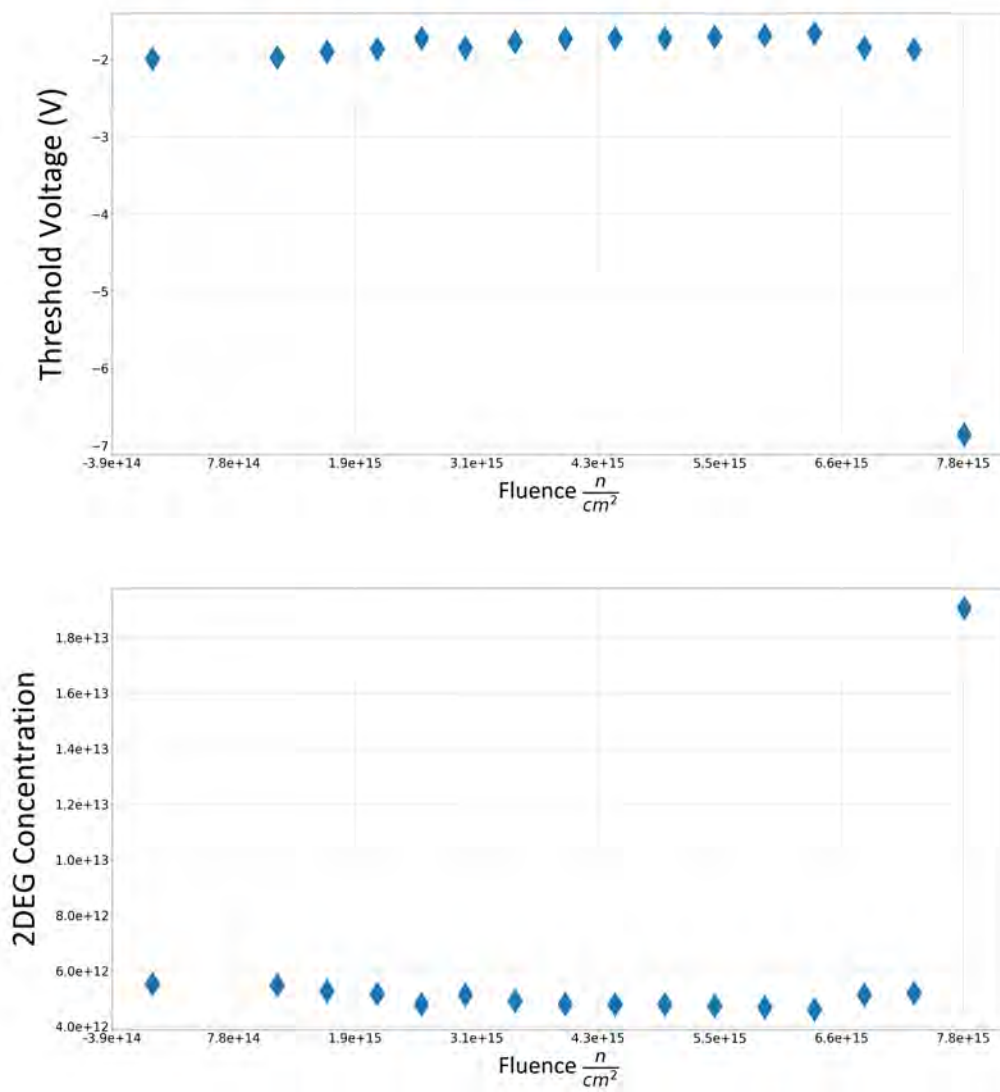
Figure A.5. Device 2 Threshold Voltage vs Fluence (top) and 2DEG Concentration vs Fluence (bottom)
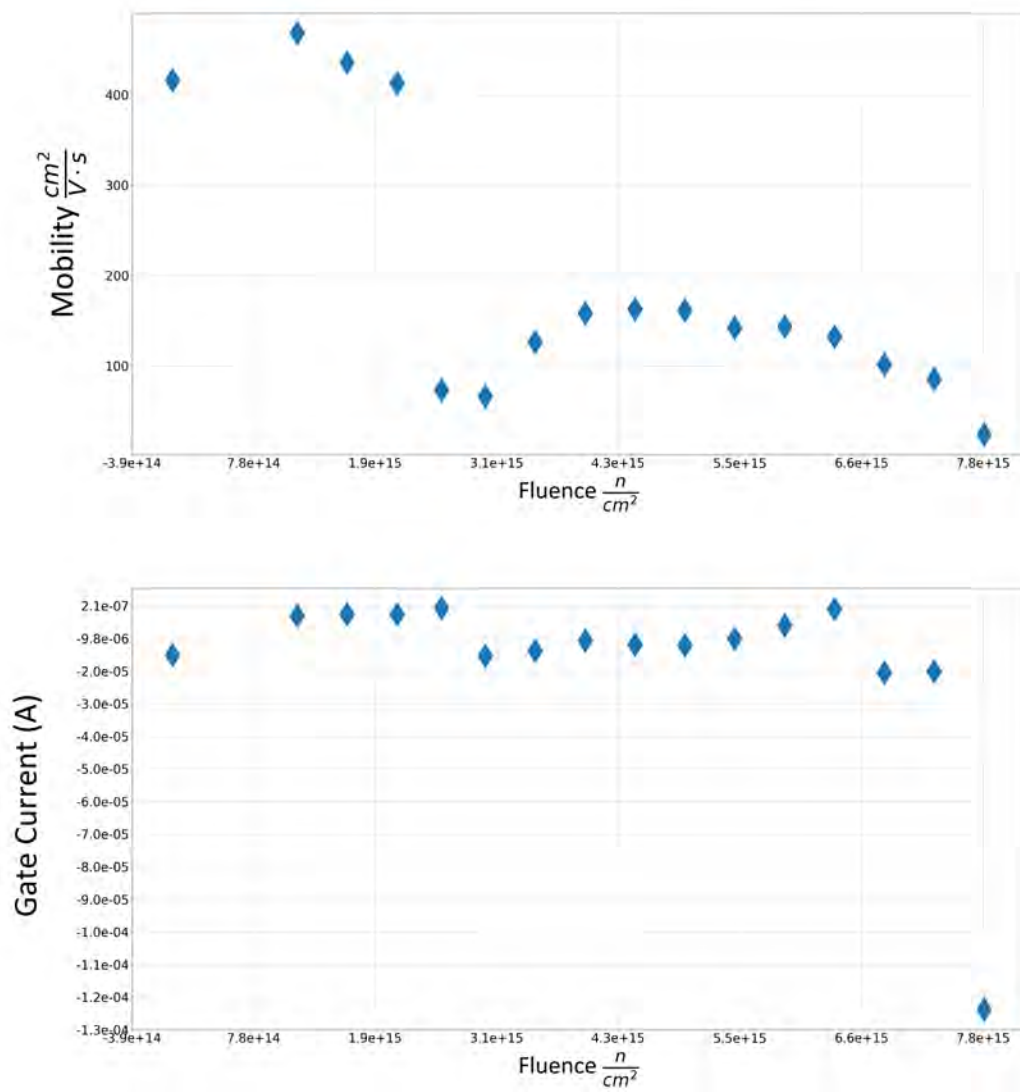
Figure A.6. Device 2 Mobility vs Fluence (top) and Gate Leakage vs Fluence (bottom)

Figure A.7. Device 2 Source Access Resistance vs Fluence (top) and Drain Access Resistance vs Fluence (bottom)

Figure A.8. Device 2 Subthreshold Slope vs Fluence (top) and Dynamic On-state Resistance vs Fluence (bottom)

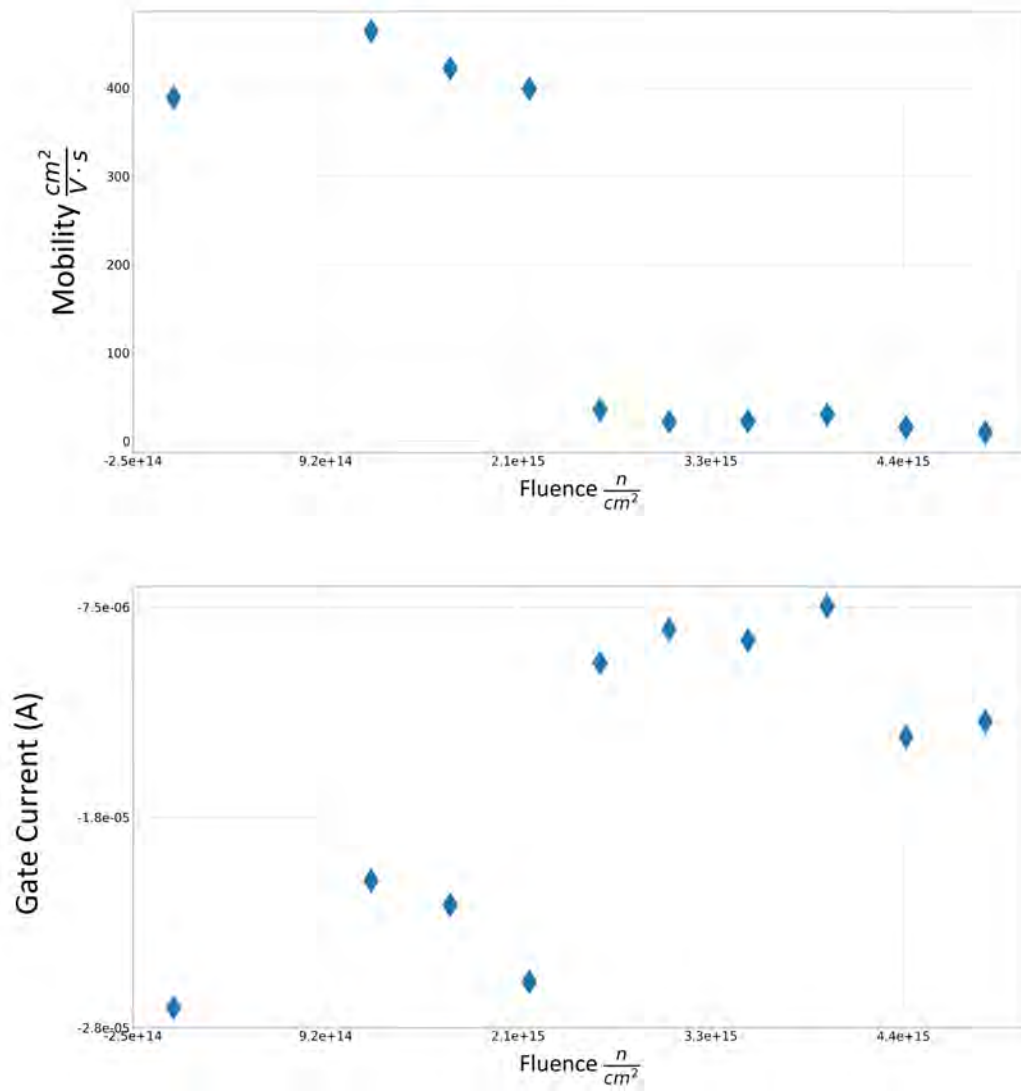Figure A.9. Device 3 Threshold Voltage vs Fluence (top) and 2DEG Concentration vs Fluence (bottom)

111

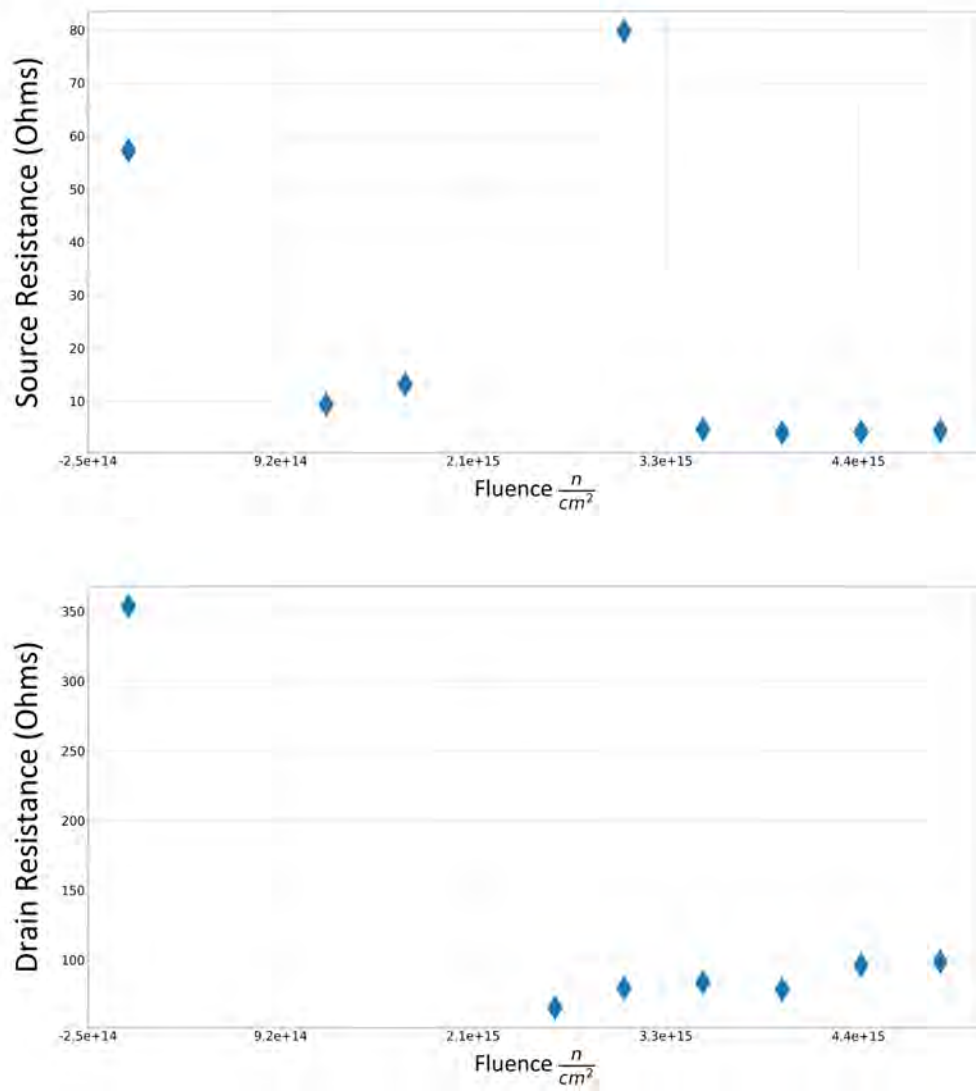Figure A.10. Device 3 Mobility vs Fluence (top) and Gate Leakage vs Fluence (bottom)

112

Figure A.11. Device 3 Source Access Resistance vs Fluence (top) and Drain
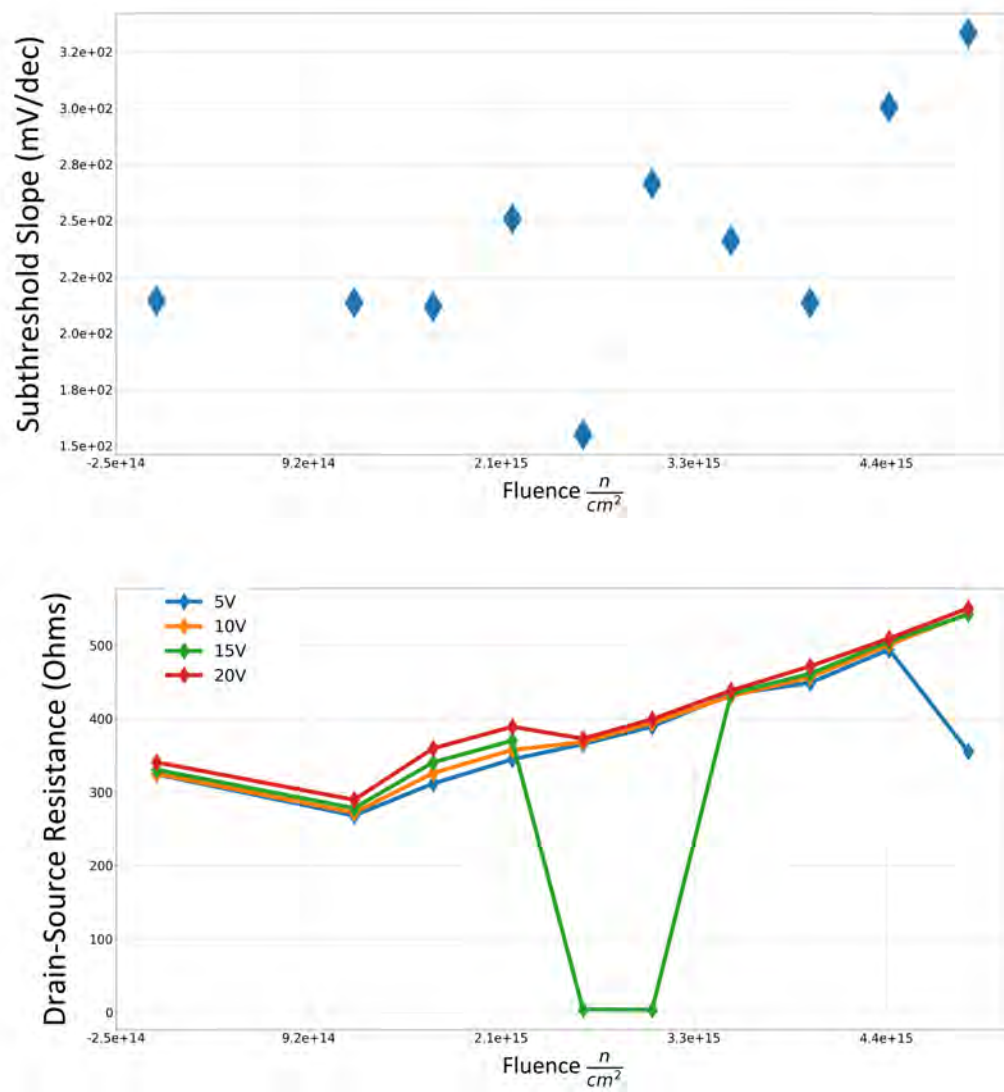Access Resistance vs Fluence (bottom)

Figure A.12. Device 3 Subthreshold Slope vs Fluence (top) and Dynamic On-state Resistance vs Fluence (bottom)
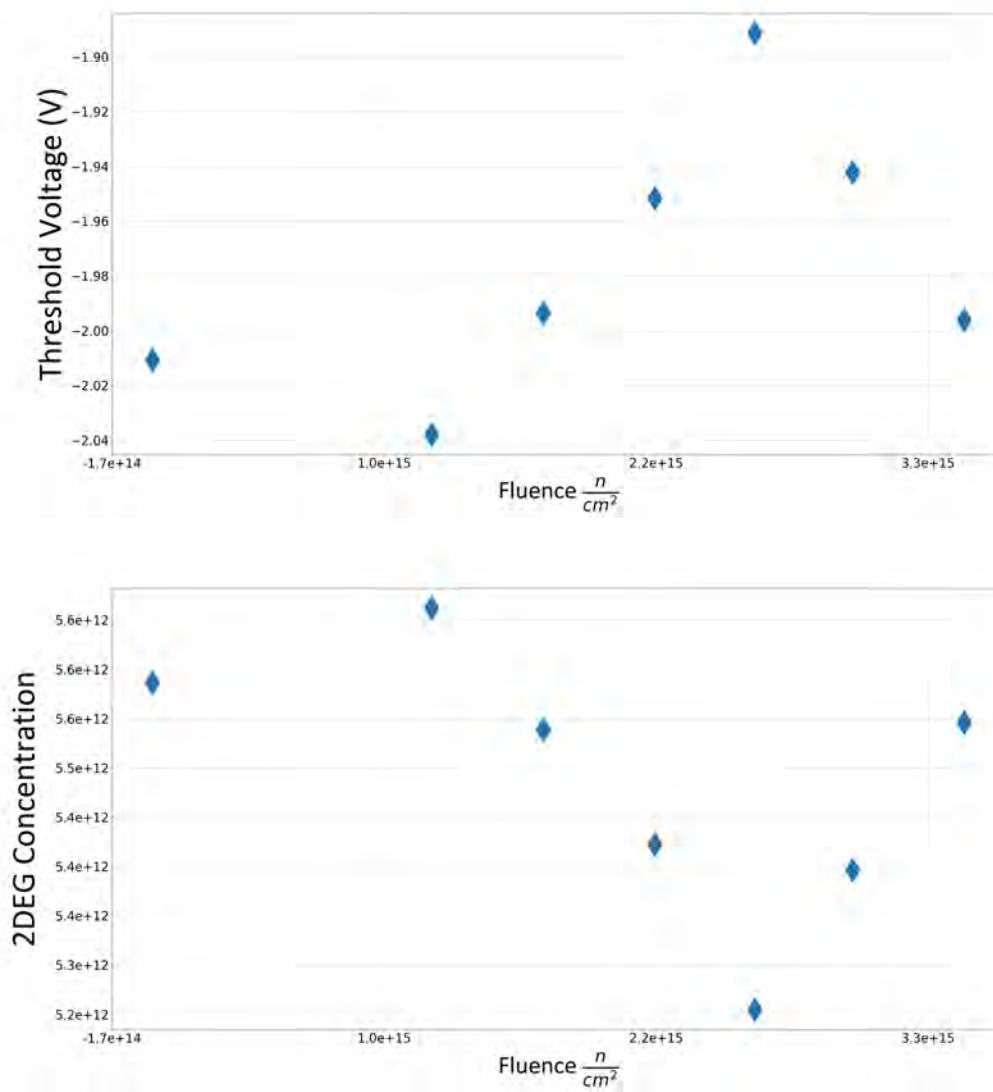
Figure A.13. Device 4 Threshold Voltage vs Fluence (top) and 2DEG Concentration vs Fluence (bottom)

Figure A.14. Device 4 Mobility vs Fluence (top) and Gate Leakage vs Fluence (bottom)

Figure A.15. Device 4 Source Access Resistance vs Fluence (top) and Drain Access Resistance vs Fluence (bottom)

Figure A.16. Device 4 Subthreshold Slope vs Fluence (top) and Dynamic On-state Resistance vs Fluence (bottom)

Figure A.17. Device 5 Threshold Voltage vs Fluence (top) and 2DEG Concentration vs Fluence (bottom)
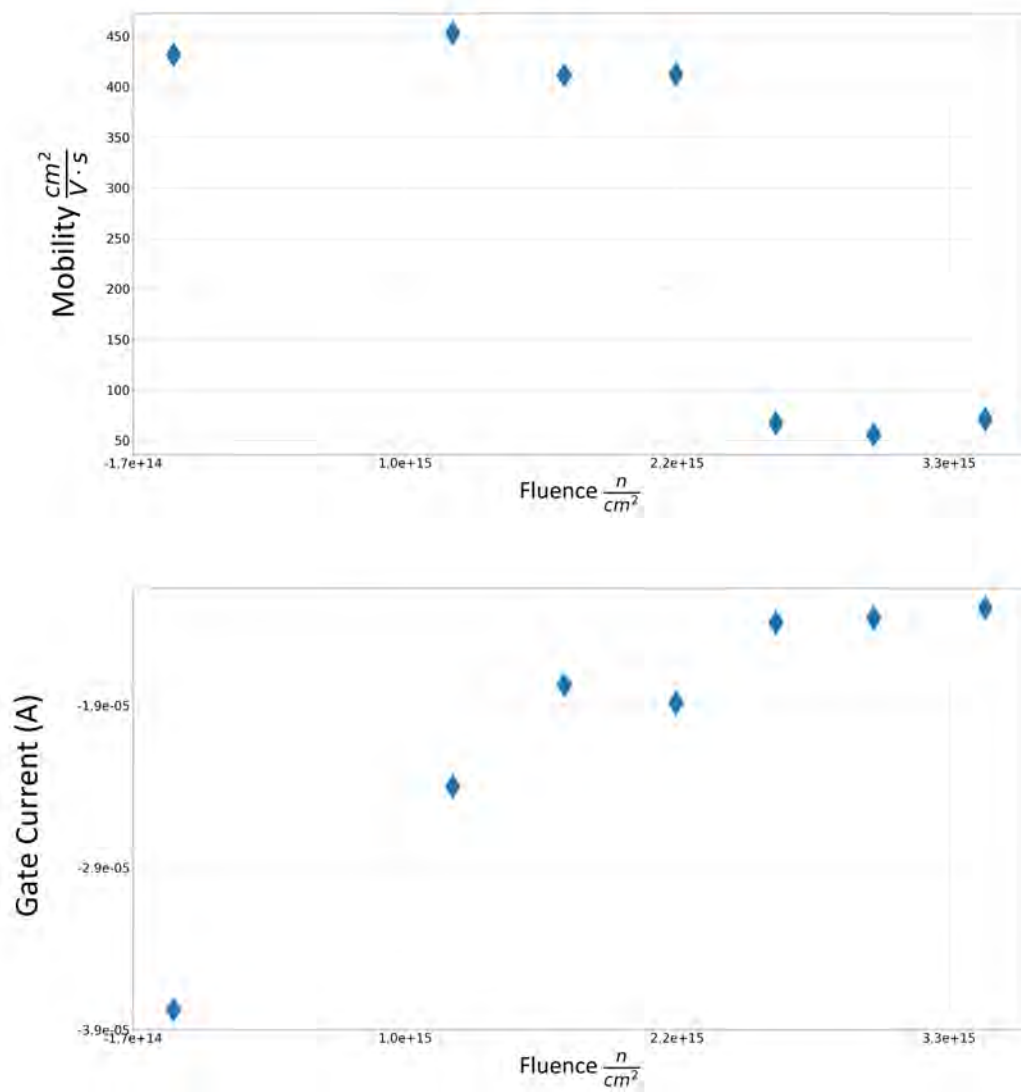
Figure A.18. Device 5 Mobility vs Fluence (top) and Gate Leakage vs Fluence (bottom)
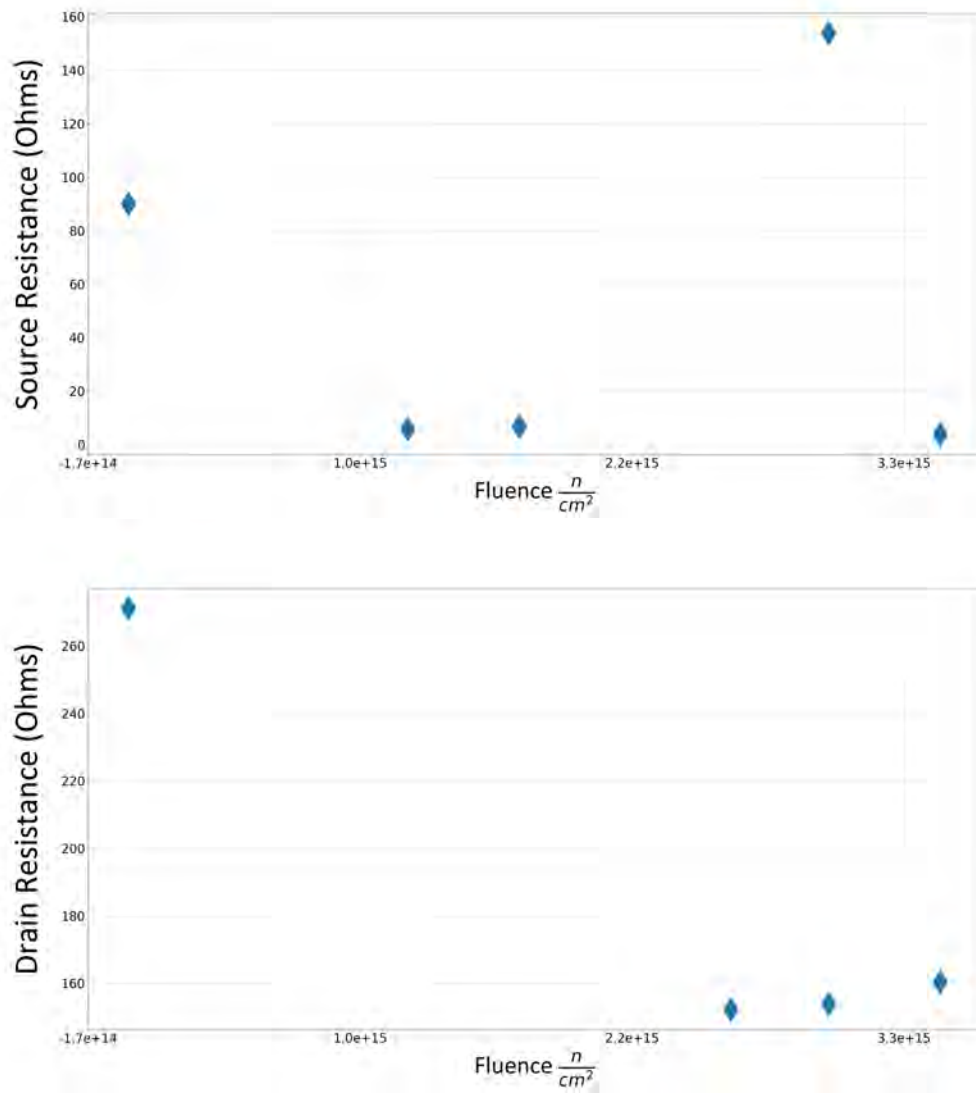
Figure A.19. Device 5 Source Access Resistance vs Fluence (top) and Drain Access Resistance vs Fluence (bottom)

Figure A.20. Device 5 Subthreshold Slope vs Fluence (top) and Dynamic On-state Resistance vs Fluence (bottom)
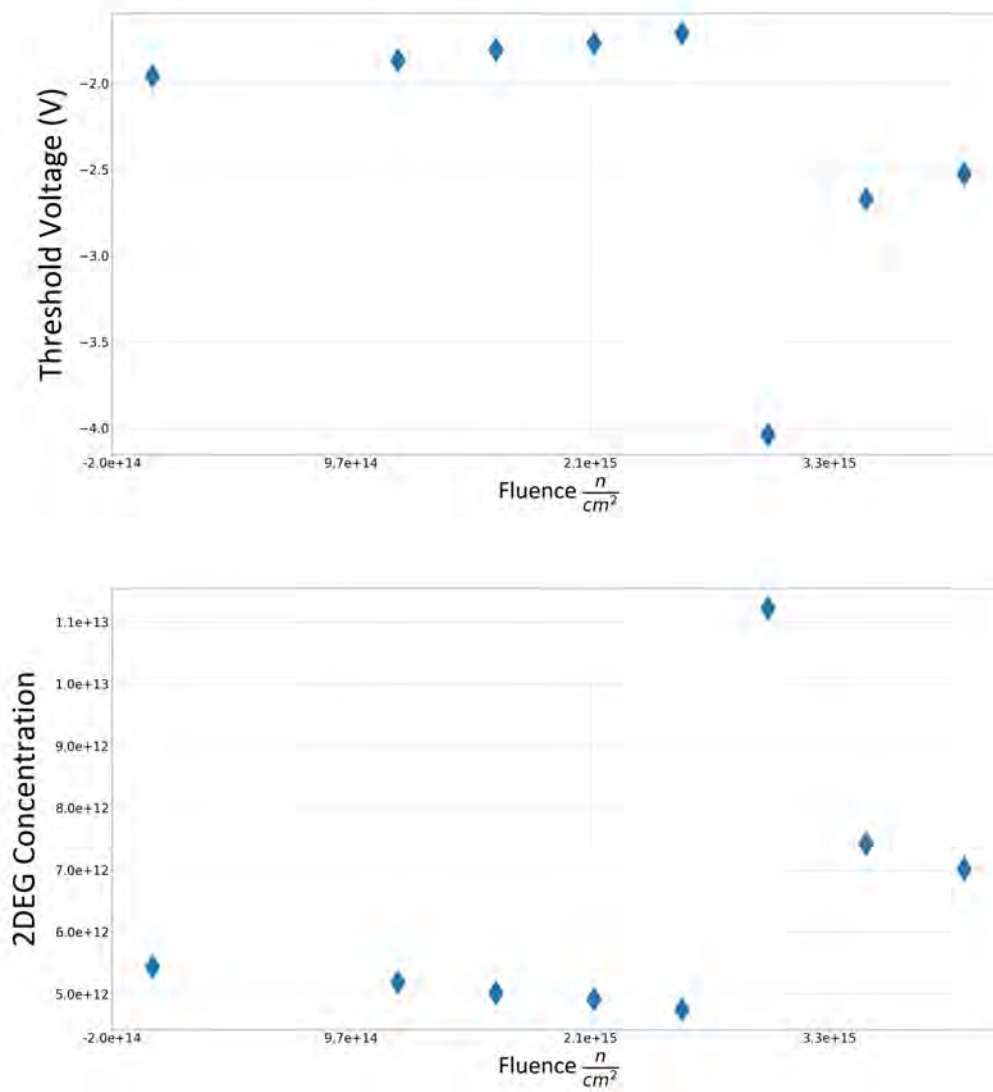
Figure A.21. Device 6 Threshold Voltage vs Fluence (top) and 2DEG Concentration vs Fluence (bottom)
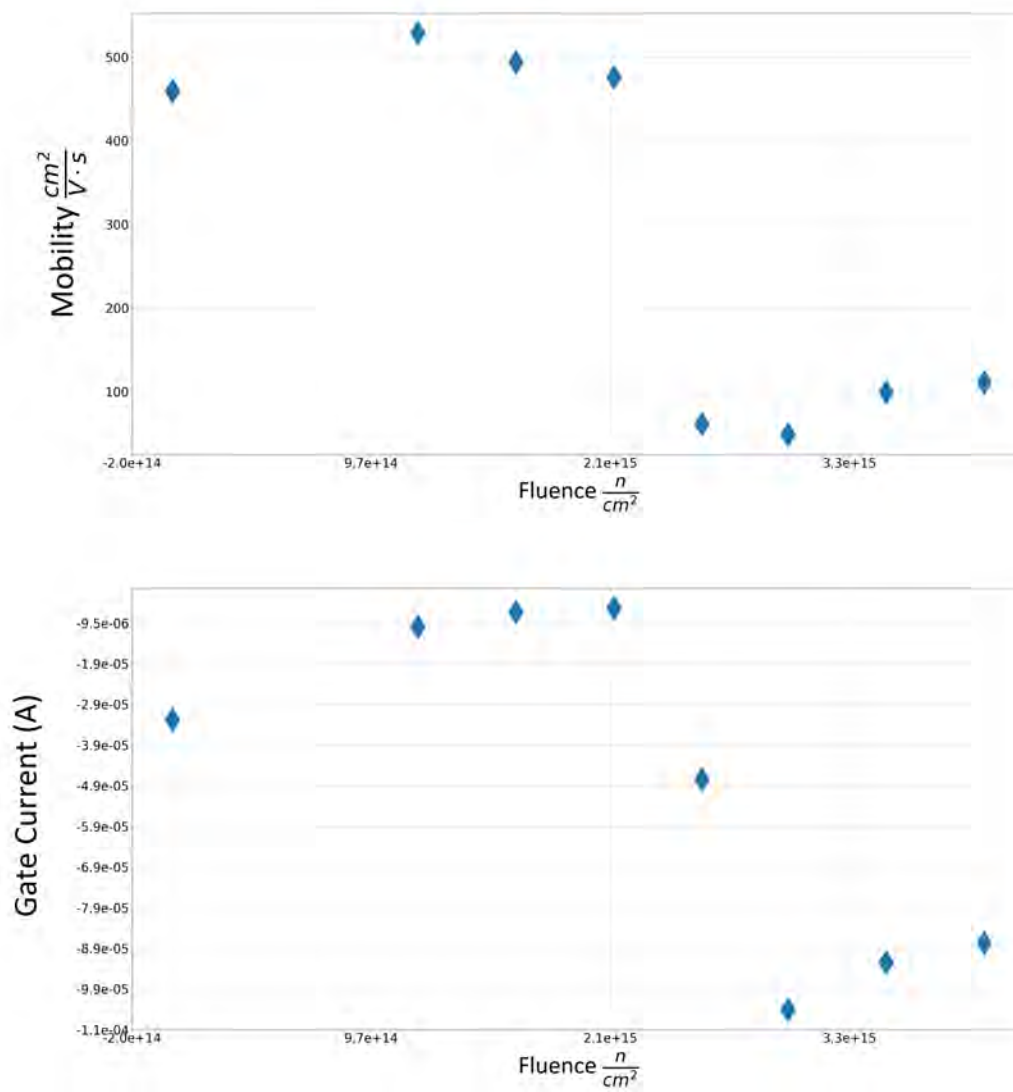
Figure A.22. Device 6 Mobility vs Fluence (top) and Gate Leakage vs Fluence (bottom)
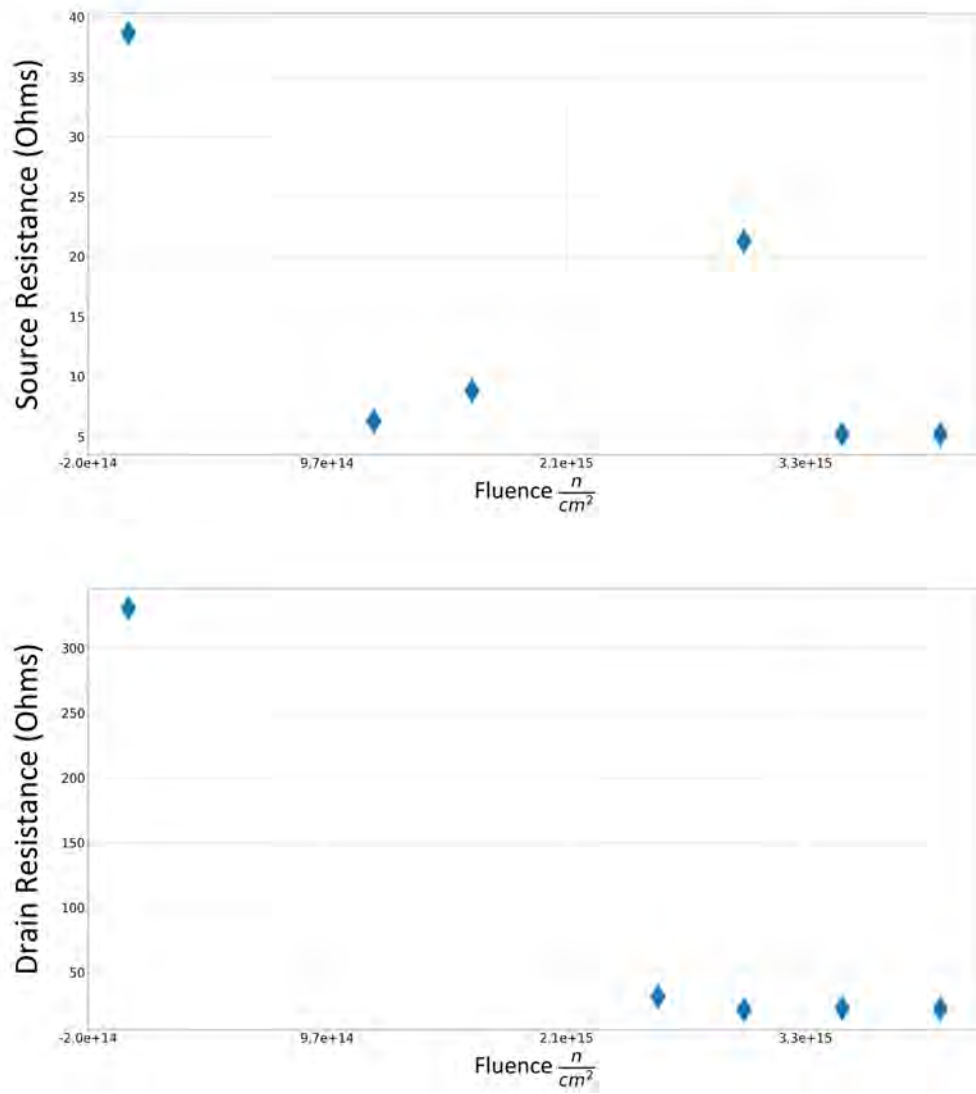
Figure A.23. Device 6 Source Access Resistance vs Fluence (top) and Drain
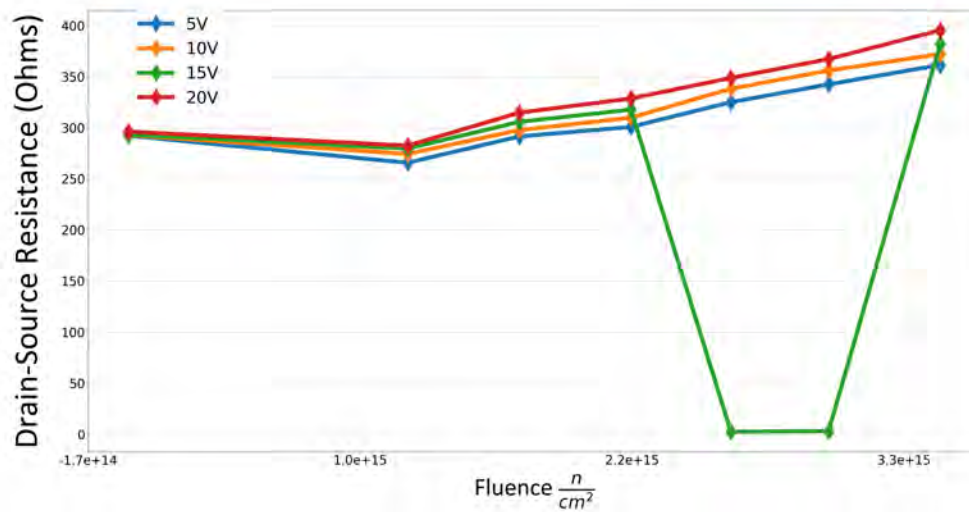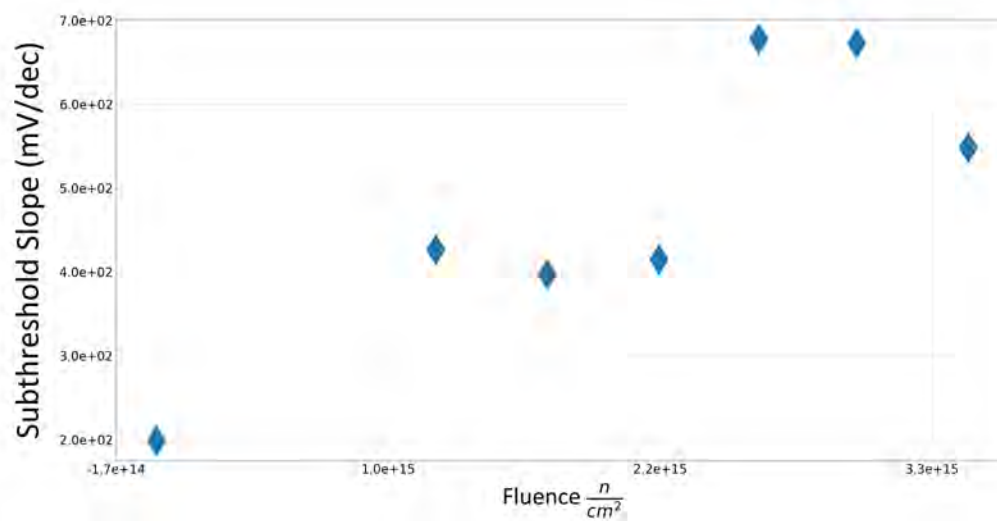Access Resistance vs Fluence (bottom)
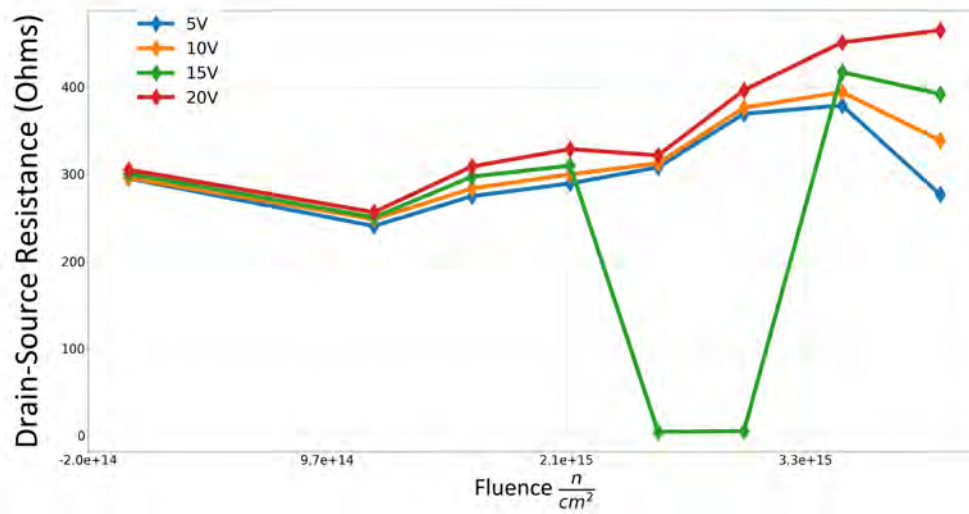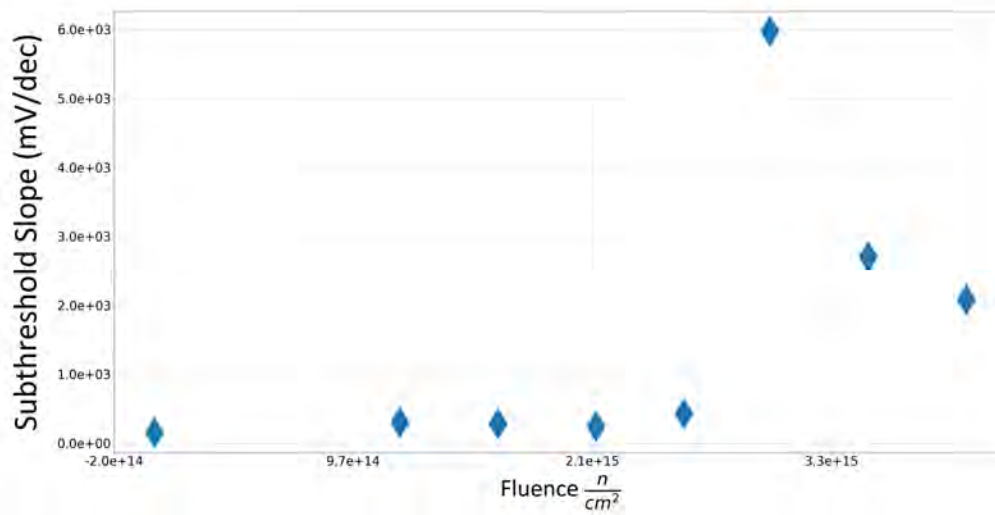
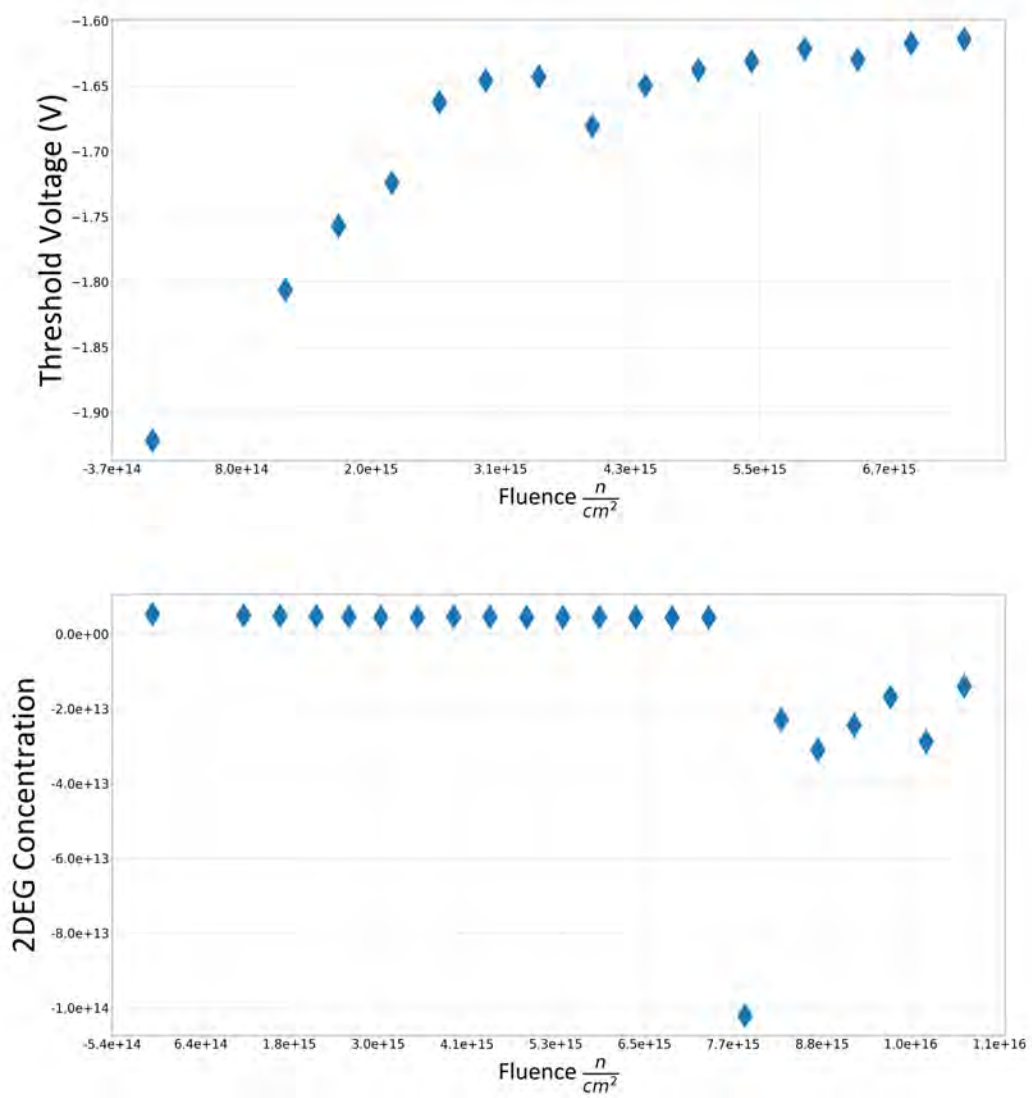Figure A.24. Device 6 Subthreshold Slope vs Fluence (top) and Dynamic On-state Resistance vs Fluence (bottom)
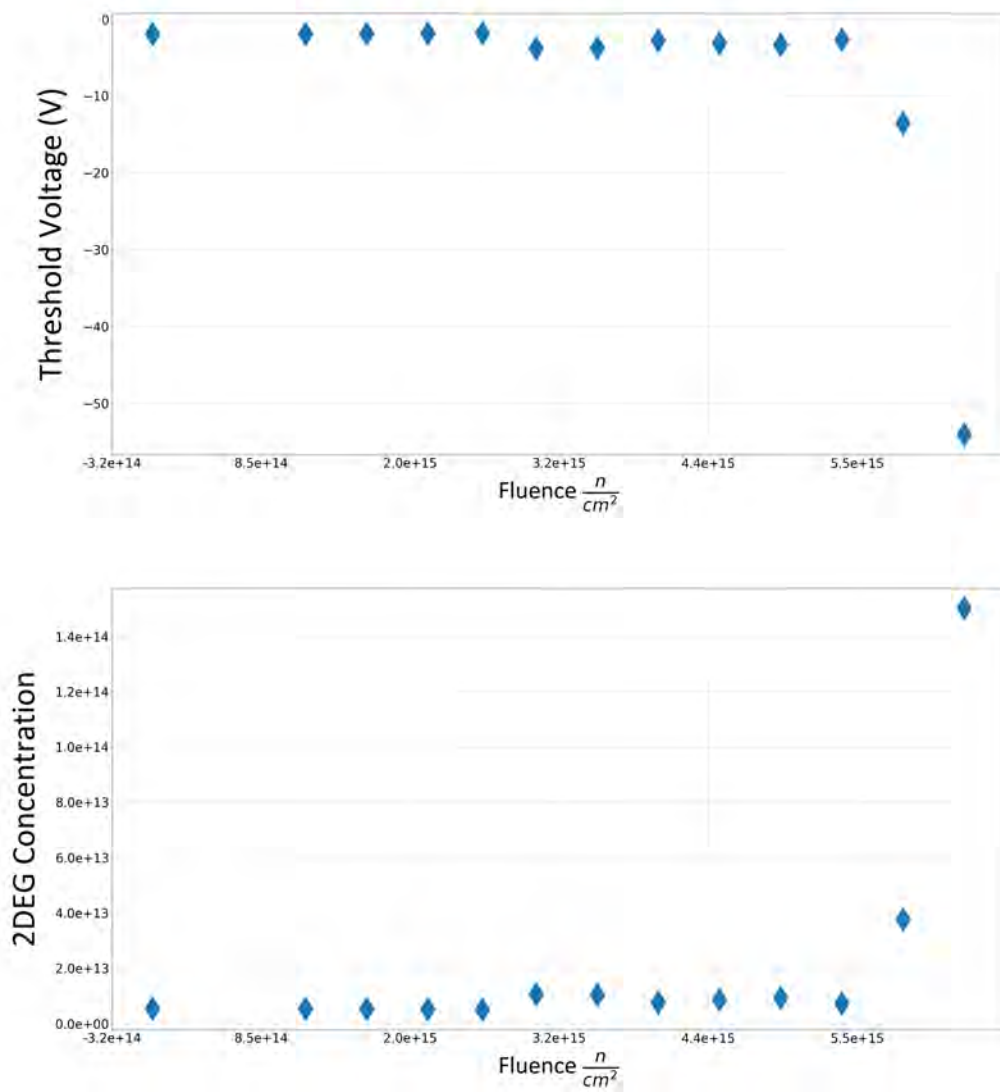
Figure A.25. Device 7 Threshold Voltage vs Fluence (top) and 2DEG Concentration vs Fluence (bottom)
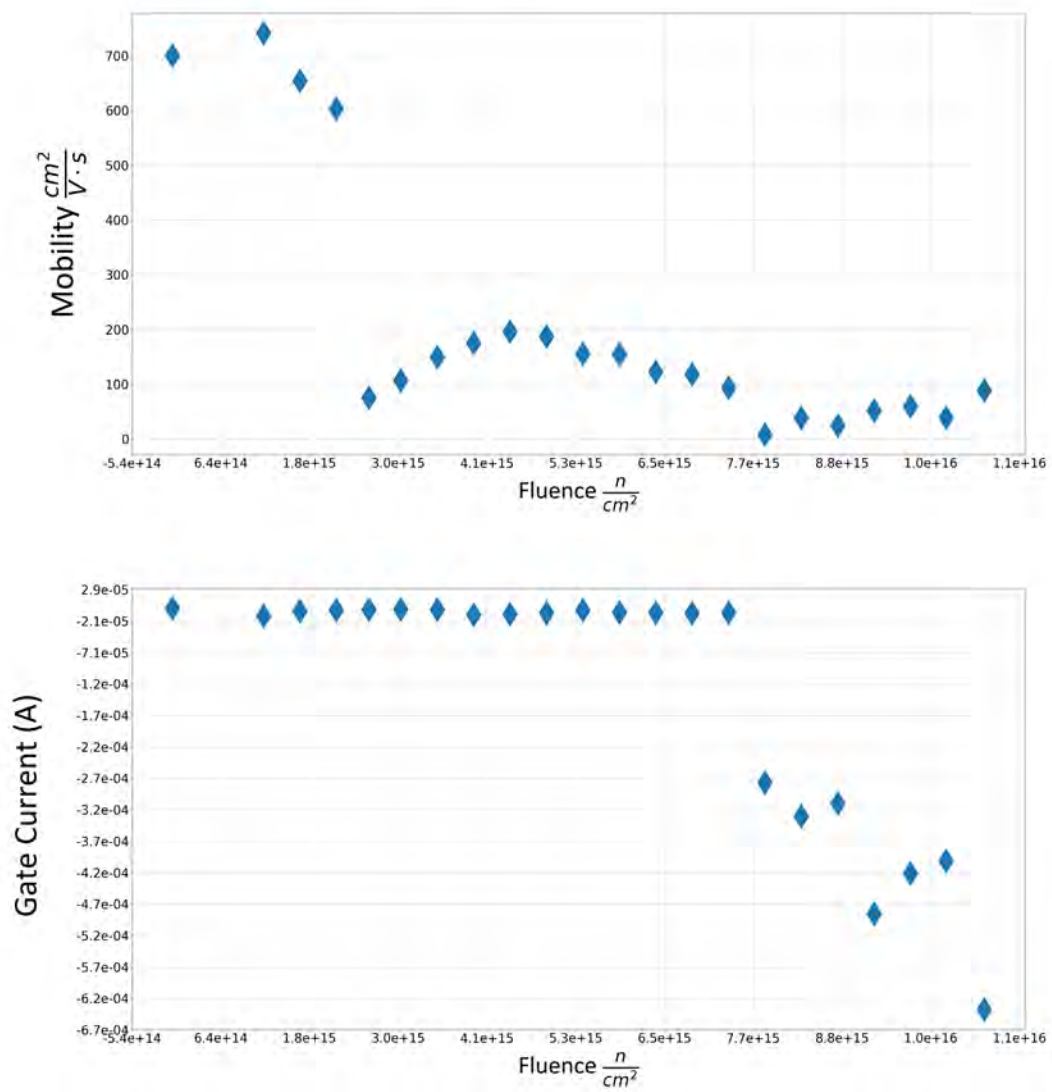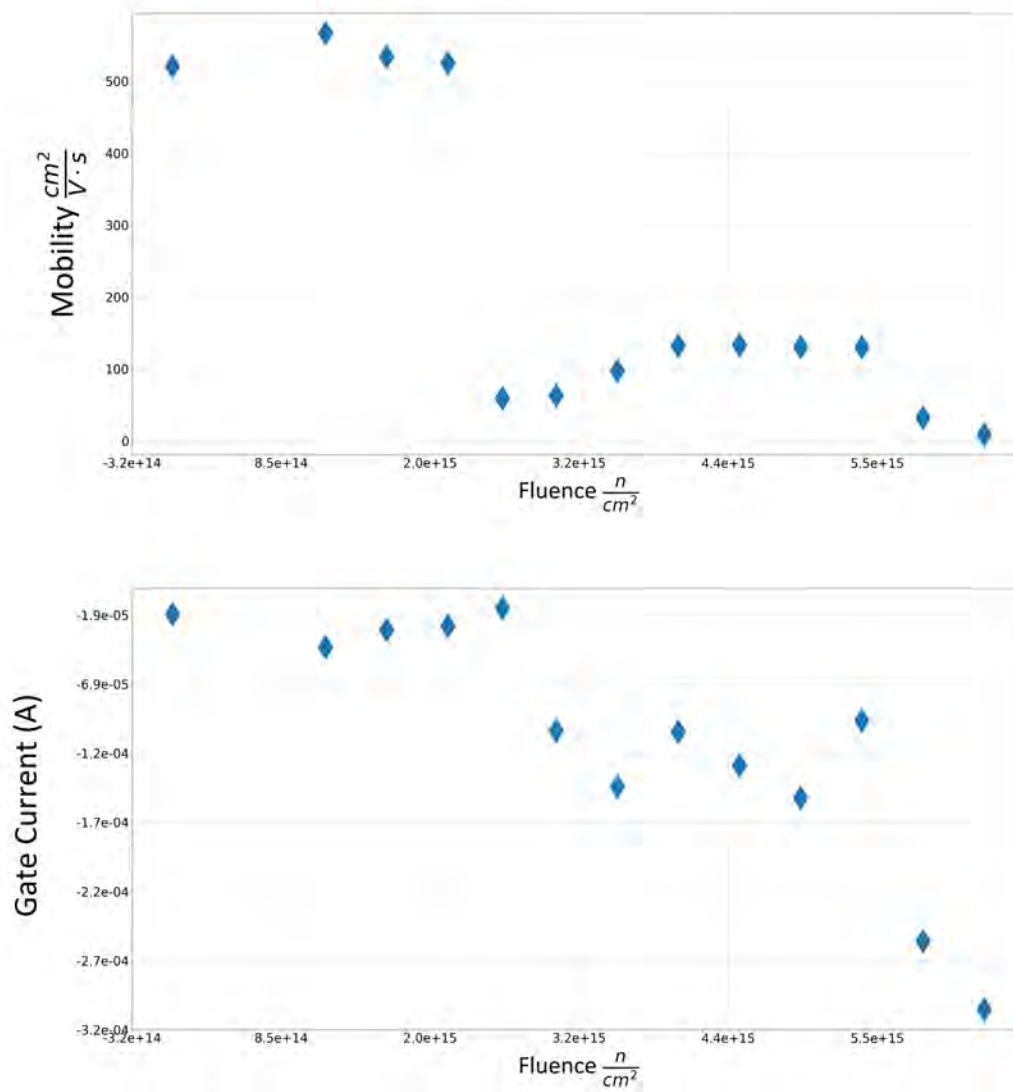
Figure A.26. Device 7 Mobility vs Fluence (top) and Gate Leakage vs Fluence (bottom)
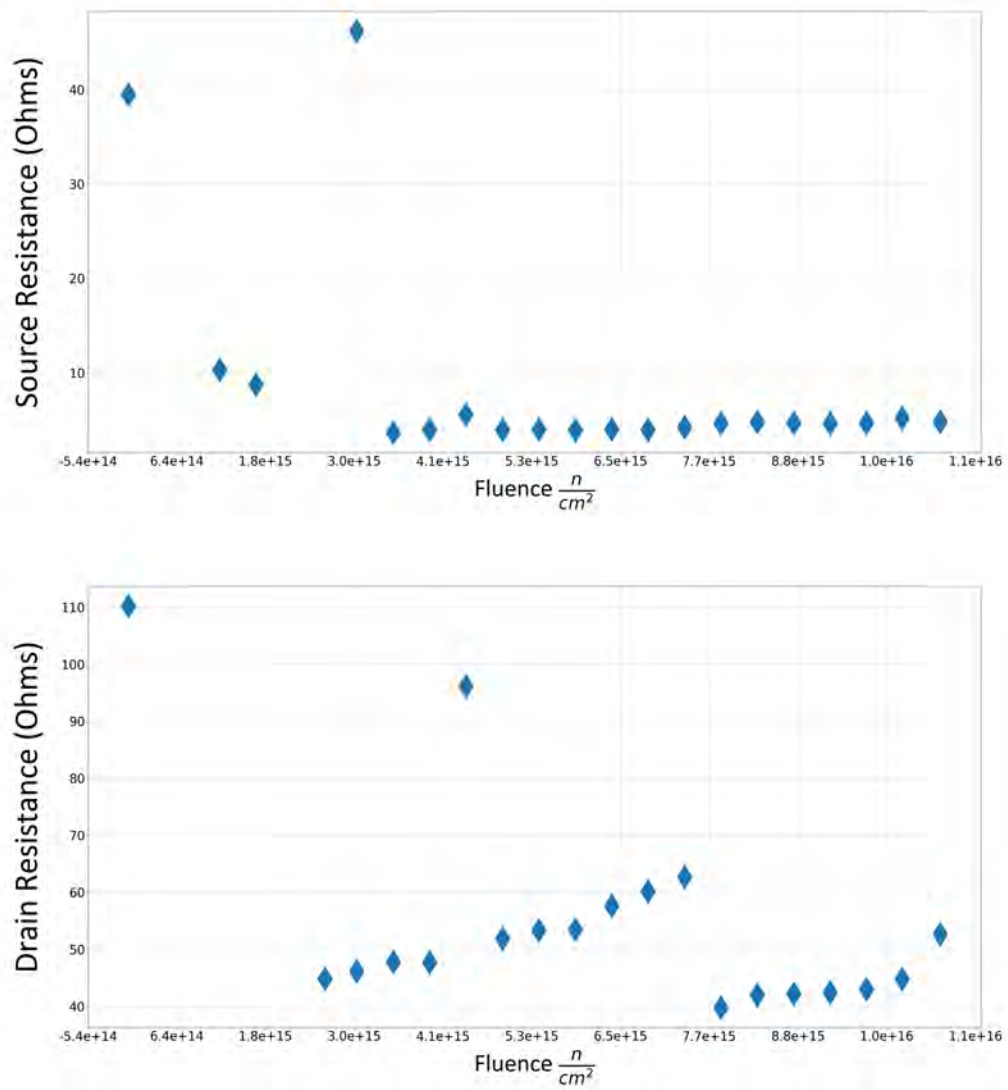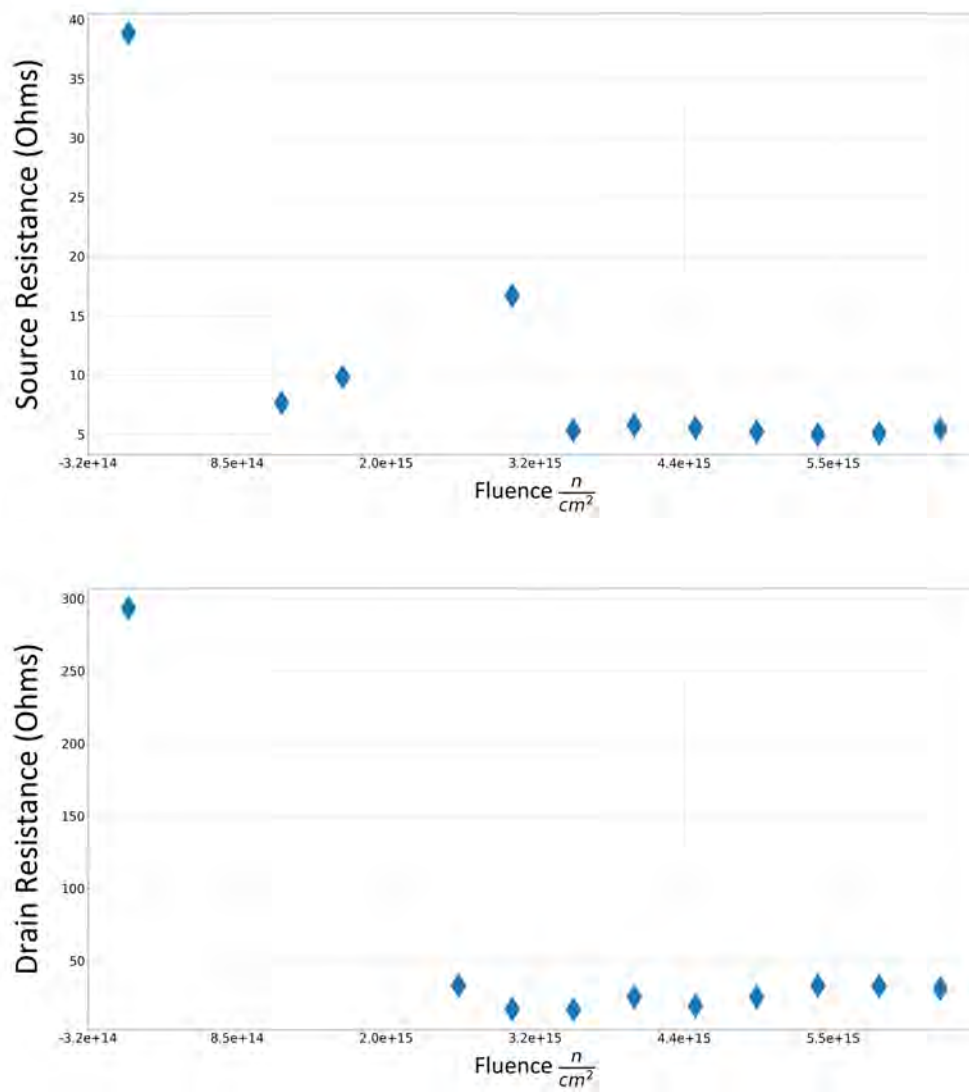
Figure A.27. Device 7 Source Access Resistance vs Fluence (top) and Drain Access Resistance vs Fluence (bottom)
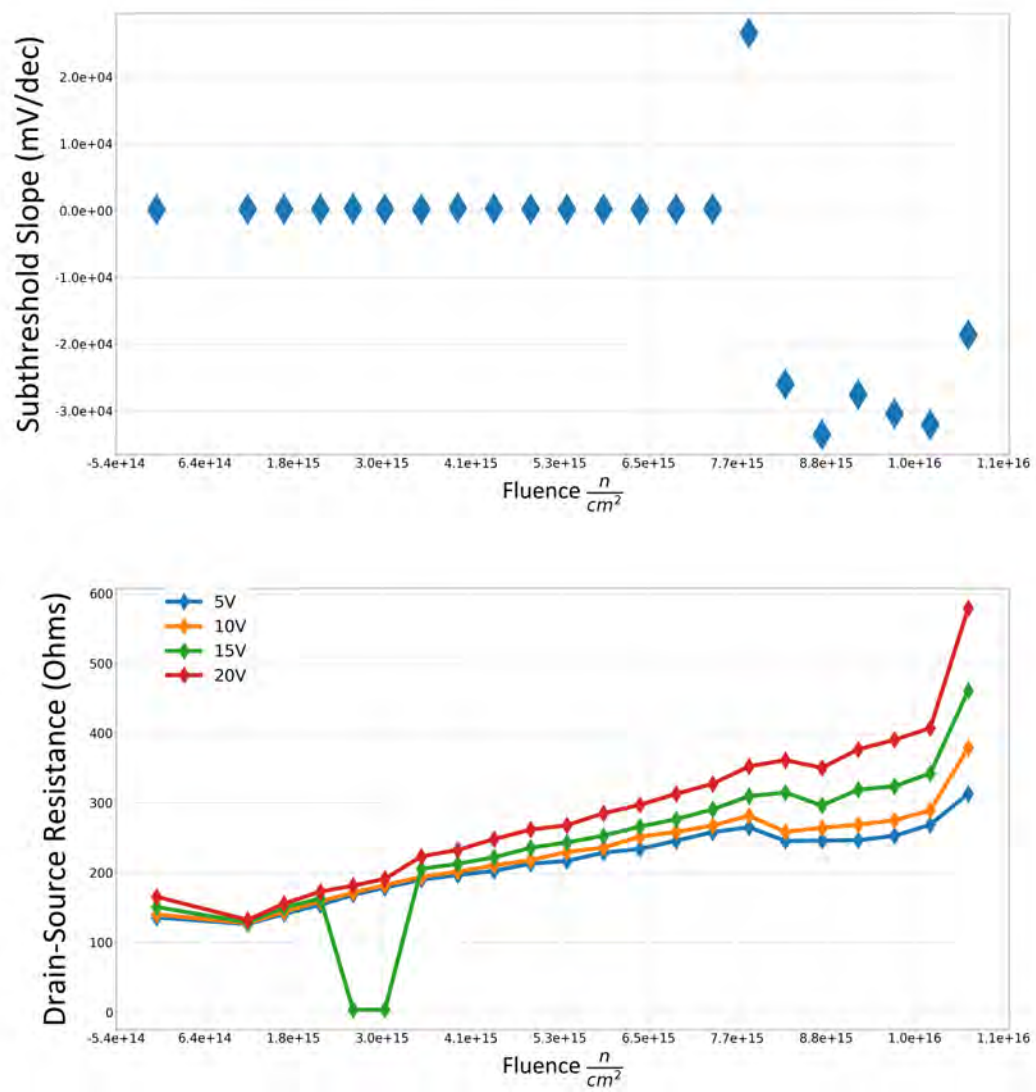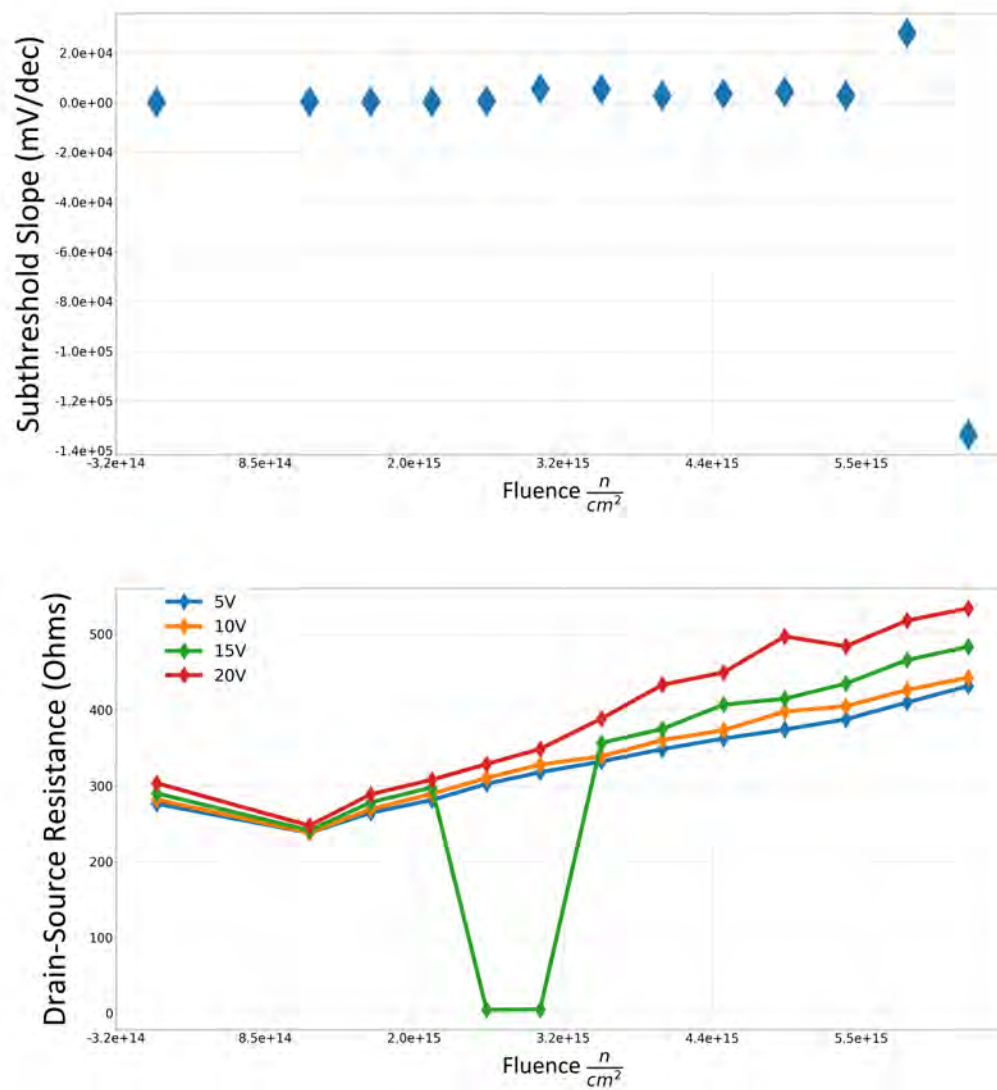
Figure A.28. Device 7 Subthreshold Slope vs Fluence (top) and Dynamic On-state Resistance vs Fluence (bottom)

APPENDIX B:
MCNP Input File

```
1 272 -19.3 (-1 -2 -3 -4 -5 -6 )
2 272 -19.3 (-7 -4 -2 -3 -1 -12 )
3 272 -19.3 (-1 -2 -3 -4 -17 -18 )
4 514 -1 (-1 -2 -3 -4 6 12 )
5 514 -1 (-3 -2 -1 -4 5 18 )
6 208 -2.699 (-31 -2 -33 -4 -35 17 )
7 208 -2.699 (-31 -2 -33 -4 7 -42 )
8 208 -2.699 (-7 -4 -17 -2 -33 3 )
9 208 -2.699 (-7 -4 -17 -2 1 -31 )
10 208 -2.699 (-35 -31 -42 -33 -59 2 )
11 208 -2.699 (-35 -31 -42 -33 4 -66 )
12 204 -0.001225 (31 42 59 -70 -71 -72 )
13 204 -0.001225 (42 33 59 -70 -71 -78 )
14 204 -0.001225 (33 59 35 -70 -78 -84 )
15 204 -0.001225 (31 66 35 -88 -72 -84 )
16 204 -0.001225 (33 66 35 -88 -84 -78 )
17 204 -0.001225 (42 33 66 -88 -78 -71 )
18 204 -0.001225 (31 42 66 -88 -71 -72 )
19 204 -0.001225 (-42 -33 -31 -35 -88 66 )
20 204 -0.001225 (-42 -33 -31 -35 -70 59 )
21 204 -0.001225 (-66 -59 -31 -33 -84 35 )
22 204 -0.001225 (-33 -31 35 66 -88 -84 )
23 204 -0.001225 (-31 -33 35 59 -70 -84 )
24 204 -0.001225 (-42 -35 33 66 -88 -78 )
25 204 -0.001225 (-66 -59 -35 -42 -78 33 )
26 204 -0.001225 (-59 -66 33 35 -84 -78 )
27 204 -0.001225 (-35 -42 33 59 -70 -78 )
28 204 -0.001225 (-31 -33 42 66 -88 -71 )
29 204 -0.001225 (-33 -31 42 59 -70 -71 )
```

```
30 204 -0.001225 (-66 -59 -33 -31 -71 42 )
31 204 -0.001225 (-66 -59 42 33 -78 -71 )
32 204 -0.001225 (-35 -42 31 66 -88 -72 )
33 204 -0.001225 (-66 -59 31 35 -84 -72 )
34 204 -0.001225 (-66 -59 -42 -35 -72 31 )
35 204 -0.001225 (-59 -66 31 42 -71 -72 )
36 204 -0.001225 (-42 -35 31 59 -70 -72 )
37 204 -0.001225 (-72 -84 -70 35 59 31 )
38 0 (1 :2 :3 :4 :5 :6 )(7 :4 :2 :3 :1 :12 )
(1 :2 :3 :4 :17 :18 )(1 :2 :3 :4 :-6 :-12 )(3 :2 :1 :4 :-5 :-18 )
(31 :2 :33 :4 :35 :-17 )(31 :2 :33 :4 :-7 :42 )(7 :4 :17 :2 :33 :-3
)(7 :4 :17 :2 :-1 :31 )(35 :31 :42 :33 :59 :-2 )
(35 :31 :42 :33 :-4 :66 )(-31 :-42 :-59 :70 :71 :72 )
(-42 :-33 :-59 :70 :71 :78 )(-33 :-59 :-35 :70 :78 :84 )
(-31 :-66 :-35 :88 :72 :84 )(-33 :-66 :-35 :88 :84 :78 )
(-42 :-33 :-66 :88 :78 :71 )(-31 :-42 :-66 :88 :71 :72 )
(42 :33 :31 :35 :88 :-66 )(42 :33 :31 :35 :70 :-59 )
(66 :59 :31 :33 :84 :-35 )(33 :31 :-35 :-66 :88 :84 )
(31 :33 :-35 :-59 :70 :84 )(42 :35 :-33 :-66 :88 :78 )
(66 :59 :35 :42 :78 :-33 )(59 :66 :-33 :-35 :84 :78 )
(35 :42 :-33 :-59 :70 :78 )(31 :33 :-42 :-66 :88 :71 )
(33 :31 :-42 :-59 :70 :71 )(66 :59 :33 :31 :71 :-42 )
(66 :59 :-42 :-33 :78 :71 )(35 :42 :-31 :-66 :88 :72 )
(66 :59 :-31 :-35 :84 :72 )(66 :59 :42 :35 :72 :-31 )
(59 :66 :-31 :-42 :71 :72 )(42 :35 :-31 :-59 :70 :72 )
(72 :84 :70 :-35 :-59 :-31 )


1 p -1 3.7854716527663e-031 4.2006196283366e-014 0.9
2 p 4.1897776066118e-014 3.4914813388431e-015 1 2.4
3 p 1 -3.7854716527663e-031 -4.2006196283366e-014 0.9
4 p -4.1897776066118e-014 -3.4914813388431e-015 -1 2.4
5 p -1.4593926746589e-028 1 -3.4914813388431e-015 2.6
```

```
6 p 1.4593926746589e-028 -1 3.4914813388431e-015 -1.7
7 p 2.2204460492518e-016 -1 3.4646377683869e-015 1.5
8 p -4.1801773162483e-014 -3.3960530068025e-015 -1 2.4
9 p 4.1801773162483e-014 3.3960530068025e-015 1 2.4
10 p 1 1.942890293094e-016 -4.180757428122e-014 0.9
11 p -1 -1.942890293094e-016 4.180757428122e-014 0.9
12 p -2.2204460492518e-016 1 -3.6091980580516e-015 1.5
13 p -1 3.7854716527663e-031 4.2006196283366e-014 0.9
14 p 4.1897776066118e-014 3.4914813388431e-015 1 2.4
15 p 1 -2.5236477685109e-031 -4.197005621095e-014 0.9
16 p -4.1897776066118e-014 -3.4914813388431e-015 -1 2.4
17 p -1.4593926746589e-028 1 -3.4914813388431e-015 3.5
18 p 1.4593926746589e-028 -1 3.4914813388431e-015 -2.8
19 p -1 3.7854716527663e-031 4.2006196283366e-014 0.9
20 p 4.1897776066118e-014 3.4914813388431e-015 1 2.4
21 p 1 -3.7854716527663e-031 -4.2006196283366e-014 0.9
22 p -4.1897776066118e-014 -3.4914813388431e-015 -1 2.4
23 p -1.4593926746589e-028 1 -3.4914813388431e-015 1.7
24 p 1.4593926746589e-028 -1 3.4914813388431e-015 -1.5
25 p 1 3.7854716527663e-031 -4.1900378151332e-014 0.9
26 p 4.2119820671043e-014 3.4914813388431e-015 1 2.4
27 p -1 -3.7854716527663e-031 4.1900378151332e-014 0.9
28 p -4.2119820671043e-014 -3.4914813388431e-015 -1 2.4
29 p 1.4593926746589e-028 -1 3.4914813388431e-015 -2.6
30 p -1.4593926746589e-028 1 -3.4914813388431e-015 2.8
31 p -1 -8.705605700798e-017 4.2021390432514e-014 1
32 p 4.1931040251474e-014 3.7192471324943e-015 1 2.3999999999999
33 p 1 8.705605700798e-017 -4.2039460468723e-014 1
34 p -4.1931040251474e-014 -3.7192471324943e-015 -1 2.4000000000001
35 p -8.7056057008136e-017 1 -3.7192471324943e-015 3.6
36 p 8.7056057008136e-017 -1 3.7192471324943e-015 -3.5
37 p -1 -8.705605700798e-017 4.2021390432514e-014 1
38 p 4.1931040251474e-014 3.7192471324943e-015 1 2.4
```

```
39 p 1 8.705605700798e-017 -4.2039460468723e-014 1
40 p -4.1931040251474e-014 -3.7192471324943e-015 -1 2.4
41 p -8.7056057008136e-017 1 -3.7192471324943e-015 -1.5
42 p 8.7056057008136e-017 -1 3.7192471324943e-015 1.6
43 p 2.1182116378979e-016 -1 3.6446581312433e-015 1.5
44 p -4.2021941482062e-014 -3.7551593071916e-015 -1 2.4
45 p -2.1182116378978e-016 1 -3.5723779864109e-015 3.5
46 p 4.2021941482062e-014 3.7551593071916e-015 1 2.4
47 p 1 2.0816681711722e-016 -4.2021941482062e-014 1
48 p -1 -2.0816681711722e-016 4.2021941482062e-014 -0.9
49 p 2.1182116378979e-016 -1 3.6446581312433e-015 1.5
50 p -4.2021941482062e-014 -3.7551593071916e-015 -1 2.4
51 p -2.1182116378978e-016 1 -3.5723779864109e-015 3.5
52 p 4.2021941482062e-014 3.7551593071916e-015 1 2.4
53 p 1 2.0816681711722e-016 -4.2021941482062e-014 -0.9
54 p -1 -2.0816681711722e-016 4.2021941482062e-014 1
55 p -3.1658304141348e-017 1 -3.663735981263e-015 3.6
56 p -1 -3.1658304141195e-017 4.1966322589747e-014 1
57 p 3.1658304141348e-017 -1 3.663735981263e-015 1.6
58 p 1 3.1658304141195e-017 -4.1966322589747e-014 1
59 p 4.1966322589747e-014 3.663735981263e-015 1 2.5
60 p -4.1966322589747e-014 -3.663735981263e-015 -1 -2.4
61 p -3.1658304141348e-017 1 -3.663735981263e-015 3.6000000000001
62 p -1 -3.1658304141195e-017 4.1966322589747e-014 1
63 p 3.1658304141348e-017 -1 3.663735981263e-015 1.5999999999999
64 p 1 3.1658304141195e-017 -4.1966322589747e-014 1
65 p 4.1966322589747e-014 3.663735981263e-015 1 -2.4
66 p -4.1966322589747e-014 -3.663735981263e-015 -1 2.5
67 p 1 3.1658304141195e-017 -4.1966322589747e-014 -0.99999999973262
68 p -3.1658304141348e-017 1 -3.663735981263e-015 -1.6000000599639
69 p -4.1966322589747e-014 -3.663735981263e-015 -1 -2.5000000005901
70 p 0 0 1 7.5000000000199
71 p 0 -1 0 7.4845925935162
```

```
72 p -1 -9.251858538543e-017 0 7.4999999999949
73 p -3.1658304141348e-017 1 -3.663735981263e-015 -1.6000000599639
74 p -1 -3.1658304141195e-017 4.1966322589747e-014 -1.00000000002673
75 p -4.1966322589747e-014 -3.663735981263e-015 -1 -2.5000000001115
76 p 0 0 1 7.5000000000199
77 p 0 -1 0 7.4845925935162
78 p 1 0 0 7.5000000000051
79 p -1 -3.1658304141195e-017 4.1966322589747e-014 -1.0000000005293
80 p -4.1966322589747e-014 -3.663735981263e-015 -1 -2.5000000000658
81 p 3.1658304141348e-017 -1 3.663735981263e-015 -3.5999999400361
82 p 0 0 1 7.5000000000199
83 p 1 0 0 7.5000000000051
84 p 0 1 0 7.5154074064838
85 p 1 3.1658304141195e-017 -4.1966322589747e-014 -0.9999999999951
86 p 0 0 1 -2.4999999999801
87 p 3.1658304141348e-017 -1 3.663735981263e-015 -3.5999999400359
88 p 0 0 -1 7.4999999999801
89 p -1 -9.251858538543e-017 0 7.4999999999949
90 p 0 1 0 7.5154074064838
91 p -1 -3.1658304141195e-017 4.1966322589747e-014 -1.0000000000051
92 p 0 0 1 -2.4999999999801
93 p 3.1658304141348e-017 -1 3.663735981263e-015 -3.5999999400249
94 p 0 0 -1 7.4999999999801
95 p 0 1 0 7.5154074064838
96 p 1 0 0 7.5000000000051
97 p -3.1658304141348e-017 1 -3.663735981263e-015 -1.6000000599639
98 p -1 -3.1658304141195e-017 4.1966322589747e-014 -0.99999999974303
99 p 0 0 1 -2.4999999999801
100 p 0 0 -1 7.4999999999801
101 p 1 0 0 7.5000000000051
102 p 0 -1 0 7.4845925935162
103 p 1 3.1658304141195e-017 -4.1966322589747e-014 -1.0000000002572
104 p -3.1658304141348e-017 1 -3.663735981263e-015 -1.6000000599639
```

105 p 0 0 1 -2.4999999999801
106 p 0 0 -1 7.4999999999801
107 p 0 -1 0 7.4845925935162
108 p -1 -9.251858538543e-017 0 7.4999999999949
109 p 3.1658304141348e-017 -1 3.663735981263e-015 1.6000000599639
110 p 1 3.1658304141195e-017 -4.1966322589747e-014 0.99999999974288
111 p -1 -3.1658304141195e-017 4.1966322589747e-014 1.0000000002572
112 p -3.1658304141348e-017 1 -3.663735981263e-015 3.5999999400361
113 p 0 0 -1 7.4999999999801
114 p 4.1966322589747e-014 3.663735981263e-015 1 -2.4999999999801
115 p 3.1658304141348e-017 -1 3.663735981263e-015 1.6000000599639
116 p 1 3.1658304141195e-017 -4.1966322589747e-014 1.0000000007917
117 p -1 -3.1658304141195e-017 4.1966322589747e-014 0.99999999973262
118 p -3.1658304141348e-017 1 -3.663735981263e-015 3.5999999400819
119 p 0 0 1 7.5000000000199
120 p -4.1966322589747e-014 -3.663735981263e-015 -1 -2.5000000000199
121 p 0 0 -1 2.4999999999801
122 p 4.1966322589747e-014 3.663735981263e-015 1 2.5000000000199
123 p -1 -3.1658304141195e-017 4.1966322589747e-014 0.9999999999951
124 p 1 3.1658304141195e-017 -4.1966322589747e-014 1.0000000000049
125 p 0 1 0 7.5154074064838
126 p 3.1658304141349e-017 -1 3.663735981263e-015 -3.5999999400361
127 p 1 3.1658304141195e-017 -4.1966322589747e-014 1.0000000000051
128 p -1 -3.1658304141195e-017 4.1966322589747e-014 0.9999999999951
129 p 3.1658304141348e-017 -1 3.663735981263e-015 -3.5999999400361
130 p 0 0 1 -2.4999999999801
131 p 0 0 -1 7.4999999999801
132 p 0 1 0 7.5154074064838
133 p -1 -3.1658304141195e-017 4.1966322589747e-014 0.99999999999491
134 p 1 3.1658304141195e-017 -4.1966322589747e-014 1.0000000005293
135 p 3.1658304141348e-017 -1 3.663735981263e-015 -3.5999999400819
136 p -4.1966322589747e-014 -3.663735981263e-015 -1 -2.5000000000199
137 p 0 0 1 7.5000000000199

```
138 p 0 1 0 7.5154074064838
139 p 3.1658304141348e-017 -1 3.663735981263e-015 1.6000000599639
140 p -3.1658304141348e-017 1 -3.663735981263e-015 3.5999999400249
141 p -1 -3.1658304141195e-017 4.1966322589747e-014 -0.99999999974288
142 p 0 0 1 -2.4999999999801
143 p 0 0 -1 7.4999999999801
144 p 1 0 0 7.5000000000051
145 p 0 0 -1 2.4999999999801
146 p 4.1966322589747e-014 3.663735981263e-015 1 2.5000000001116
147 p -3.1658304141348e-017 1 -3.663735981263e-015 3.5999999400249
148 p 3.1658304141348e-017 -1 3.663735981263e-015 1.6000000599639
149 p 1 0 0 7.5000000000051
150 p -1 -3.1658304141194e-017 4.1966322589747e-014 -1.0000000000051
151 p 4.1966322589747e-014 3.663735981263e-015 1 2.5000000000658
152 p 0 0 -1 2.4999999999801
153 p -1 -3.1658304141195e-017 4.1966322589747e-014 -1.0000000000049
154 p 3.1658304141348e-017 -1 3.663735981263e-015 -3.5999999400249
155 p 0 1 0 7.5154074064838
156 p 1 0 0 7.5000000000051
157 p -3.1658304141348e-017 1 -3.663735981263e-015 3.5999999400361
158 p 3.1658304141348e-017 -1 3.663735981263e-015 1.6000000599639
159 p -1 -3.1658304141195e-017 4.1966322589747e-014 -1.0000000007917
160 p -4.1966322589747e-014 -3.663735981263e-015 -1 -2.5000000001116
161 p 0 0 1 7.5000000000199
162 p 1 0 0 7.5000000000051
163 p -1 -3.1658304141195e-017 4.1966322589747e-014 1.0000000002572
164 p 1 3.1658304141195e-017 -4.1966322589747e-014 0.99999999974303
165 p -3.1658304141348e-017 1 -3.663735981263e-015 -1.6000000599639
166 p 0 0 1 -2.4999999999801
167 p 0 0 -1 7.4999999999801
168 p 0 -1 0 7.4845925935162
169 p 1 3.1658304141195e-017 -4.1966322589747e-014 1.0000000002673
170 p -1 -3.1658304141195e-017 4.1966322589747e-014 0.99999999973262
```

171 p -3.1658304141348e-017 1 -3.663735981263e-015 -1.6000000599639
172 p -4.1966322589747e-014 -3.663735981263e-015 -1 -2.5000000001115
173 p 0 0 1 7.5000000000199
174 p 0 -1 0 7.4845925935162
175 p 0 0 -1 2.4999999999801
176 p 4.1966322589747e-014 3.663735981263e-015 1 2.5000000001115
177 p 1 3.1658304141195e-017 -4.1966322589747e-014 1.0000000000053
178 p -1 -3.1658304141195e-017 4.1966322589747e-014 0.99999999999491
179 p 0 -1 0 7.4845925935162
180 p -3.1658304141349e-017 1 -3.663735981263e-015 -1.6000000599639
181 p 0 0 -1 2.4999999999801
182 p 4.1966322589747e-014 3.663735981263e-015 1 2.5000000001115
183 p -3.1658304141348e-017 1 -3.663735981263e-015 -1.6000000599639
184 p -1 -3.1658304141195e-017 4.1966322589747e-014 -1.0000000000053
185 p 1 0 0 7.5000000000051
186 p 0 -1 0 7.4845925935162
187 p -3.1658304141348e-017 1 -3.663735981263e-015 3.5999999400359
188 p 3.1658304141348e-017 -1 3.663735981263e-015 1.6000000599639
189 p 1 3.1658304141195e-017 -4.1966322589747e-014 -1.0000000002572
190 p 0 0 1 -2.4999999999801
191 p 0 0 -1 7.4999999999801
192 p -1 -9.251858538543e-017 0 7.4999999999949
193 p 0 0 -1 2.4999999999801
194 p 4.1966322589747e-014 3.663735981263e-015 1 2.5000000005443
195 p 1 3.1658304141195e-017 -4.1966322589747e-014 -0.9999999999951
196 p 3.1658304141348e-017 -1 3.663735981263e-015 -3.5999999400359
197 p 0 1 0 7.5154074064838
198 p -1 -9.251858538543e-017 0 7.4999999999949
199 p 0 0 -1 2.4999999999801
200 p 4.1966322589747e-014 3.663735981263e-015 1 2.5000000010689
201 p 3.1658304141348e-017 -1 3.663735981263e-015 1.6000000599639
202 p -3.1658304141348e-017 1 -3.663735981263e-015 3.5999999400359
203 p -1 -9.251858538543e-017 0 7.4999999999949 204 p 1 3.1658304141194e-017

```
        -4.1966322589747e-014 -0.99999999999491
205 p 4.1966322589747e-014 3.663735981263e-015 1 2.5000000005901
206 p 0 0 -1 2.4999999999801
207 p 1 3.1658304141195e-017 -4.1966322589747e-014 -0.99999999999491
208 p -3.1658304141348e-017 1 -3.663735981263e-015 -1.6000000599639
209 p 0 -1 0 7.4845925935162
210 p -1 -9.251858538543e-017 0 7.4999999999949
211 p 3.1658304141348e-017 -1 3.663735981263e-015 1.6000000599639
212 p -3.1658304141348e-017 1 -3.663735981263e-015 3.5999999400819
213 p 1 3.1658304141195e-017 -4.1966322589747e-014 -0.99999999973262
214 p -4.1966322589747e-014 -3.663735981263e-015 -1 -2.5000000010689
215 p 0 0 1 7.5000000000199
216 p -1 -9.251858538543e-017 0 7.4999999999949
217 p -1 -9.251858538543e-017 0 7.4999999999949
218 p 0 1 0 7.5154074064838
219 p 0 0 1 7.5000000000199
220 p 3.1658304141348e-017 -1 3.663735981263e-015 -3.5999999400819
221 p -4.1966322589747e-014 -3.663735981263e-015 -1 -2.5000000005443
222 p 1 3.1658304141195e-017 -4.1966322589747e-014 -0.99999999999491

mode n p e
m204 7014.70c -0.755636 air (US S. Atm at sea level)
8016.70c -0.231475 18036.70c -3.9e-005 18038.70c -8e-006
18040.70c -0.012842
m208 13027.70c -1 aluminum
m272 74182.70c -0.260586 Tungsten
74183.70c -0.142269 74184.70c -0.307531 74186.70c -0.289615
m514 1001.70c -0.111894 Liquid Water,
8016.70c -0.888106
imp:n 1 36r 0
imp:p 1 36r 0
imp:e 1 36r 0
PHYS:P 100 0 0 -1 0 J 0
```

```
MPHYS ON
sdef pos=0 5.6 0 axs=0 -1 0 ext=0 rad=d1 dir=1 vec=0 -1 0 erg=31 par=e
SI1 0 .5
SP1 -21 1
E0 1e-4 33ILOG 30
NPS 1e5
print
prdmp 2j 1
fir5:n -2.0 -1.0 0 0 -1.0 -1.0 0 0 0 0
fs5 -1.5 19i 3.5
c5 -2.5 19i 2.5
fir15:p -2.0 -1.0 0 0 -1.0 -1.0 0 0 0 0
fs15 -1.5 19i 3.5
c15 -2.5 19i 2.5
```

Figure C.1. Exploded-view of the Full Photoneutron Converter including the Cooling System

THIS PAGE INTENTIONALLY LEFT BLANK

List of References

[1] A. Holmes-Siedle and L. Adams, *Handbook of Radiation Effects*, 2nd ed. Oxford, UK: OUP, 2002.

[2] M. A. Iobst, "Gamma and neutron radiation effects on biased gallium nitride transistors," Master's thesis, Naval Postgraduate School, 2015.

[3] ITER, "Fusion," 2017, ITER - International Thermonuclear Experimental Reactor, https://www.iter.org.

[4] G. S. Was, *Fundamentals of Radiation Materials Science: Metals and Alloys*. New York: Springer, 2016.

[5] M. Victoria, N. Baluc, and P. Spatig, "Structural materials for fusion reactors," *Nuclear Fusion*, vol. 41, no. 8, p. 1047, 2001.

[6] O. Ambacher, B. Foutz, J. Smart, J. Shealy, N. Weimann, K. Chu, M. Murphy, A. Sierakowski, W. Schaff, and L. Eastman, "Two dimensional electron gases induced by spontaneous and piezoelectric polarization in undoped and doped AlGaN/GaN heterostructures," *Journal of Applied Physics*, vol. 87, no. 1, pp. 334–344, 2000.

[7] M. G. Wade, "Proton irradiation-induced metal voids in gallium nitride high electron mobility transistors," Master's thesis, Naval Postgraduate School, 2015.

[8] A. Rubio, J. L. Corkill, M. L. Cohen, E. L. Shirley, and S. G. Louie, "Quasiparticle band structure of AlN and GaN," *Physical Review B*, vol. 48, no. 16, 1993.

[9] J. Ibbetson, P. Fini, K. Ness, S. DenBaars, J. Speck, and U. Mishra, "Polarization effects, surface states, and the source of electrons in AlGaN/GaN heterostructure field effect transistors," *Applied Physics Letters*, vol. 77, no. 2, pp. 250–252, 2000.

[10] B. Gil, *III-Nitride Semiconductors and their Modern Devices*. Oxford, UK: OUP, 2013, vol. 18.

[11] S. H. Simon, *The Oxford Solid State Basics*. Oxford, UK: OUP, 2013.

[12] U. Mishra and J. Singh, *Semiconductor Device Physics and Design*. Berlin, Germany: Springer Science & Business Media, 2007.

[13] H. Morkocc, *Nitride Semiconductor Devices: Fundamentals and Applications*. Hoboken: John Wiley & Sons, 2013.

[14] A. S. Grove, *Physics and Technology of Semiconductor Devices*, J. Wiley, Ed. Hoboken: John Wiley & Sons Inc., 1967.

[15] M. Lorenz, H. Hochmuth, and C. Gruner, "Oxide thin film heterostructures on large area, with flexible doping, low dislocation density, and abrupt interfaces: Grown by pulsed laser deposition," *Laser Chemistry*, no. 140976, p. 27, 2010.

[16] A. R. Arehart, "Investigation of electrically active defects in GaN, AlGaN, and Al-GaN/GaN high electron mobility transistors," Ph.D. dissertation, The Ohio State University, 2009.

[17] M. Lundstrom, *Fundamentals of Carrier Transport*, 2nd ed. Cambridge, UK: CUP, 2000.

[18] J. Debdeep, "Theory of transport in semiconductors," 2002, unpublished - A brief recap of semiconductor transport physics.

[19] R. F. Pierret and G. W. Neudeck, *Advanced Semiconductor Fundamentals*. Boston: Addison-Wesley Reading, 1987, vol. 6.

[20] D. Jin and J. A. del Alamo, "Mechanisms responsible for dynamic on-resistance in GaN high-voltage HEMTs," in *Power Semiconductor Devices and ICs (ISPSD), 2012 24th International Symposium*. IEEE, 2012, pp. 333–336.

[21] M. Nastasi, J. Mayer, and J. K. Hirvonen, *Ion-Solid Interactions: Fundamentals and Applications*. Cambridge, UK: CUP, 1996.

[22] C. Smith, *A Textbook of Nuclear Physics*. London, UK: MacMillan Company, 1965.

[23] V. Zerkin, "Evaluated nuclear data file," International Atomic Energy Association, 2017, https://www-nds.iaea.org/exfor/endf.htm.

[24] A. Polyakov, N. Smirnov, A. Govorkov, A. Markov, S. Pearton, N. Kolin, D. Merkurisov, and V. Boiko, "Neutron irradiation effects on electrical properties and deep-level spectra in undoped n-AlGaN/GaN heterostructures," *Journal of Applied Physics*, vol. 98, no. 3, 2005.

[25] A. Polyakov, N. Smirnov, A. Govorkov, A. Markov, N. Kolin, D. Merkurisov, V. Boiko, K. Shcherbatchev, V. Bublik, M. Voronova *et al.*, "Fermi level pinning in heavily neutron-irradiated GaN," *Journal of Applied Physics*, vol. 100, no. 9, 2006.

[26] A. Polyakov, N. Smirnov, A. Govorkov, A. Markov, S. Pearton, N. Kolin, D. Merkurisov, V. Boiko, C.-R. Lee, and I.-H. Lee, "Fast neutron irradiation effects in n-GaN," *Journal of Vacuum Science & Technology B: Microelectronics and Nanometer Structures Processing, Measurement, and Phenomena*, vol. 25, no. 2, pp. 436–442, 2007.

[27] J. C. Petrosky, J. W. McClory, T. E. Gray, and T. A. Uhlman, "Trap assisted tunneling induced currents in neutron irradiated AlGaN/GaN HFETs," *IEEE Transactions on Nuclear Science*, vol. 56, no. 5, pp. 2905–2909, 2009.

[28] A. Polyakov, N. Smirnov, A. Govorkov, N. Kolin, D. Merkurisov, V. Boiko, A. Korulin, and S. Pearton, "Neutron transmutation doping effects in GaN," *Journal of Vacuum Science & Technology B, Nanotechnology and Microelectronics: Materials, Processing, Measurement, and Phenomena*, vol. 28, no. 3, pp. 608–612, 2010.

[29] W. Gu, Y. Hao, L. Yang, C. Duan, H. Duan, J. Zhang, and X. Ma, "The effect of neutron irradiation on the AlGaN/GaN high electron mobility transistors," *Physica Status Solidi (c)*, vol. 7, no. 7-8, pp. 1991–1996, 2010.

[30] A. Polyakov, N. Smirnov, A. Govorkov, E. Kozhukhova, S. J. Pearton, F. Ren, L. Liu, J. Johnson, W. Lim, N. Kolin, S. S. Veryovkin, and V. S. Ermakov, "Comparison of neutron irradiation effects in AlGaN/AlN/GaN, AlGaN/GaN, and InAlN/GaN heterojunctions," *Journal of Vacuum Science & Technology B, Nanotechnology and Microelectronics: Materials, Processing, Measurement, and Phenomena*, vol. 30, no. 6, 2012.

[31] F. Berthet, Y. Guhel, B. Boudart, H. Gualous, J. Trolet, M. Piccione, and C. Gaquiere, "Influence of thermal and fast neutron irradiation on dc electrical performances of

AlGaN/GaN transistors," *IEEE Transactions on Nuclear Science*, vol. 59, no. 5, pp. 2556–2561, 2012.

[32] C.-H. Lin, E. J. Katz, J. Qiu, Z. Zhang, U. K. Mishra, L. Cao, and L. J. Brillson, "Neutron irradiation effects on gallium nitride-based schottky diodes," *Applied Physics Letters*, vol. 103, no. 16, p. 162106, 2013.

[33] F. Berthet, S. Petitdidier, Y. Guhel, J. L. Trolet, P. Mary, C. Gaquière, and B. Boudart, "Influence of neutron irradiation on electron traps existing in GaN-based transistors," *IEEE Transactions on Nuclear Science*, vol. 63, no. 3, pp. 1918–1926, 2016.

[34] M. Guthrie, "Future directions in high-pressure neutron diffraction," *Journal of Physics: Condensed Matter*, vol. 27, no. 15, 2015.

[35] W. M. Stacey, *Nuclear Reactor Physics*. Hoboken: John Wiley & Sons, 2007.

[36] A. Marks, "Physics of uranium and nuclear physics," *World Nuclear Association*, September 2016.

[37] CERN, "How an accelerator works," 2017, https://home.cern/about/how-accelerator-works.

[38] Y. Gohar, J. Bailey, H. Belch, D. Naberezhnev, P. Strons, and I. Bolshinsky, "Accelerator driven subcritical assembly; concept development and analyses," in *The RERTR-2004 Intern Meeting Vienna*, 2004.

[39] H. Bethe and W. Heitler, "On the stopping of fast particles and on the creation of positive electrons," in *Proceedings of the Royal Society of London A: Mathematical, Physical and Engineering Sciences*, vol. 146, no. 856. The Royal Society, 1934, pp. 83–112.

[40] P. Chomaz, "Collective excitations in nuclei," *Ecole Joliot Curie*, 1997.

[41] M. Berger, J. Coursey, M. Zucker, and J. Chang, "Stopping-power and range tables for electrons, protons, and helium ions," National Institute of Standards and Technology, 2017, https://www.nist.gov/pml/stopping-power-range-tables-electrons-protons-and-helium-ions.

[42] J. Hubbell and S. Seltzer, "X-ray mass attenuation coefficients," National Institute of Standards and Technology, 2017, https://www.nist.gov/pml/x-ray-mass-attenuation-coefficients.

[43] W. P. Swanson, "Calculation of neutron yields released by electrons incident on selected materials." *Health Physics*, vol. 35, no. 2, pp. 353–367, 1978.

[44] S. Vaughn, "Investigation of a passive, temporal, neutron monitoring system that functions within the confines of start I," Master's thesis, Air Force Institute of Technology School of Engineering and Management, 2003.

[45] R. Augustine, "Analysis of proton radiation effects on gallium nitride high electron mobility transistors," Master's thesis, Naval Postgraduate School, 2017.

[46] C. Luan, Z. Lin, Y. Lv, J. Zhao, Y. Wang, H. Chen, and Z. Wang, "Theoretical model of the polarization coulomb field scattering in strained AlGaN/AlN/GaN heterostructure field-effect transistors," *Journal of Applied Physics*, vol. 116, no. 4, 2014.

[47] A. D. Koehler, P. Specht, T. J. Anderson, B. D. Weaver, J. D. Greenlee, M. J. Tadjer, M. Porter, M. Wade, O. C. Dubon, K. D. Hobart, T. R. Weatherford, and F. J. Kub, "Proton radiation-induced void formation in Ni/Au-Gated AlGaN/GaN HEMTs," *IEEE Electron Device Letters*, vol. 35, no. 12, pp. 1194–1196, 2014.

THIS PAGE INTENTIONALLY LEFT BLANK

Initial Distribution List

1. Defense Technical Information Center
   Ft. Belvoir, Virginia

2. Dudley Knox Library
   Naval Postgraduate School
   Monterey, California